Abstract

Title of Dissertation: Gas Kinematics and Dynamics:
Spiral Structure and Cloud Formation in Disk Galaxies

Rahul Shetty, Doctor of Philosophy, 2007

Dissertation directed by: Professor Eve C. Ostriker
Department of Astronomy

Star formation in disk galaxies occurs as a result of various physical mechanisms acting in the interstellar medium. Molecular clouds, the sites of star formation, grow from the diffuse interstellar medium due to a combination of gas self-gravity, galactic rotation, and magnetohydrodynamic effects. Observations have suggested that spiral arms promote star formation by compressing gas as it flows through the arms. When the density is sufficiently high, gravitational instability causes gas to collapse and form clouds. After the formation of stars within such clouds, the subsequent evolution of the cloud and the surrounding ISM is dramatically altered. Feedback effects such as stellar winds, ionizing radiation, and supernova explosions inject energy into the surrounding medium; these processes may halt the collapse, and perhaps even destroy the natal clouds. In this thesis, we study the flow of gas through the spiral arms of the grand-design galaxy M51; additionally, through numerical simulations, we model the growth of clouds in spiral arms and investigate the effect of feedback on cloud formation and disk dynamics.

We use both observational and numerical methodologies to study gas kinematics and dynamics in spiral galaxies. Using CO and Hα velocity fields we study spiral arm streaming in M51. With numerical simulations, we investigate gravitational instability in disk galaxies, which leads to the growth of clouds. In order to study the subsequent evolution of the gaseous disk, we include feedback effects that return dense cloud gas back into the surrounding ISM.

We find that the simple description of a stationary spiral pattern in M51 is inaccurate. Our numerical models suggest that sheared features can grow regardless of the presence of grand-design spiral structure, but that spiral perturbations cause arm clouds to grow, along with distinct spiral substructure. We find that feedback can significantly affect the evolution of the gaseous disk. We suggest that the disk thickness is important in setting the rate at which stars form. The turbulence scale also needs to be considered, both for the growth of clouds and stars, as well as for the evolution of any large-scale spiral pattern.

Gas Kinematics and Dynamics: Spiral Structure and Cloud Formation in Disk Galaxies

by

Rahul Shetty

Dissertation submitted to the Faculty of the Graduate School of the
University of Maryland at College Park in partial fulfillment
of the requirements for the degree of
Doctor of Philosophy
2007

Advisory Committee:

Professor Eve C. Ostriker, Chair/Adviser
Professor Stuart N. Vogel
Professor Massimo Ricotti
Professor Daniel P. Lathrop, Dean's Representative
Professor Colin A. Norman

Preface

This thesis contains research that has already been published. Chapter 2 entitled "Kinematics of Spiral Arm Streaming in M51" has been published in the Astrophysical Journal (Shetty, R., Vogel, S. N., Ostriker, E. C., & Teuben, P. J. 2007, ApJ, 665, 1138). Chapter 3 entitled "Global Modeling of Spur Formation in Spiral Galaxies" has also been published in the Astrophysical Journal (Shetty, R., & Ostriker, E. C. 2006, ApJ, 647, 997). The observations presented in Chapter 2 were obtained with the BIMA interferometer and the Maryland-Caltech Palomar Fabry-Perot. Simulations presented in Chapter 3 were performed on many workstations in the Astronomy Department at the University of Maryland (UMD). The high-resolution simulations presented in Chapter 4 were performed using Teragrid resources, the Beowulf cluster (*BORG*) in the Department of Astronomy at UMD, and the High Performance Computing Cluster at UMD, maintained and supported by the Office of Information Technology and the Department of Astronomy. This work was supported in part by the National Science Foundation under grants AST-0228974 and AST-0507315.

To my parents, Nirupa and Raghuram Shetty.

Acknowledgements

The last six years of my life has truly been an amazing experience, and for this I am grateful to a number of individuals, both for helping me reach this finish line, as well as making the journey enjoyable.

I owe my deepest gratitude to my advisers, Eve Ostriker and Stuart Vogel. Both were always willing to answer my many questions, allowed me to work and learn at my own pace, and were generous in sending me to conferences and summer schools. Stuart was my first adviser, and patiently waded through my initial attempts at scientific writing. His keen sense of how nebulous research can seem to newcomers ensured that I stayed focused, and his affinity for M51 was contagious. Eve assured that I made steady progress, and I was in awe of her breadth of knowledge, intuition, as well as her equanimity. I always felt more knowledgeable after our meetings, which sometimes lasted three hours or more. I feel tremendously fortunate and honored to have had Eve and Stuart as my mentors, and I look forward to continued collaboration with them in the future. Thank you Stuart and Eve.

I am very grateful to my parents, my brother Rohith, and Mary. My parents were supportive throughout my academic career, and I would not have been able to complete this thesis without them. I enjoyed many weekend brunches with my brother and Mary, and of course, the sometimes heated debates.

I am also grateful to Peter Teuben, who taught me much about computing, especially how to be efficient; from him I also learned invaluable keyboard shortcuts on both the command line and in Emacs, as well as how delicious Ollie-bollen is. I would also like to thank Marc Pound and Stephen White for helping me with various computing issues, including data reduction using MIRIAD. I will remember advice, ranging from coursework to the process of job hunting, from Cole Miller and Andy Harris. Additionally, I'm thankful to Mary Ann and John Trasco for taking care of all the administrative necessities. I'm grateful to Eric Wilcots, who prepared me well as my first research adviser at the University of Wisconsin. I would also like to thank my committee for critiquing this thesis, and for directing me to think about the subject in a different way.

I will definitely miss the camaraderie amongst graduate students, faculty and post-docs. Woong-Tae Kim was like an academic big brother to me, and I have enjoyed remaining in touch with him. I certainly benefited from discussions with my office mates: Rachel Kuzio de Naray, Nikolaus Volgenau, Nicholas Chapman, Raquel Fraga-Encinas, Lisa Wei, Misty LaVigne, Rick Pernak, and Kayhan Gultekin, who all made it easier learning new software, especially Nikolaus, who first showed me how to reduce BIMA data. I also thank Gilberto Gomez for helping me learn how to use ZEUS. Many of us enjoyed the hospitality of Glen Petitpas during the NCAA tournament. I will always remember the many late-night conversations with David Garofalo and

Ji Hoon Kim; I will further miss having David on my soccer team. I also benefited from many discussions relating to numerical hydrodynamics with John Vernaleo, Hao Gong, and Kwang-Ho Park. I also thank Mark Wolfire and John Ohlmacher, who ensured that my computer functioned properly. I will of course miss attending Terp basketball games and playing IM sports on the Dirty Snowballs, along with the associated company. I am especially appreciative of all the time spent with Vanessa Lauburg, Matthew Knight, Stacy Teng, Nicholas Chapman, Rob Piontek, Franziska Koeckert, Derek and Frances Richardson, the Mandalay family, and, of course, Rocky and Petee. Finally, I thank Vanessa for making graduate school seem much shorter than it really was.

Contents

List of Tables

List of Figures

Chapter 1

Introduction

Star formation, the process of converting the diffuse gas in the interstellar medium (ISM) into dense stars, involves many physical mechanisms that depend on the basic dynamical state of the host galaxy. Since stars form in molecular clouds, clouds first need to form within a galaxy's gaseous component. In disk galaxies, clouds grow as a result of unstable perturbations in the gas as it flows around the galactic center. Instabilities can arise due to the interaction between stars and gas, rotational shear, magnetic fields, and the thermal state of the various phases in the ISM, among other factors. One potential source of large scale perturbations is the spiral arms. Gas becomes compressed as it flows through the spiral arm, and clouds will grow if the collapse due to gas self-gravity is able to overwhelm all restoring effects acting to disperse the dense gas. Gas self-gravity is also important in the formation of clumps and cores, which are direct precursors to stars, within these larger clouds. Once stars are formed, stellar winds, ionizing radiation from the young O and B stars, and supernovae affect the subsequent evolution of the natal cloud, and perhaps also the dynamics of the galaxy's global flow. Thus, the process of individual star formation and evolution, which occurs on small scales, is intimately related to the large scale dynamical state of the gaseous disk. In this introductory chapter, we discuss the relevant physical mechanisms at work in a gaseous disk; we also present an overview of the

observations and current theoretical understanding of the gaseous component, focusing on spiral structure and the formation and destruction of gas clouds.

1.1 Spiral Structure in Disk Galaxies

Spiral arms, which in most disks are the dominant morphological features (see Figure 1.1), appear with many different shapes and sizes. In the widely utilized Hubble classification of galaxies (Hubble 1936), early-type disks have tight winding arms, and late-type disks have open arms (Kennicutt 1981). The pitch angle, defined as the angle between a spiral arm segment and a galactocentric circle at the radius of the spiral segment, increases from early-type to late-type disks. Grand-design spirals are disks that have distinct arms spanning the whole disk. Many disks, especially isolated ones without bars, are flocculent spirals, showing localized, patchy, and segmented spiral features (Elmegreen & Elmegreen 1982).

There are other differences between galaxies of different Hubble types. From early- to late-type galaxies, gas fraction increases, relative bulge size decreases, and total mass decreases (e.g. Bertin & Lin 1996, and references therein). These properties are generally thought not to vary much over the course of a few galactic orbits. In fact, it was these characteristics that were initially used to classify galaxies, since the telescopes of the early 20th century were not powerful enough to resolve spiral structure in most galaxies and gas was not observed. Galaxies that have been classified through these properties, and which show fragmented spiral arm segments and varying pitch angles, do generally follow the trend of increasing pitch angle from early to late type disks. Thus, there seems to be a correlation between the pitch angle of the spiral arms with the other characteristics of the galaxy that seemingly have little relationship to the spiral arms. For example, it is not immediately obvious why the shape of the spiral arm is related to the total mass of the

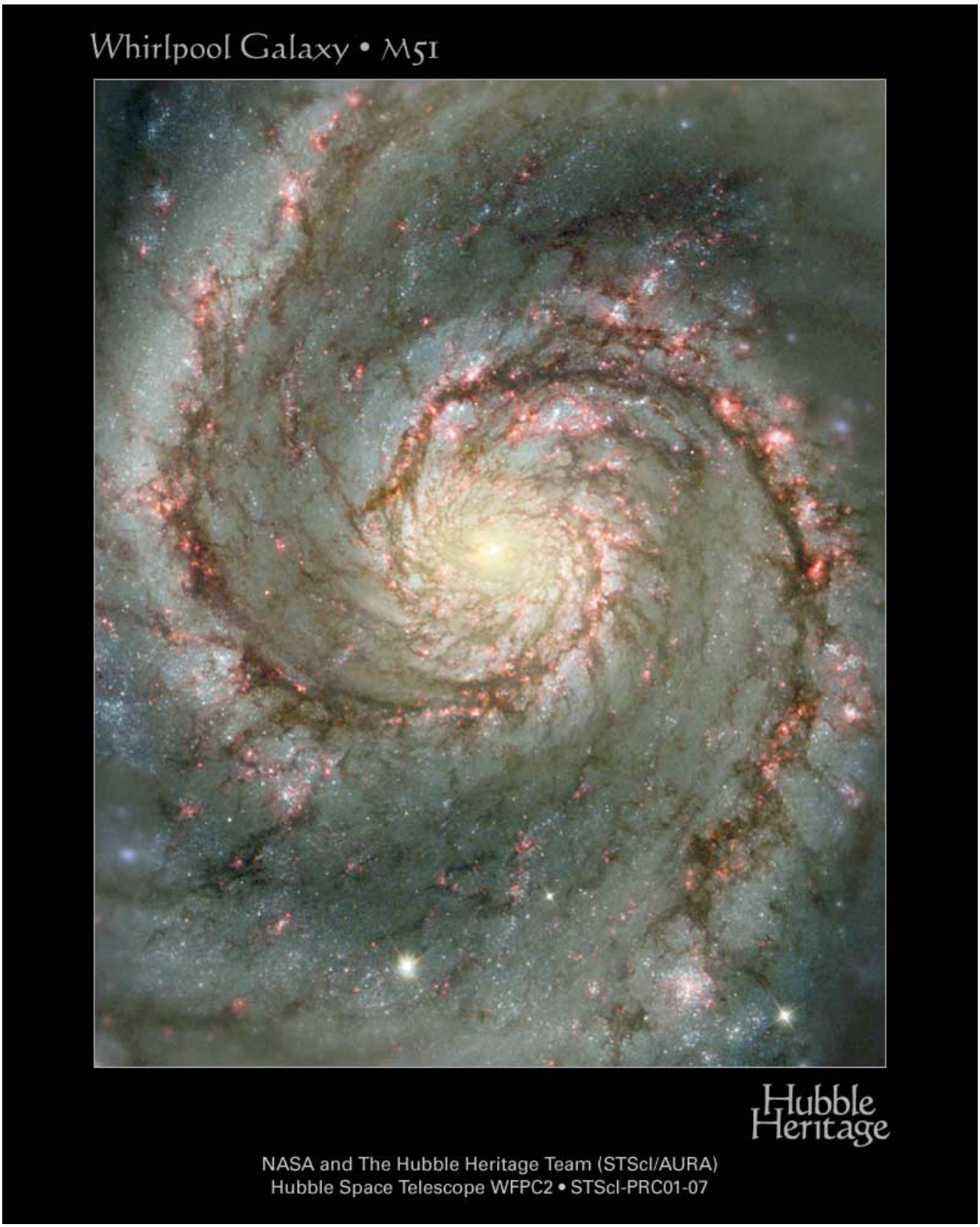

Figure 1.1: *Hubble Space Telescope* image of M51 (Scoville & Rector 2001).

galaxy, or to the size of the bulge.

This correlation between the spiral arm pitch angle and other basic characteristics that are thought to be slowly evolving led to the formulation of the quasi-stationary spiral structure, or QSSS, hypothesis; the QSSS hypothesis was attractive because it also avoids the "winding dilemma" (Lindblad 1963). The "winding dilemma" arises if the spiral arms are material objects; the radial velocity profile in galaxy disks, with angular velocity Ω decreasing outward (typically $\Omega \propto 1/R$) implies that any material entity would be wrapped around the center, and eventually sheared out. The Lin-Shu density wave theory, developed within the framework of the QSSS hypothesis, describes the spiral arms as the result of a global wave which rotates with a fixed angular velocity (Lin & Shu 1964). If spiral arms represent a density wave with fixed angular pattern speed, stars and gas pass in and out of the arms, but the global spiral morphology remains relatively unchanged for a significant amount of time.

Many observations of grand design spiral galaxies have been explained as natural consequences predicted by density wave theory, and the more developed modal theory (Bertin et al. 1989a,b). The observed streaming velocities across the spiral arms in M51 (Aalto et al. 1999; Rand 1993) and M81 (Visser 1980a) have qualitatively agreed with predictions from density wave theory. Further, the relative locations of the molecular arms (widely observed in CO maps), HII regions, and photodissociated HI gas, is explained through density wave theory. In the density wave depiction, gas is compressed as it passes through the spiral potential minimum. Stars eventually form downstream, within collapsed gas clouds. There, radiation from hot O and B stars ionize the surrounding gas, creating HII regions. Then, the stellar radiation field will eventually photodissociate the molecular medium into atomic gas. Such sequences have been observed in M51 (Vogel et al. 1988), M81 (Allen et al. 1997), and M100 (Knapen & Beckman 1996).

However, the opposing theory asserting that spiral arms are transient has also been

cited to explain observations. Toomre & Toomre (1972) suggested that tidal encounters between two galaxies can also produce spiral structure in disks. Multiple density wave patterns, with different pattern speeds, and regenerative spiral arms are possible consequences of tidal interactions. Even studies of the grand design galaxy M51, which has been heavily cited in support of density wave theory, have suggested that the arms are transient (e.g. Elmegreen et al. 1989; Toomre & Toomre 1972; Vogel et al. 1993).

Regardless of the distinctions between the QSSS and tidally-driven explanations for global kpc-scale spiral structure, one aspect of disk galaxies that is unambiguous is that observed sub-kpc scale structures are transient; many of these features can be attributed to the process of star formation. Besides the increased concentration of gas along the arms, observations also show regularly spaced dust lanes projecting out from the main spiral arms, reaching well into interarm regions. In some cases, these features even connect one arm to another. These extinction features were labeled “feathers” by Lynds (1970). Later, stellar features were observed to be correlated with the feathers, and were denoted “spurs” (Elmegreen 1980). Spurs and feathers can easily be identified in Figure 1.1. The survey by La Vigne et al. (2006) found that the majority of grand design spirals clearly show the presence of spurs or feathers. That survey also found a strong correlation between the spurs/feathers and bright OB associations located in the spiral arms, further attesting to the link between the spiral arms the formation of stars.

1.2 Star Formation in Disk Galaxies

Despite the remaining uncertainty in the underlying nature of the spiral arms, it is clear that the process of star formation is affected by any degree of spiral structure. In grand design spirals, a large fraction of young stars are observed to be associated with the spiral arms (e.g Scoville et al. 2001). Though observations have shown that disks with strong

or weak spiral structure have comparable star formation rates (per unit molecular mass), spiral structure certainly has the effect of concentrating star formation activity in or near the arms (e.g. Kennicutt 1998a, and references therein). A simple explanation for this association is that the gas density is higher in the spiral arms, making it more likely for gas clouds to form, within which stars can be born.

The idea that stars form in regions of high gas density suggests that large scale gravitational instabilities regulate star formation (Quirk 1972). Observations do indeed show an increase in star formation activity in environments with higher densities. Empirically, the star formation rate per unit area Σ_{SFR} is connected to the gas surface density Σ through the Kennicutt-Schmidt power law relation $\Sigma_{SFR} \propto \Sigma^{\alpha}$, as long as Σ is above some critical value (Kennicutt 1989; Schmidt 1959). This relation is observed on both global and local scales (e.g. Kennicutt et al. 2007); for entire disks, α=1.4 gives a remarkably good fit for over 4 orders of magnitude in surface density (Kennicutt 1998b), though there is large dispersion in both local and global relationships.

One proposal is that the star formation rate is correlated with the orbital time of the disk τ_{dyn}, or the angular velocity Ω (Wyse 1986; Wyse & Silk 1989). For normal disks, $\Sigma_{SFR} \propto \Sigma/\tau_{dyn} \propto \Sigma\Omega$ fits as well as the $\Sigma_{SFR} \propto \Sigma^{\alpha}$ power law. If all disks are considered, including starburst galaxies, the slope of this correlation only decreases by $\sim$10%. Both the Kennicutt-Schmidt power law and linear relationship between Σ_{SFR} and Ω have been extensively documented, but a clear theoretical framework remains elusive (Kennicutt 1998b).

Since the azimuthally averaged surface density decreases with radius in galaxy disks, a real critical surface density in the Kennicutt-Schmidt law would also imply a threshold radius. Most disk galaxies do indeed show such a cutoff radius; outside this radius, very little star formation occurs. The actual values of the cutoff radii and critical densities, however, vary between individual galaxies (Martin & Kennicutt 2001).

It has been proposed that the large-scale dynamics of the disk determines the cutoff radius. In a (2D) gaseous medium where only thermal pressure and gas self-gravity operate, the minimum wavelength necessary for perturbations to grow is the Jeans length $\lambda_J = c_s^2/G\Sigma$, where c_s is the sound speed and G is the gravitational constant. For a representative ISM surface density $\Sigma \sim 1-40$ $M_\odot$ pc^{-2} and $c_s \sim 7$ km s^{-1}(e.g. Heiles & Troland 2003), $\lambda_J \sim 0.3-11$ kpc. For a rotating disk, the Toomre Q parameter describes the gravitational stability of axisymmetric perturbations, accounting for the restoring effects of thermal pressure and rotational shear (Toomre 1964). For thin gaseous disks,

$$Q \equiv \frac{\kappa c_s}{\pi G \Sigma}. \tag{1.1}$$

Here, κ is the epicyclic frequency, which is related to the angular velocity Ω by $\kappa^2 = 4\Omega^2 + 2\Omega R(d\Omega/dR)$. For $Q > 1$ the disk is stable, so linear perturbations will not grow; in regions where $Q < 1$, the disk is unstable, so linear disturbances can lead to cloud growth. Observation have found that the threshold Q-value $Q_{crit} \approx 1.5$ in many galaxies (Martin & Kennicutt 2001).

The Toomre Q parameter indicates the susceptibility for linear, axisymmetric perturbations to grow. Using azimuthally averaged quantities, such as Σ and κ, the threshold Q value would locate a cutoff radius, inside of which active star formation occurs. However, in real galaxies there are many non-linear, non-axisymmetric sources of perturbations. As a result, star formation may still proceed in localized regions outside of the Q derived cutoff radius. For instance, a spiral potential can cause gas outside of the critical radius to collapse, sufficiently increasing the density to ultimately form stars (e.g. Ferguson et al. 1998). Thus, other mechanisms besides the interplay between thermal pressure, rotation, and gas self-gravity also need to be considered to develop a more complete picture of the star formation process. For example, another explanation for the observed cutoff in star formation is that a phase transition occurs at the critical radius, inside of which the higher pressure allows the gravitationally unstable cold component to exist (Schaye 2004). Es-

sentially, any mechanism that creates or sustains compressions in the gaseous medium can be the initial driver of star formation.

One important aspect of the ISM is the magnetic field. In fact, magnetic fields were thought to be responsible for tempering the collapse of gas clouds. Typically, molecular clouds have densities n_H = 100 cm^{-3}. If the collapse times of clouds were determined solely by self-gravity, then the typical cloud would collapse in 4 Myr. The total mass of molecular material in the Milky Way is estimated to be $\sim 10^9 M_\odot$ (Cohen et al. 1986; Williams & McKee 1997). If the collapses occurs at the free-fall rate, then the star formation rate would be 250 M$_\odot$ yr^{-1}. However, this value is almost 2 orders of magnitude greater than the observed star formation rate of 4 M$_\odot$ yr^{-1} (McKee & Williams 1997). Hence, a resistive mechanism is required to slow or reverse the collapse. Magnetic fields could keep the ions from collapsing at the free-fall speed, but allow neutrals to drift through the field lines at a slower rate; this process is known as ambipolar diffusion. Localized collapse would then occur only at the rate permitted by ambipolar diffusion (e.g. Spitzer 1978). However, existing field strengths in clouds appear to be too low for magnetic regulation to apply, and observational and theoretical advances have led to a different understanding of the star formation process, leading to the development of turbulence regulated star formation theory (see reviews by Mac Low & Klessen 2004; McKee & Ostriker 2007, and references therein).

On larger scales in disk galaxies, magnetic fields can be important for the development of instabilities, especially when other mechanisms are also at work. In general, Coriolis forces tend to divert compressive motions into epicycles. But, in disks with weak shear profiles and strong magnetic fields, magnetic fields can transfer spin angular momentum between neighboring condensations leading to the growth of dense clouds. This magneto-Jeans instability, or MJI, may be at work in the inner regions of galaxies where the rotation curve is rising, or equivalently, where there is little shear. Numerical simulations have also

showed that the MJI acts to grow spiral arm clouds and the associated spurs (Kim 2002; Kim & Ostriker 2001, 2002).

The thermal state of gas in the ISM is crucial for both star formation and the overall dynamics of a galaxy disk. McKee & Ostriker (1977), hereafter MO, expanded the two phase proposal of Field et al. (1969) to include a hot component. In the MO model, the majority of the volume of the ISM exists as a hot ionized medium (HIM), with temperatures and densities of $\sim 10^6$ K and $\sim 10^{-3}$ cm^{-3}, respectively. This medium is heated by supernova explosions (SNE), which also energize the remaining components of dense clouds of the cold neutral medium (CNM). The temperature and density of these clouds are 10-100 K and $\sim$50 cm^{-3}, and are surrounded by a warm neutral medium (WNM) and warm ionized medium (WIN). The density of the warm medium is 0.1 - 1 cm^{-3}.

Empirically, Heiles & Troland (2003) found that about half of the WNM exists as thermally stable gas, with temperatures $\sim$8000 K, and that the other half is thermally unstable, with temperatures $\sim$500-5000 K. The three phases exist in rough pressure equilibrium. In their original depiction, MO suggested that most of the volume of the ISM is occupied by the HIM. However, most of the ISM volume is now thought to be in the warm phase, with the hot phase existing mostly away from the midplane of galaxy disks; the mass fractions of the warm component is comparable to that of the cold medium (e.g Cox 2005).

The formation of stars requires the accumulation of gas in the ISM to form molecular clouds. The rate at which diffuse gas is gathered into dense molecular clouds, which is determined by the large-scale dynamics, may be important in setting the star formation rate. The warm and cold gas is gathered through a variety of possible instabilities; or, cold cloudlets could collide and stick with other cold clouds to form larger clouds. Once these clouds are large enough, self shielding from diffuse UV radiation allows the gas to exist in molecular form; the formation of H_2 molecules from HI atoms occurs mostly on the

surfaces of dust grains. Molecular clouds have masses of $\gtrsim 10^4$ M$_\odot$. Clouds with masses $\sim 10^5 - 10^6 M_\odot$ are called Giant Molecular Clouds (GMCs). In grand design galaxies, the molecular clouds in spiral arms are observed to be collected into larger masses $\gtrsim 10^7 M_\odot$, referred to as giant molecular associations (GMAs) (Vogel et al. 1988). Spiral arms have also been observed to contain $\sim 10^7 M_\odot$ atomic clouds, termed "superclouds" by Elmegreen & Elmegreen (1983), within which molecular clouds exist. Turbulence and other dynamical processes within these molecular clouds lead to the formation of clumps and cores, finally producing individual stars. The physics of clump and core formation within clouds are reviewed by Ballesteros-Paredes et al. (2007); Elmegreen & Scalo (2004); Mac Low & Klessen (2004); McKee & Ostriker (2007).

The SNE occurring after stars have consumed all their fuel are an integral part of the dynamics of the ISM, as MO depicted in their model. In addition to contributing to the phase structure of the ISM, supernovae return much of the gas from massive stars back into the ambient ISM. Further, SNE are at least partly responsible for driving ISM turbulence. On large scales correlated supernovae create superbubbles, which destroy the large natal clouds, and drive hot gas away from the midplane of the galaxy through chimneys. This gas cools well above the disk, and the clouds rain back onto the disk (Norman & Ikeuchi 1989). The return of halo gas to the disk may be another source of large scale turbulence.

Turbulence in the ISM is an extremely active research area, partly because turbulence may play a key role in the process of star formation. Observed velocity dispersions suggest that the turbulent velocities are $\sim$7 km s^{-1}(Heiles & Troland 2003; Mohan et al. 2004). As discussed, SNE are a potential source for turbulence, both due to single SN shocks as well as a number of correlated SN, which may also drive gas away from the midplane of the galaxy disk only to fall back onto the disk, again creating turbulence. However, SN driven turbulence only explains turbulence near active star forming regions.

Proposed non-stellar sources of turbulence in the ISM include cosmic rays, the magneto-rotational instability (Balbus & Hawley 1991; Piontek 2005), large-scale gravitational instability (Wada et al. 2002), and spiral shocks (Kim et al. 2006), many of which involve galactic rotation, underscoring the importance of the large scale dynamics on the smaller scale characteristics of the ISM.

1.3 Thesis Outline

The focus of this thesis is on the kinematics and dynamics of the global flow in galaxy disks, leading to the formation of gas clouds, with emphasis on the role of the spiral structure, gas self-gravity, and supernovae driven feedback. We employ both observational and theoretical methodologies to study these processes. We use interferometric CO observations to investigate the flow of the gaseous component through the spiral arms of M51. These observations test theoretical models of the way in which gas is compressed into spiral arms, initiating the process of star formation. Through the use of numerical simulations, we investigate the detailed response of the gaseous component to an external spiral potential, leading to the growth of large gas clouds in the spiral arms, as well as spiral arm substructure, known as spurs or feathers. We also include feedback effects, due to mechanical input from supernovae, to study the subsequent evolution of the gaseous disk. These theoretical models are compared to observations of the morphological structure of the ISM in the MW and external galaxies (including properties such as spur spacing and GMC masses), to observations of correlations between ISM properties and star formation rates, and to theoretical predictions based on simplified systems.

In Chapter 2, we present results of our analysis of spiral arm streaming in the grand design spiral galaxy M51. We fit the observed CO and Hα velocities to estimate the radial and tangential velocity components as a function of arm phase, or, equivalently,

arm distance. We then analyze these velocity components, and compare with predictions from theory. We also consider conservation of vortensity and mass, in order to assess whether the velocity profiles are consistent with the QSSS hypothesis.

In Chapter 3, we present results of our study of the growth of spiral arm clouds and spurs. We use numerical simulations to evolve the global flow of gas in a disk. We impose an external spiral potential, which represents the perturbations in the background stellar disk, in order to grow gaseous spiral arms. Gas self-gravity causes regions of enhanced density to collapse into clouds. Self-gravity also perturbs the flow through the spiral arms, resulting in the formation of spiral arm spurs. We compare models with and without self-gravity, as well as magnetic fields.

In Chapter 4, we extend the models presented in Chapter 3 to include feedback effects. Without feedback, self-gravitating clouds would collapse indefinitely. However, feedback associated with star formation returns much of the cloud gas back into the ISM. We consider feedback from correlated supernovae to disperse the clouds. We vary the feedback parameters, and study the subsequent evolution of the disk. We investigate the star formation rates associated with feedback, and compare with the observed Kennicutt-Schmidt relation. We also assess the role of feedback on large scale turbulence, as well as on the evolution of the spiral arms.

In Chapter 5 we summarize this thesis, and discuss prospects for future research.

Chapter 2

Kinematics of Spiral Arm Streaming in M51

Abstract

We use CO and Hα velocity fields to study the gas kinematics in the spiral arms and interarms of M51 (NGC 5194), and fit the 2D velocity field to estimate the radial and tangential velocity components as a function of spiral phase (arm distance). We find large radial and tangential streaming velocities, which are qualitatively consistent with the predictions of density wave theory and support the existence of shocks. The streaming motions are complex, varying significantly across the galaxy as well as along and between arms. Aberrations in the velocity field indicate that the disk is not coplanar, perhaps as far in as 20″ (800 pc) from the center. Velocity profile fits from CO and Hα are typically similar, suggesting that most of the Hα emission originates from regions of recent star formation. We also explore vortensity and mass conservation conditions. Vortensity conservation, which does not require a steady state, is empirically verified. The velocity and density profiles show large and varying mass fluxes, which are inconsistent with a steady flow for a single dominant global spiral mode. We thus conclude that the

spiral arms cannot be in a quasi-steady state in any rotating frame, and/or that out-of-plane motions may be significant.

2.1 Introduction

Spiral arms are the dominant morphological features of most disk galaxies. From a theoretical perspective, two frameworks have been proposed to describe the nature of the spiral arms: one is that the spiral arms are generally long-lasting, or slowly evolving, and the other is that the arms are transient features (e.g. Toomre & Toomre 1972). Observational studies have yet to show definitively whether the arms are evolving or long lived, although it has been over 40 years since the landmark paper by Lin & Shu (1964) suggesting that spiral structure in galaxies is a long lived phenomenon — the quasi-stationary spiral structure (QSSS) hypothesis (Lindblad 1963). In the QSSS depiction, although material passes in and out of the arms, the slowly evolving global pattern rotates with a single angular speed that results from the excitation of global modes. The spiral arms are formed from self-excited and self-regulated standing density waves (Bertin & Lin 1996; Bertin et al. 1989a,b).

However, interaction between a disk galaxy and a companion is another explanation for the presence of spiral arms. In such a framework, the arms are transient features that are generated by the tidal interaction (e.g., Toomre & Toomre 1972). Any spiral arms existing before the encounter are overwhelmed by the tidal driving (Salo & Laurikainen 2000).

Regardless of the origin of the stellar arms, gas in the disk will respond strongly to the gravitational perturbations those arms impose. Numerical studies have indicated that shocks can develop if the relative speed between the spiral perturbation and the gas is large (Roberts 1969; Shu et al. 1973; Woodward 1975). The presence of dust lanes in the

spiral arms and the enhancement in ionized emission downstream, indicating regions of star formation, is attributed to this shock scenario. Such shocks are also thought to be the cause of the well defined molecular arms seen in many grand design galaxies, including M51. Numerical and analytical studies have provided predictions for the velocity and density profiles of the matter affected by the spiral gravitational perturbation (e.g Gittins & Clarke 2004; Kim & Ostriker 2002; Lubow et al. 1986).

There have been numerous observational studies addressing the nature of spiral structure that have focused on the gaseous components. Visser (1980b) showed that steady state density wave models fit the H I kinematics of M81 quite well. Lowe et al. (1994) used the modal theory of density waves to describe the spiral pattern in M81. Both Rand (1993) and Aalto et al. (1999) used observed molecular velocities along 1D cuts on the major and minor axes of the grand design spiral M51, and found qualitative agreement with the density wave models of Roberts & Stewart (1987). Kuno & Nakai (1997) fitted observed CO velocities from single dish observations to obtain gas streamlines. The smooth shape of the velocity profiles led them to conclude that galactic shocks do not exist in M51. However, the study by Aalto et al. (1999), using higher resolution interferometric data, found steeper velocity gradients, supporting the presence of shocks.

Yet, other observational studies have suggested that the arms are not long lived. In fact, the classic kinematic study of M51, that of Tully (1974), found evidence for a transient pattern in the outer disk, due to the interaction with its companion, but that a steady state is probably appropriate for the inner arms. Elmegreen et al. (1989) and Vogel et al. (1993) also suggested the presence of multiple pattern speeds. Henry et al. (2003) argued that the spiral pattern may be a superposition of an m=2 mode and a weaker m=3 mode, suggesting a transient pattern for the arms of M51.

This paper presents a detailed study of the gaseous velocity structure associated with the spiral pattern in M51. In a future paper, we will discuss and compare the spiral pattern

in different tracers. Here, we use the CO and Hα velocities to map the 2D velocity field in M51.

Our study makes use of the full 2D velocity field in M51 from interferometric CO and Fabry-Perot Hα observations, rather than just major and minor axis cuts. Noting that variations in the observed velocity field are mainly associated with the spiral arms, we fit the observed velocity field to obtain the radial and tangential components as a function of arm phase (i.e. distance perpendicular to the arm). We then analyze whether the fitted velocity field and density maps are consistent with the predictions of steady state theory.

In the next section we briefly describe our CO and Hα observations. In §2.3 we describe the method we employ to estimate the radial and tangential velocity components throughout the disk. Since our method is sensitive to the assumed values of the systematic velocity, major axis position angle, and disk inclination with respect to the sky, in §2.4 we present results from our effort to constrain these parameters, and describe how errors could affect the fitting results. In §2.5 we present and discuss the fitted profiles of radial and tangential velocities for a range of radii. We then use the velocity and density profiles to empirically test conservation of vortensity in §2.6.1. Next, in §2.6.2, we examine whether (quasi) steady state mass conservation is applicable, as would be necessary for a QSSS description. Finally, in §2.7, we summarize our conclusions.

2.2 Observations

The CO and Hα intensity and velocity maps are shown in Figures 2.1 and 2.2, respectively. The CO J=1-0 data for M51 were obtained in part from BIMA SONG (Survey of Nearby Galaxies). The observations and data reduction are described in Regan et al. (2001) and Helfer et al. (2003). The SONG map is based on 26 pointings and has an angular resolution of $5.8'' \times 5.1''$. Later, we obtained data for 34 additional pointings,

so that the spiral arms were mapped as far as the companion galaxy to the north and to a similar distance along the spiral arm to the south. In addition, inner fields were mapped in a higher resolution array (B array), yielding higher angular resolution. The newer data were reduced using the same procedures as described in Helfer et al. (2003) for BIMA SONG. Together the data sets cover 60 pointings. The maps used for this paper have variable resolution, reaching as high as $4''$ in the inner spiral arms but degrading to $6''$ – $13''$ in the interarms and in the outer arms.

Hα data were obtained with the Maryland-Caltech Palomar Fabry-Perot, which covered the optical disk at an angular resolution of $2''$ and a velocity resolution of 25 km s^{-1}. The observations and reduction are described in Gruendl (1996) and also Vogel et al. (1993). Both CO and Hα intensity maps are obtained by fitting Gaussian profiles to the spectrum at each location. The velocity maps indicate the velocity of the peak of the fit Gaussian intensity.

Also shown in Figures 2.1 and 2.2 are two lines tracing logarithmic spirals. The bright CO arm is well represented by a logarithmic spiral with a pitch angle of 21.1°. The weaker arm also generally follows a logarithmic spiral, although, as will be discussed, a number of its arm segments either lead or lag the depicted line. The logarithmic spirals will be discussed extensively in the following sections.

2.3 Estimation of Spiral Streaming Velocities

The observed line-of-sight velocity V_{obs} can be decomposed as a sum of terms involving the systematic velocity V_{sys}, the radial velocity v_R and the tangential velocity v_θ:

$$V_{obs}(R,\theta) = V_{sys} + [v_R(R,\theta)\sin(\theta-\theta_{MA}) + v_\theta(R,\theta)\cos(\theta-\theta_{MA})]\sin i, \qquad (2.1)$$

where R and θ are the galactocentric radius and azimuthal angle, and θ_{MA} and i are the position angle of the major axis and inclination of the galaxy, respectively. This equation

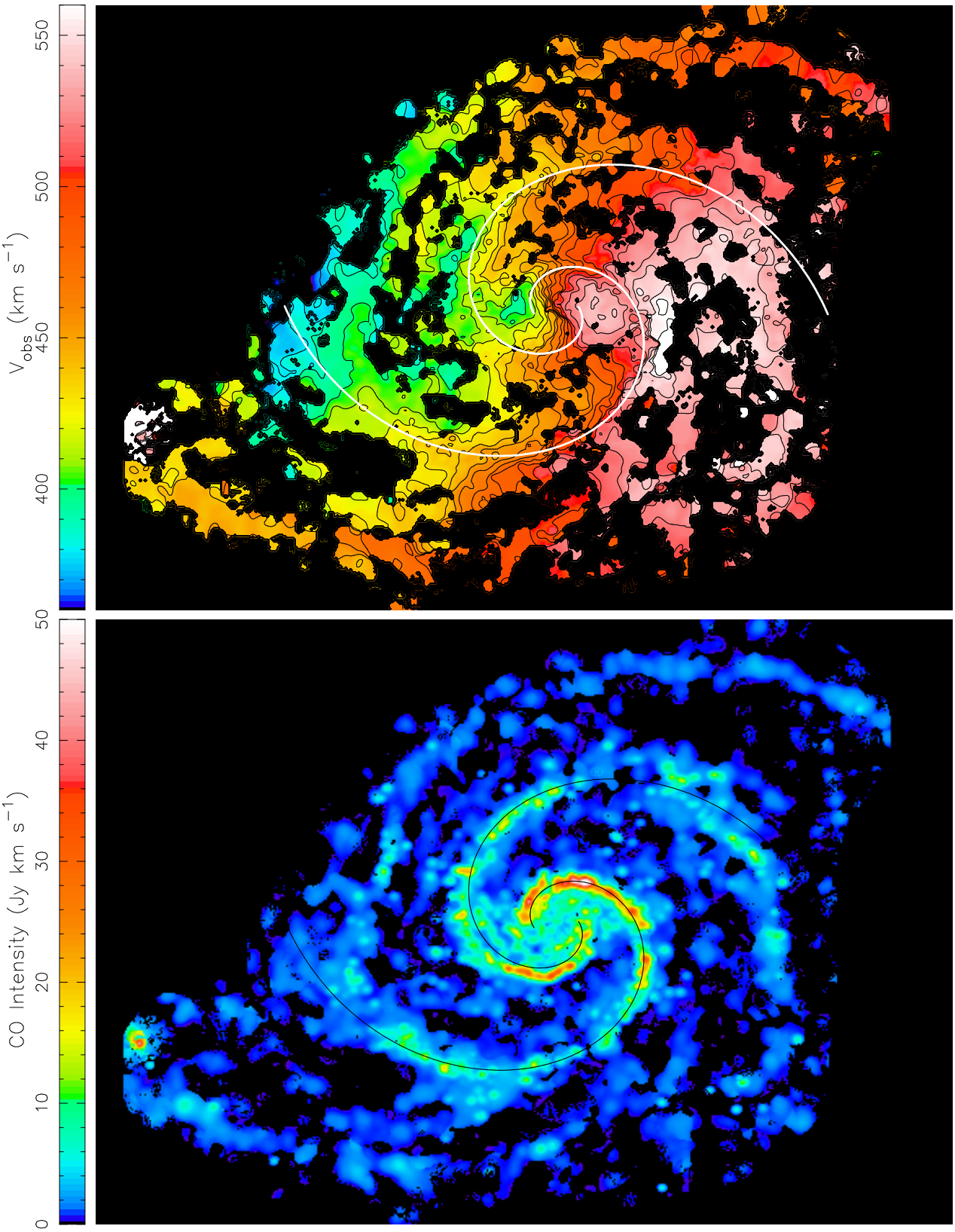

Figure 2.1: CO (1-0) velocity-integrated intensity (bottom) and velocity (top) maps of M51. Velocity contours increment by 10 km s^{-1}, between 360 and 560 km s^{-1}. Overlaid lines are logarithmic spirals with a pitch angle of 21.1°, separated by 180°.

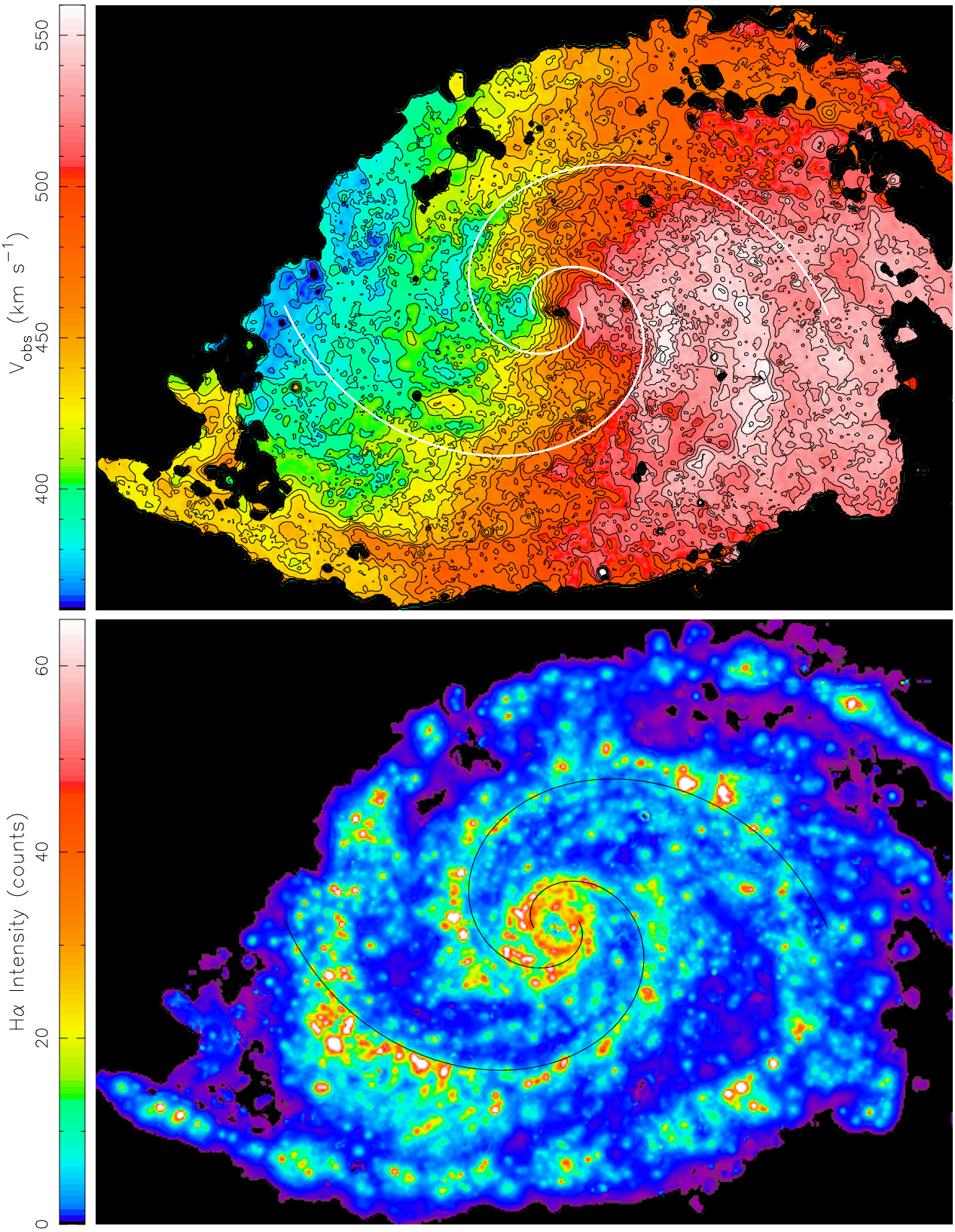

Figure 2.2: Hα velocity-integrated intensity (bottom) and velocity (top) map of M51. The overlaid spirals, as well as the velocity contours, are as described in Figure 2.1.

does not include a velocity component perpendicular to the disk. The exclusion of the vertical velocity component is reasonable since studies of face-on grand design spirals indicate that the z-component of velocity is less than 5 km s^{-1}(van der Kruit & Shostak 1982), provided the disk has no significant warp (we return to this issue in §2.4.2).

Inspection of the velocity maps indicates that the isovelocity contours near the spiral arms tend to run parallel to the arms. For a disk in pure circular rotation and with a flat rotation curve, on the other hand, the isovelocity contours of the projected velocity field are purely radial. It is evident that the velocity field of M51 is significantly different from this sort of simple "spider diagram," due to the non-axisymmetric perturbations associated with spiral streaming. Clearly, v_R and v_θ vary with azimuth.

Previous estimates of streaming velocities have used observed velocities near the major axis (where the projections of v_R vanishes) to estimate v_θ, and velocities near the minor axis (where the projections of v_θ vanishes) to estimate v_R (e.g., Rand 1993). However, much of the CO gas is organized into GMCs (giant molecular clouds) and larger complexes known as GMAs (giant molecular associations) (Vogel et al. 1988). Further, Aalto et al. (1999) have found that the streaming velocities of M51 GMAs in the same spiral arm have a significant dispersion. Observations along a single cut, e.g. the major axis, sample discrete GMCs and therefore may give a misleading estimate of the streaming velocities. As an alternative, an approach that fits a streaming profile to all the observed velocities in an annulus as a function of distance from the arm peak may better characterize the streaming velocities. Also, the gas surface density distribution varies significantly at any distance from the peak (i.e. the gas is clumpy), and so averaging parallel to the arm may better characterize the variation in gas surface density as a function of arm distance.

Typically, 2D fits to a galaxy velocity field assume that v_R and v_θ are constant along rings (e.g. the tilted ring analysis described in Begeman (1989)). By contrast, as mentioned earlier, v_R and v_θ do vary with azimuth, and indeed inspection of Figures 2.1 and

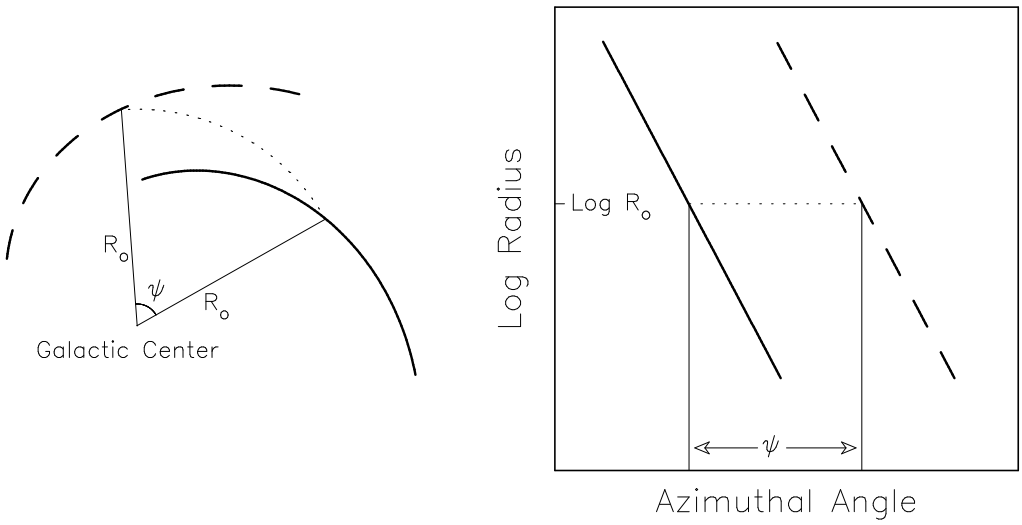

Figure 2.3: Geometry depicting the spiral arm phase ψ. The diagram on the left is the geometry in the plane of the galaxy. The phase, ψ, represents the angular displacement between two locations with equal galactocentric radius R_o for two congruent spiral segments. The diagram on the right is the logarithmic polar projection of the geometry on the left, showing the corresponding spiral segments.

2.2 indicates that the primary variations are due to the flow through the spiral arms rather than variations with galactocentric radius. As in most galaxies, the rotation curve of M51 is relatively flat; the radial variations that do occur are associated with spiral arm streaming. Thus, we are motivated to assume that radial variations of azimuthally-averaged quantities are negligible (at least over relatively limited radial ranges) and that v_R and v_θ vary primarily with spiral arm phase ψ. The left panel of Figure 2.3 shows the relevant geometry depicting the spiral arm phase. Our assumption is that v_R and v_θ are constant along narrow spiral arcs, such as the segments in Figure 2.3, that are congruent to the spiral arms. Thus, we rewrite equation (2.1) (for a limited range of radii) as

$$V_{obs} = V_{sys} + [v_R(\psi)\sin(\theta - \theta_{MA}) + v_\theta(\psi)\cos(\theta - \theta_{MA})]\sin i. \qquad (2.2)$$

In order to simplify the process of identifying regions of constant arm phase, we adopt a coordinate system in which the spiral arms are straight. Elmegreen et al. (1989) show that the spiral arms of M51 appear as straight line segments in a $(\theta, log(R))$, or logarithmic polar, coordinate system. The right panel of Figure 2.3 shows the logarithmic

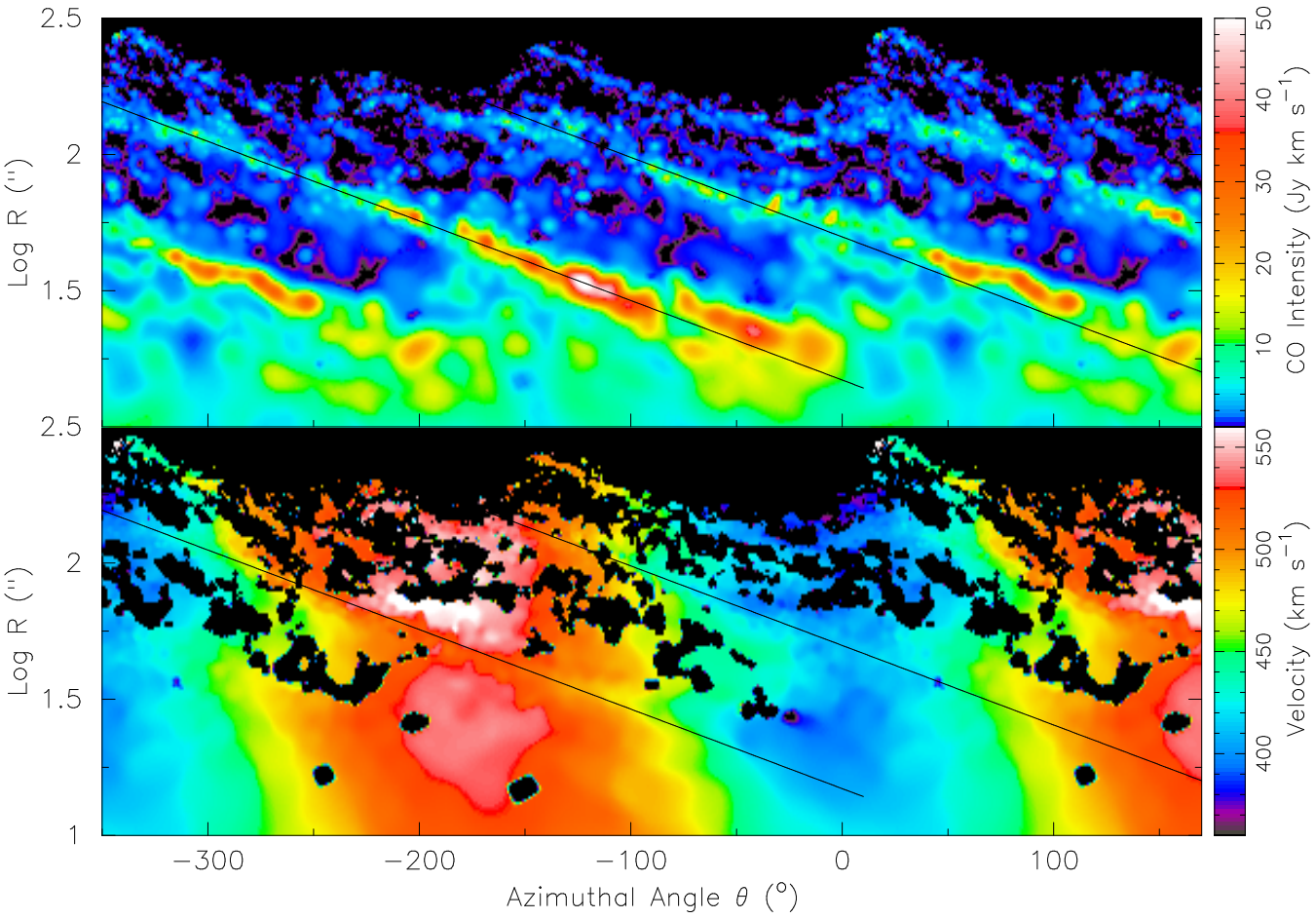

Figure 2.4: Logarithmic polar projections of the CO intensity and velocity maps. Though the origin of the abscissa (azimuthal angle) is arbitrary, in this case it is aligned with due North. The direction of rotation is to the right (counter-clockwise as seen on the sky). Also shown are the two logarithmic spiral lines positioned along the two spiral arms, which correspond to the lines overlaid on the maps of Figure 2.1.

polar diagram corresponding to the features in the left panel. Figure 2.4 shows the CO intensity and velocity maps of M51 in log-polar coordinates, and Figure 2.5 shows the corresponding Hα maps.

The sky images in Figures 2.1 and 2.2 are first deprojected before being transformed into a $(\theta, log(R))$ coordinate system. In order to deproject the sky view of a galaxy, the center position, position angle, and inclination are required. We initially use the canonical values for these parameters, which are listed in Table 2.1. We discuss the estimation of these parameters in the next section.

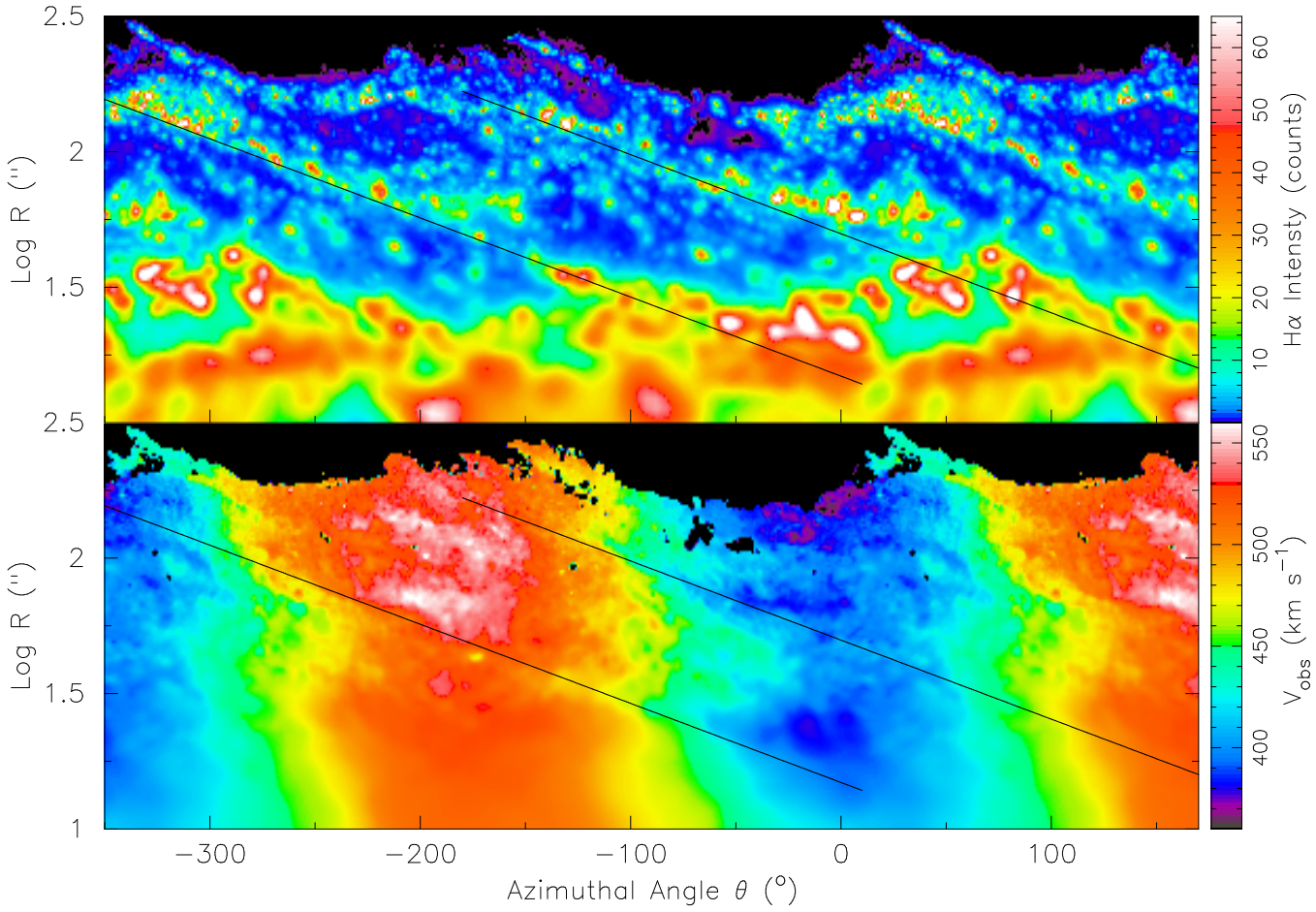

Figure 2.5: Logarithmic polar projections of the Hα intensity and velocity maps. Coordinate system and log spiral overlays are as in Figure 2.4.

Table 2.1. Initially Adopted Parameters for M51

Parameter	Value	Reference
Center RA (α) (J2000)	$13^h29^m52^s.71$	Hagiwara et al. (2001)
Center DEC (δ) (J2000)	$47°11'42''.80$	”
Systematic Velocity (V_{sys})	472 (LSR)	Tully (1974)
Position Angle of Major Axis (θ_{MA})	170°	”
Inclination (i)	20°	”

The two straight lines overlaid on Figures 2.4 and 2.5 indicate the adopted pitch angle of 21.1° and also correspond to the spiral loci shown in Figure 2.1. It is clear from the overlaid lines, which are separated by 180°, that the weaker arm is not symmetric with the brighter one, as discussed by Henry et al. (2003). Yet, both CO arms wrap around approximately 360° of the galaxy, even though they appear to jump in phase at one or more positions. The arms in Hα show more jumps in phase and variations in the pitch angle. In spite of their asymmetries, the CO spiral arms are particularly well described as logarithmic spirals, better even than Hα, or the optical arms shown by Elmegreen et al. (1989).

We will refer to overlaid logarithmic spiral arcs (or lines) as "slits," for we will extract observed CO and Hα velocities as a function of position along the arc (or line), similar to obtaining long-slit spectra. Each slit marks a region of constant arm phase ψ. Thus, while the observed velocity varies along the slit due to projection, v_R and v_θ are assumed constant. We arbitrarily define the arm phase marked by the leftmost slit in Figures 2.4 and 2.5 as $\psi = 0°$. The other CO arm appears at an arm phase of approximately ψ = 180°; other features such as the stellar arms and the gravitational potential minimum may of course be offset from the CO arms.

As noted previously, our fit will assume that the intrinsic v_R and v_θ are constant at a given arm phase, i.e. along a given slit, but that v_R and v_θ vary with ψ as the slit is translated in azimuth. Translating the slit amounts to shifting a straight line to the right in the logarithmic polar diagram; this direction of increasing azimuth is the same as the direction of rotation for M51. We then fit equation (2.2) to the observed velocities extracted at each arm phase ψ, thereby obtaining $v_R(\psi)$ and $v_\theta(\psi)$.

Although v_R and v_θ vary primarily with arm phase, they may of course also vary with radius. Therefore, we limit the radial range of an annulus (or equivalently the length of a slit) as much as possible while still fitting a sufficiently extended azimuth range to obtain

good leverage on both v_R and v_θ. In other words, an annulus should be sufficiently broad to cover the spiral arm both near the major axis and the minor axis; the width of the annulus thus depends on the pitch angle and galactocentric radius of the arm.

We first test our method by applying it to a model spiral galaxy with known radial and tangential velocities. The solid lines in Figure 2.6 shows the averaged density, v_R, and v_θ profiles in an annulus from a snapshot of a hydrodynamic simulation of a disk responding to a spiral perturbation. The model spiral galaxy is a 2D version of a 3D model described in detail in Gómez & Cox (2002), and the annulus used here extends from 8.38 - 8.92 kpc. The direction of gas flow is in the direction of increasing phase. As the gas approaches the arm, (marked by density maxima) the radial velocity, v_R, decreases by $\sim$40 km s^{-1}. The sign reversal of v_R indicates that the gas is moving away from the nucleus before the shock and towards the nucleus after the shock. As the gas emerges from the arm, the radial velocity increases again. The tangential velocity v_θ gradually decreases as the gas approaches the arm, then receives a strong boost and reaches a maximum just downstream from the arm.

In order to test the fitting algorithm, the model v_R and v_θ at all locations are used in equation (2.1) to create a model observed velocity field. This velocity field, along with the model density map, is transformed into logarithmic polar projections. Equation (2.2) is then fit to the model observed velocities at each arm phase in an annulus, using slits parallel to the spiral arms; the dashed lines in Figure 2.6 are the results of the velocity fits, in the same annulus (8.38 - 8.92 kpc). The results reproduce the overall shape of the velocity profiles quite well, although with slight phase shifts and offsets. The offsets and the shallower minimum in v_R are likely due to the variation of the pitch angle of the arms with radius; i.e. the spiral arms are not perfectly logarithmic, whereas the "slit" used to extract velocities at constant arm phase is. Despite these offsets, we were able to reproduce the major features of the velocity profiles of the model spiral galaxy, indicating

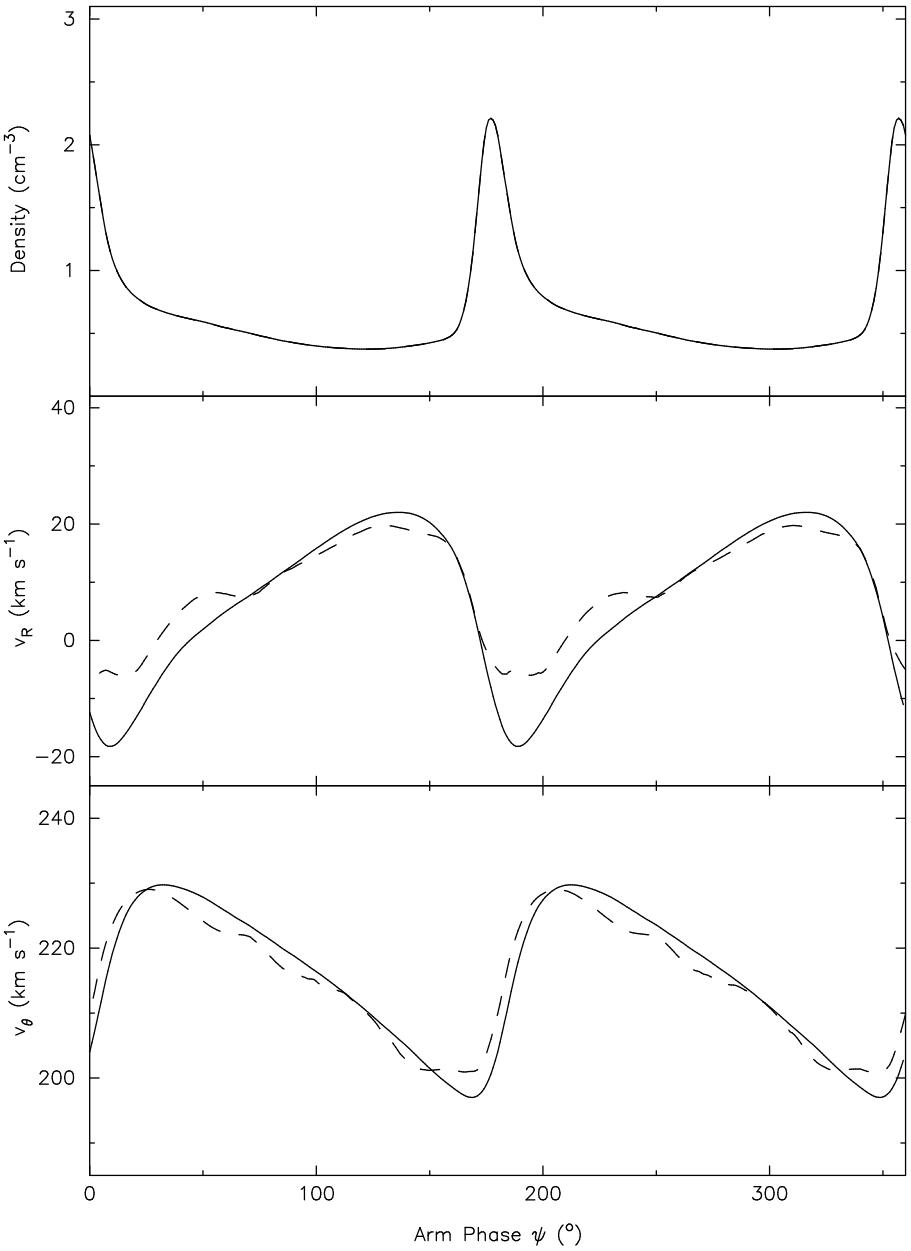

Figure 2.6: Gas profiles as a function arm phase ψ for a model spiral galaxy (see text). Solid lines: density (top), v_R (middle), and v_θ (bottom) profiles averaged at each arm phase, in an annulus extending from 8.38 - 8.92 kpc. The v_R and v_θ dashed lines in lower panels are obtained by fitting equation (2.2) to the "observed" velocities in the 8.38 - 8.92 kpc annulus.

that our method of fitting observed velocities at each arm phase recovers a 2D velocity field reasonably accurately.

We now apply our fitting method to the M51 data, adopting systematic parameters listed in Table 2.1. As an example, Figure 2.7 shows the v_R (top) and v_θ (bottom) fits to the observed CO and Hα velocity field for one annulus between the galactocentric radii of $21''$ and $36''$. The CO intensity averaged along a slit as a function of phase angle ψ is also shown as dashed lines, indicating the distribution of molecular gas. As mentioned, $\psi = 0^\circ$ is arbitrary and is marked by the leftmost line in Figures 2.4 and 2.5, corresponding to the brighter arm, which we will refer to as Arm 1. We show a phase range greater than 360° so that both upstream and downstream velocities can easily be seen for both arms. The direction of gas flow through the arms (assuming we are inside corotation) is from left to right, so that the right sides of the CO peaks correspond to the downstream side of the arm. In most cases, as the gas flows through the arm, the radial velocity decreases and then increases, and the tangential velocity receives a boost, as predicted qualitatively by density wave theory.

In a conventional tilted-ring velocity fitting analysis, galaxy parameters such as the inclination, position angle, dynamical center, and systematic velocity can be directly fit. However, even though the inclination and position angle appear explicitly in equation (2.2), for our fits all but the systematic velocity must be assumed prior to deprojecting a galaxy velocity field and therefore before the fit. For our initial fits we employed the standard assumed values for these parameters for M51, shown in Table 2.1. In the next section we explore the effects of errors in these assumed global parameters on the estimation of v_R and v_θ.

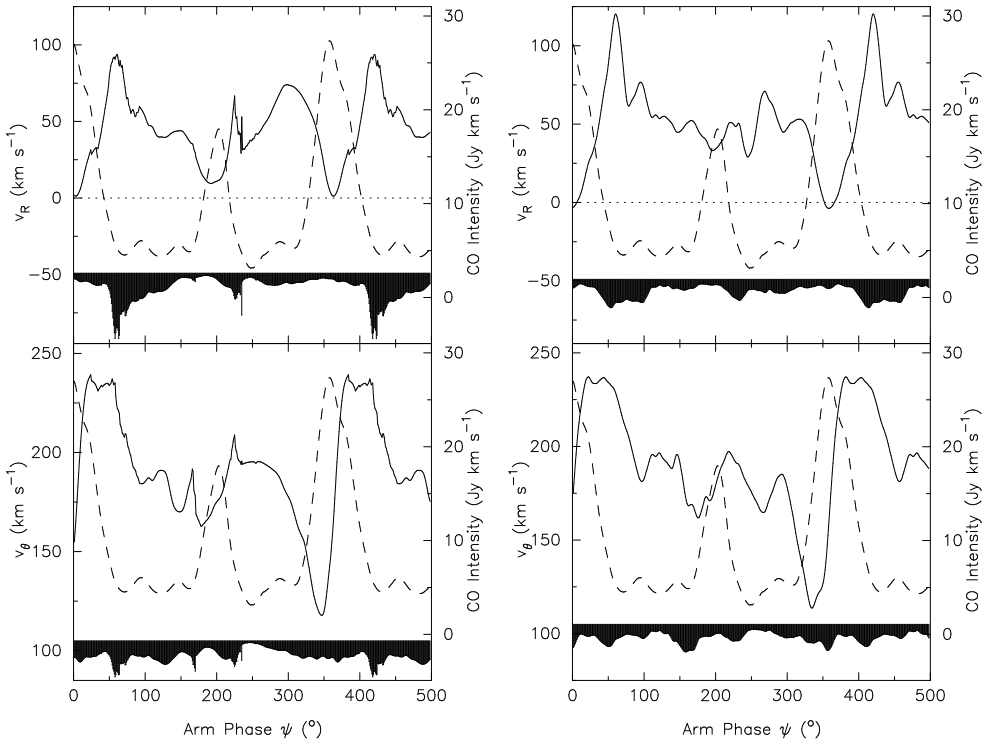

Figure 2.7: CO (left) and Hα (right) v_R and v_θ fits as a function of arm phase for an annulus with an inner radius of 21″ and an outer radius of 36″. The one sided 3σ error-bars are also shown on the bottom of each panel. Dashed lines are the corresponding mean CO velocity integrated intensities, with the scale depicted on the right ordinate. Table 2.1 shows the fixed (canonical) parameters used in obtaining these fits.

2.4 Method Testing and Parameter Constraints

To test the sensitivity of the v_R and v_θ fits to errors in the global (fixed) parameters, we generated test velocity fields and created sky projections with known parameters. We then applied our fitting technique to estimate v_R and v_θ for the model galaxies, assuming incorrect values for the fixed parameters, and compared the fitting results to the actual model values of v_R and v_θ. This enables us to quantify the sensitivity of the fits to the fixed parameters. In addition to constraints obtained from fitting our kinematic data, we also use standard methods to constrain the values of V_{sys}, θ_{MA}, and i. As we shall show, one of our conclusions is that some of the basic parameters for M51, many of which date to Tully (1974), may in fact be poorly constrained due to the morphological and kinematic

perturbations induced by the tidal interaction with its companion.

As an initial test, we generated a simple model with $v_\theta = 240$ km s^{-1} and $v_R = -35$, i.e. an axisymmetric disk with a flat rotation curve and uniform radial inflow. We refer to this model as the "constant velocity" model. We apply our general method to fit v_R and v_θ as a function of arm phase using "observed" velocities. If we assume the input values of $V_{sys} = 464$ km s^{-1}, $\theta_{MA} = 170^\circ$, and $i = 20^\circ$, we indeed recover the input values for v_R and v_θ as independent of phase. We now consider the effects of assuming incorrect values for the parameters.

2.4.1 Position of Dynamical Center

In testing the sensitivity of the fits to the assumed center position, we applied the fitting algorithm to a model for which the center position was shifted by $1''$ in both RA and DEC. We found that a $1''$ error in the assumed center has a negligible effect on the fit velocities. BIMA observations have an astrometric accuracy of $\sim$10% of the synthesized beam. The highest resolution of our CO observations is $4.5''$, so the error in position will likely not be greater than $\sim 0.5''$. Thus, observational errors will likely not affect the results of our fits. For all the analysis that follows, we will adopt the center position listed in Table 2.1. This choice assumes that the dynamical center coincides with the location of a weak AGN known to exist in the nucleus of M51 (Ho et al. 1987; Nakai & Kasuga 1988). We use the position of the radio continuum source observed with the VLA, which has an accuracy of $\pm 0.''01$ (Hagiwara et al. 2001).

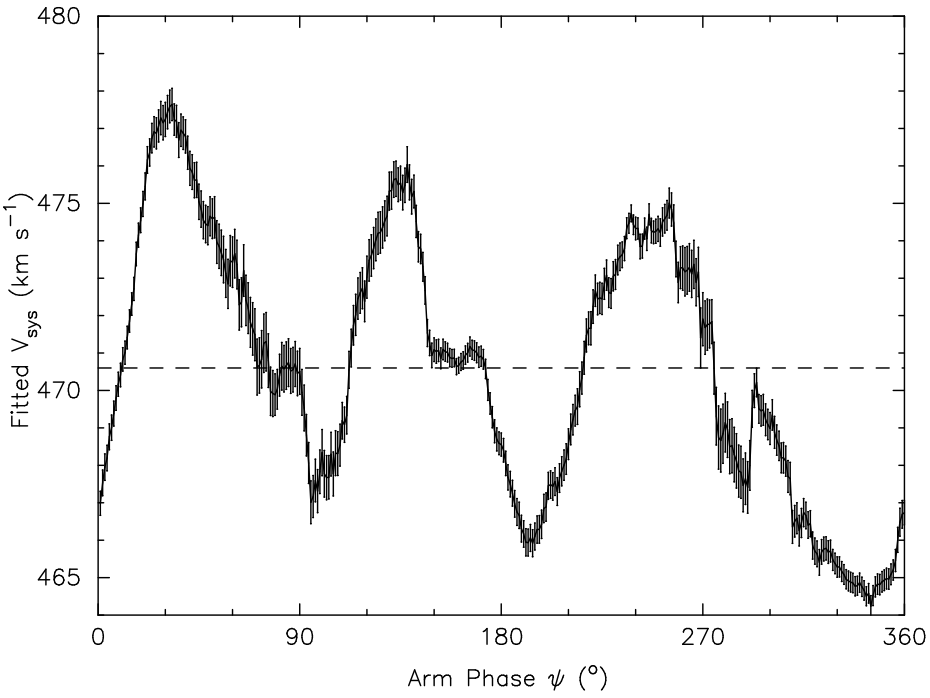

Figure 2.8: Result of fit to M51 CO velocity data in which V_{sys}, v_R, and v_θ were allowed to vary. The radial range of the annulus is 14″ - 136″. The fact that the fit value of V_{sys} varies with phase ψ shows that other parameters (e.g. i, θ_{MA}) vary with radius within the annulus. The mean of the fits is 470.6 km s^{-1} (LSR), shown by the dashed line.

2.4.2 Systematic Velocity

Before discussing methods for determining V_{sys}, we first explore the effect that an error in an assumed value of V_{sys} would have on fits for v_R and v_θ in which V_{sys} is held fixed, using the constant velocity model. As expected, an error ΔV_{sys} in the assumed V_{sys} produces a sinusoidal variation in both fitted velocity components, with an amplitude of $\Delta V_{sys}/\sin i$, and a period of 360°(see eqn. 2.1). Clearly, V_{sys} needs to be well determined.

One approach to obtaining V_{sys} is to fit the data for its value using equation (2.2). Figure 2.8 shows the results of fits to the M51 data in which V_{sys} was fit, along with v_R and v_θ, as a function of arm phase. Although V_{sys} should be constant, it can be seen that the fit value of V_{sys} varies with arm phase. Similar variations in fitted V_{sys} result regardless of what values of the position angle and inclination are assumed.

One possible explanation for the apparent variation of V_{sys} is that the galactic disk of

M51 is twisted and/or warped, i.e. the position angle and/or inclination may vary with radius. We therefore compare the results of fitting for V_{sys} from a model galaxy with no warp to a model with a warp. We again make use of the constant velocity model, for this model also represents an unwarped disk. Instead of keeping V_{sys} fixed, we allowed this parameter to be free in the fit. If we use the true position angle and inclination, we correctly recover the adopted values for all three free parameters, V_{sys}, v_R, and v_θ.

To generate a warp model, we increase i monotonically from 25° at the inner radius (100″) to 35° at the outer radius (200″); the position angle is kept fixed. If we allow V_{sys} to be free in fitting the model data, Figure 2.9 shows that the V_{sys} varies almost sinusoidally about the true model value 400 km s^{-1}. The mean fitted systematic velocity is equal to this value. This is the case regardless of what values of inclination or position angle we use (within reasonable limits), and regardless of the radius range of the annulus used for fitting. Thus, regardless of the assumed fixed parameters and of the limits in radius, for a simple warp the mean value of the fits gives the correct systematic velocity.

Motivated by our finding that even with a warp the average fit value of V_{sys} gives the true value, we calculated the mean of the V_{sys} values shown in Figure 2.8, obtaining V_{sys} = 470.6 km s^{-1}. Comparison of the V_{sys} fits of the actual M51 data (Figure 2.8) with V_{sys} fits to the simple warp model (Figure 2.9) shows that the warp model has a slower variation. Hence, if a warp is responsible for producing variations in the fitted systematic velocity it must be more complex than our simple model; we return to this question in §2.6.2.

We therefore apply two additional methods to estimate the value of V_{sys}. The first method is based on a standard tilted-ring analysis (Begeman 1989), in which the galactic disk is represented as a series of nested tilted rings. In its most general form, each tilted ring may have a different center, systematic velocity, position angle, inclination, and rotational velocity. We use 10″ rings from an inner radius of 20″ to an outer radius of 120″,

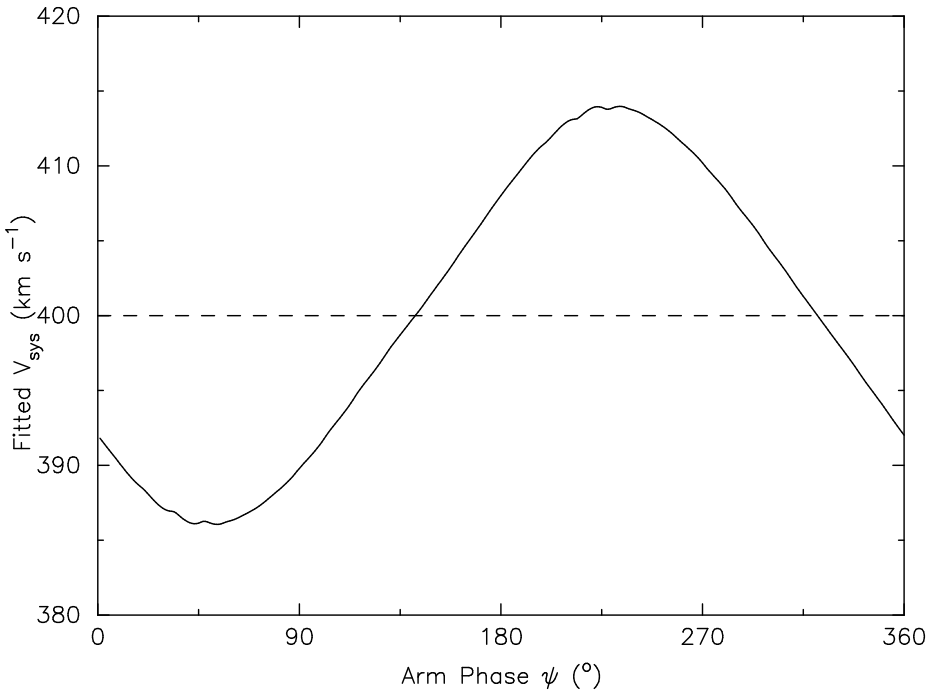

Figure 2.9: Fit V_{sys} as a function of arm phase, similar to Fig. 2.8, but for a model galaxy with a warp. The systematic velocity adopted for the model is 400 km s^{-1} (dashed line), equal to the mean of the fits (solid line).

fixing the center position, inclination, and position angle to the values in Table 2.1. We obtain mean systematic velocity of 471.4 ± 0.5 km s^{-1}. When we allow the position angle to vary as well, we obtain a mean of 471.3 ± 0.3 km s^{-1}.

A third method we use to constrain V_{sys} is to assume a functional form for the rotation curve, using the `NEMO` program `rotcurshape` (Teuben 1995). In contrast to the tilted-ring method, which fits each ring independently, `rotcurshape` fits V_{sys}, θ_{MA}, i, center position α and δ, and the coefficients of the function used to describe the rotation curve simultaneously to the entire velocity field. Therefore, it can yield a single V_{sys} that best fits the entire velocity field. It is particularly useful for finding V_{sys} if the kinematic center position can be fixed. For this fit, we limit the `rotcurshape` fit to the inner $20''$ in radius. This is inside the main spiral arms, in the region where the rotation curve is rising and the isovelocity contours are relatively straight. We assume the center, θ_{MA}, and i listed in Table 2.1 and a rotation curve of the form $v = V_{sys} + v_o x/(1+x)$ where x is the ratio

Table 2.2. Estimation of the Systematic Velocity of M51

Method	V_{sys} (km s^{-1})[a]	Error (km s^{-1})
Tully (1974)	472	3
Freeing V_{sys} in fitting for $v_R(\psi)$ and $v_\theta(\psi)$	470.6	0.4
Tilted Rings Analysis	471.4	0.5
Rotation Curve Fitting	473.3	0.5
Weighted Mean	471.7	0.3

[a]Velocity in LSR frame

of the radius to the core radius, and fit for V_{sys}, v_o, and the core radius. We obtain V_{sys} = 473 ± 0.5 km s^{-1}. If we allow the position angle to vary as well, we obtain 473.2 ± 0.3 km s^{-1}. It is encouraging that this is within 2 km s^{-1}of V_{sys} determined from the other two methods even though this fit uses a different method and fits an entirely different region (i.e. the inner 20″, inside the main CO arms, as opposed to outside 20″).

The canonical value of V_{sys} for M51 is 472 ± 3 km s^{-1} (Tully 1974, and references therein). Table 2.2 lists Tully's value for V_{sys} as well as the results from applying the three techniques described above. Our different methods give a mean systematic velocity of 471.7 ± 0.3 km s^{-1}. Henceforth, we will fix V_{sys} to be 472 km s^{-1} (LSR, corresponding to a heliocentric velocity of 464 km s^{-1}) in fitting the velocity field to estimate $v_R(\psi)$ and $v_\theta(\psi)$.

2.4.3 Position Angle

To investigate the effect of errors in the assumed galaxy position angle on the fitted values of v_R and v_θ, we first use the aforementioned constant velocity model. Note that the position angle is required to deproject the galaxy image, as well as in equation (2.2). Using incorrect position angles, but correct model values of systematic velocity and inclination,

yields a greater effect on v_R than on v_θ. This is because an error $\Delta\theta_{MA} \ll 1$ in θ_{MA} results in an error $\approx -v_\theta \sin\Delta\theta_{MA}$ in the fitted v_R, whereas the corresponding error in v_θ is $\approx +v_R \sin\Delta\theta_{MA}$. Since v_θ is large compared to v_R, the shift in v_R is larger than the shift in v_θ. Thus , a $\pm 10^\circ$ error in position angle in the "constant velocity" model that has v_θ = 240 km s^{-1} produces approximately a ∓ 40 km s^{-1} shift in the fitted radial velocity. Position angle errors also produce small perturbations in both velocity components. We conclude that using an accurate value of θ_{MA} is very important to obtain accurate v_θ and especially v_R fits.

Unfortunately, the position angle of the major axis of M51 is particularly difficult to determine. The strong spiral arms and the tidal interaction with NGC 5195 distort the stellar disk, making it effectively impossible to determine a position angle from the orientation of the isophotes. Thus, it is necessary to go beyond morphology in determining θ_{MA}. We therefore revisit the determination of the galaxy's position angle. We apply the method of Tully (1974) to our velocity data from Hα and CO observations. We also study the effect of streaming motions on this method by using model galaxies with known position angles and streaming velocities. In addition, we also apply two alternate methods to derive the position angle.

The widely used value for the position angle of M51, 170°, was determined by Tully (1974) using kinematic information. Tully assumed that the observed velocity should reach its extreme value at the position angle of the galaxy major axis, θ_{MA}. To determine θ_{MA}, he averaged the observed velocities in wedges extending over 5° in azimuth, and then for each radius took the position angle of the wedge with the extreme velocity as the estimated major axis at that radius. Tully excluded radii at which he was not confident that the true major axis had measured velocities (e.g. the faint interarm regions near the major axis).

Figure 2.10 shows the results of applying Tully's position angle determination method

to Hα and CO observations. For each annulus of radial extent 5″, the position of the wedge with the extreme velocity is marked. Due to the lack of data in the outer regions of the CO observations, only the wedges in the inner 70″ provide reliable measures of the position angle of the extreme velocity. Similar to Tully, we did not attempt to estimate the position angle of the extreme velocity at radii for which data are sparse in the range of plausible position angles of the major axis. From the location of these extreme velocity wedges, we found θ_{MA} to be 172° (from an error weighted average) from both CO and Hα observations.

However, streaming motions can shift the velocities, resulting in the extreme velocity occurring at position angles not corresponding to the true major axis. Indeed, inspection of positions of the velocity extremum wedges overlaid on the intensity maps shows that the position angles of the wedges in the interarms are clearly shifted counter-clockwise from those in the arms. This is most evident in the Hα maps, for which emission is detected from almost everywhere in the disk. We further explore streaming effects on the Tully method using a model with known streaming motions, generated using one of our v_R and v_θ fits to the M51 CO data, with θ_{MA} = 170°. (Since this test is designed simply to reveal the twists in the apparent position angle due to streaming, the particular value assumed for the true position angle and the particular v_R and v_θ fits used is not significant.) Figure 2.11 shows the results of applying Tully's method to this streaming model galaxy. In any given annulus, the extreme velocity averaged in the 5° wedges occurs in the interarm regions. In Tully's analysis, however, only spiral arm regions (near the apparent major axis) were considered, due to observational limitations. Therefore, the major axis position angle he found is likely biased clockwise from the true major axis. As shown in Figure 2.11, even if the interarm regions are considered, the position angles of the locations of the extreme velocities do not necessarily correspond to the major axis. Thus, such an extrema method can be biased due to the inherent streaming in M51,

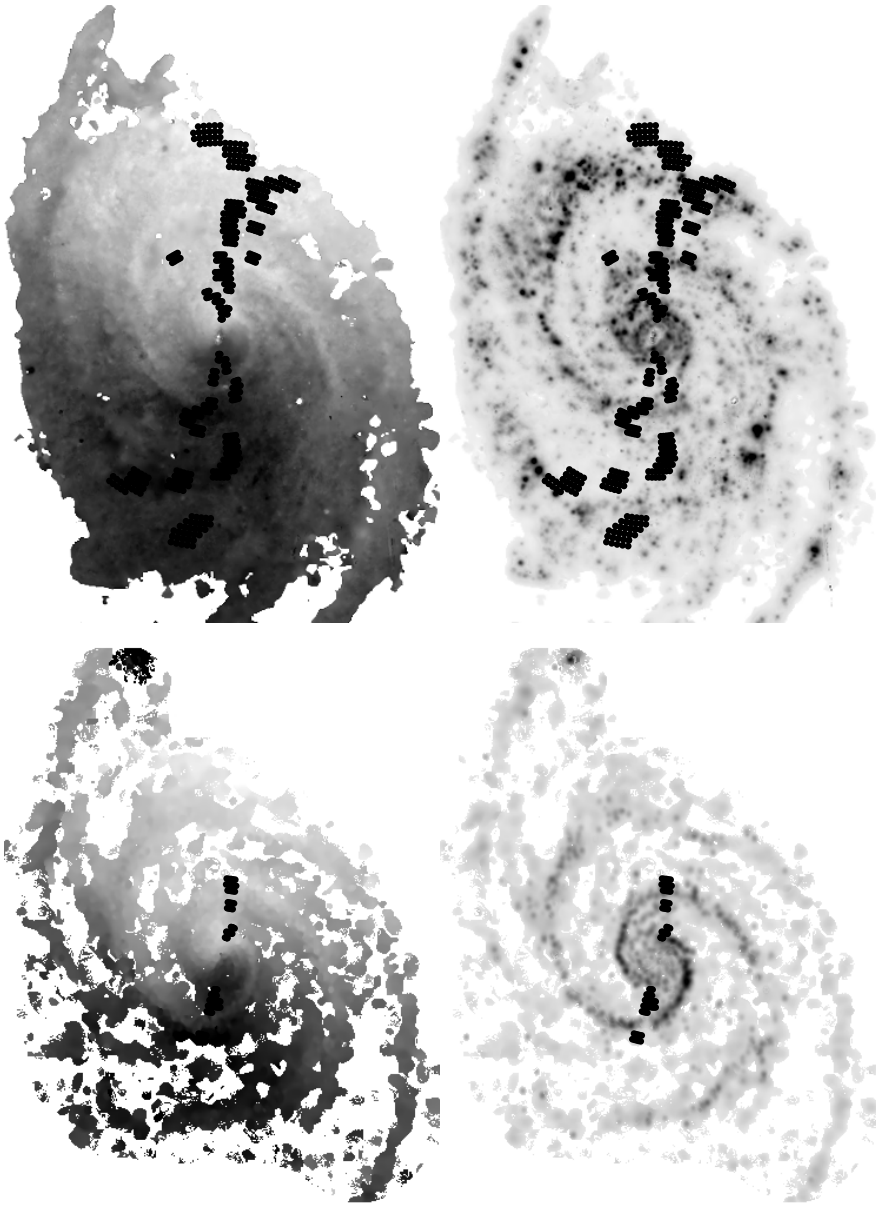

Figure 2.10: Tully "wedge" method for estimating galaxy position angle. The extreme velocity for each 5″ annulus, averaged in 5° wedges, is marked. The upper panels show the Hα velocity (left) and velocity-integrated intensity (right); lower panels show the same for CO. For CO, emission was too weak to apply the method at some radii, especially in the outer galaxy.

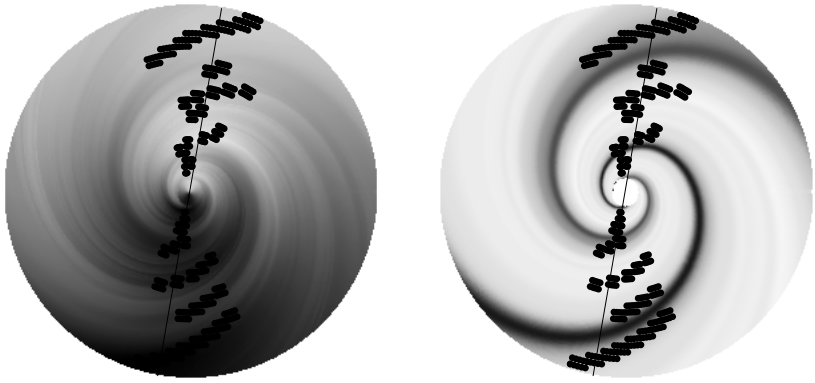

Figure 2.11: Application of Tully wedge method to a model with streaming. The velocity field is shown (left) along with the corresponding intensity map (right). The position angle assumed in the model is 170°, shown by the solid line. The 5° wedges with the extreme velocity for each annulus is marked. It can be seen that streaming shifts the estimated position angle from the true position angle. Note that the extreme velocities do not occur in the arm.

regardless of whether the arms or interarms are considered.

We employ two alternate position angle determination methods that make use of the full observed velocity field. In the first method, we average the observed velocity at each position angle in a wedge for both the northern and southern sides of the galaxy; then we fit a cosine curve to these averaged velocities as a function of azimuthal angle. We will refer to this method as the "radial-averaged" method. This is most easily accomplished in the polar projection, where we can average along a column to perform the radial average. The radial-averaged velocity as a function of position angle is shown in Figure 2.12, along with the corresponding cosine fitted curves. We assume that the galaxy major axis should be at the position angle of the extrema of such curves. The mean position angle determined from the Hα and CO fits is $\sim$177°, larger than the position angle determined by the Tully method. Again, the position angle determined in such a way is sensitive to streaming. Earlier we showed that streaming tends to cause the position angle of extreme interarm velocities to be biased counter-clockwise from the true value. Since the interarms occupy a greater fraction of the galaxy compared to the arms, streaming will introduce a counter-clockwise bias to the apparent position angle of the major axis. The effect of

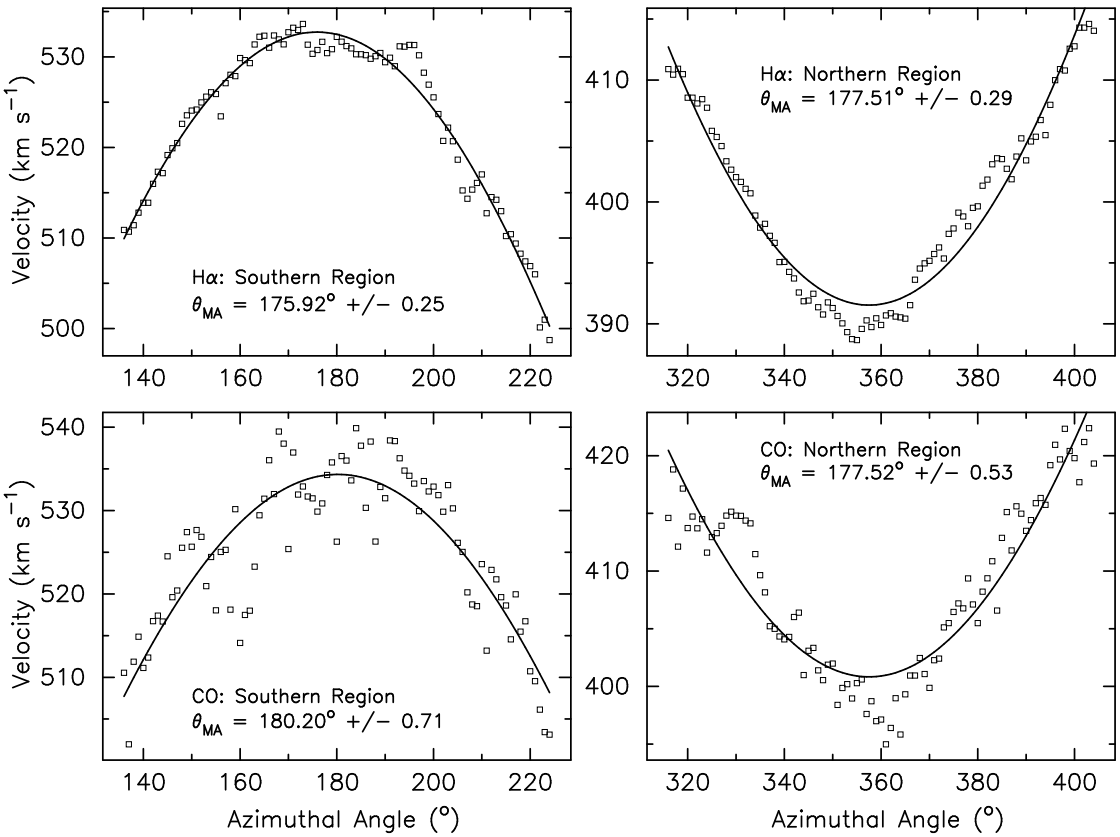

Figure 2.12: Mean observed velocity plotted vs azimuthal angle. All observed velocities were averaged over radius at each azimuth. Velocities are fit by cosine functions (solid line); extremum of the cosine curve indicates the best fit position angle of the major axis.

streaming on this method is further discussed below, following a discussion of our second position angle determination method.

Our second method to determine the position angle, the "azimuthal fit" method, is similar to the one described in the previous paragraph, but instead the cosine curve is fit to the observed velocities along a projected circle with constant (projected) radius. As in the previous method, the polar projection of the velocity field is useful; in this case we simply fit a cosine curve to the velocities along a row of constant projected radius. The results from applying this method are shown in Figure 2.13. Note that the position angle of the velocity extrema varies systematically as a function of radius; it is approximately 180° in the inner region 30″ from the center, declining to 165° 120″ from the center; this trend, including the rise near Log(R) = 1.7, is also evident from simple inspection of

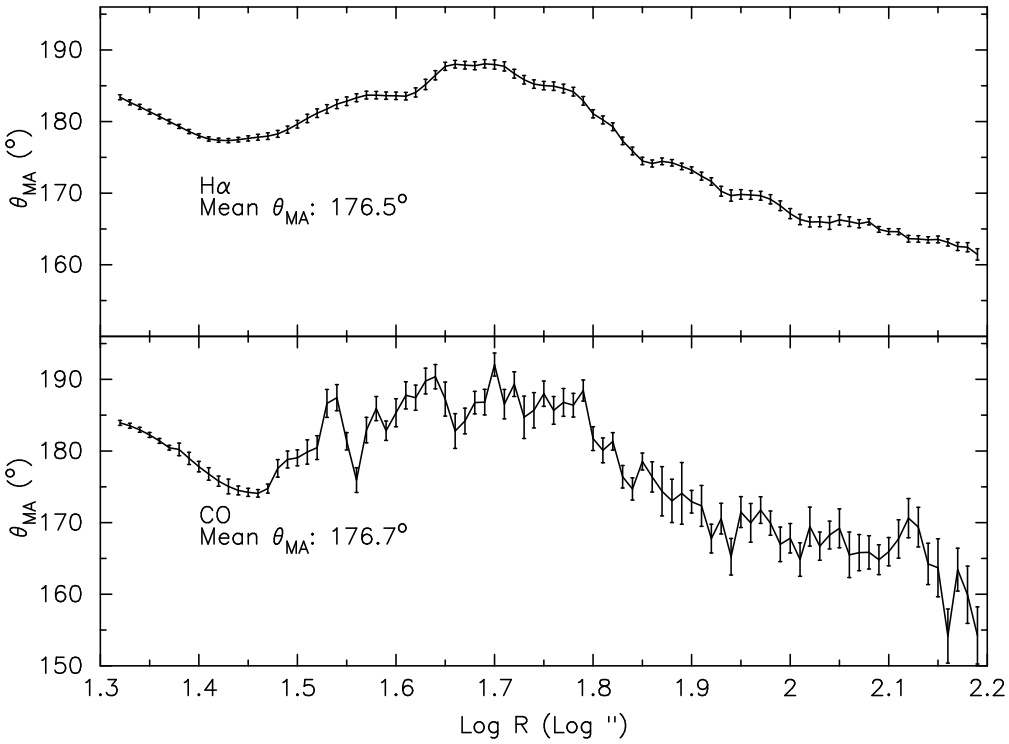

Figure 2.13: Fit position angle of the major axis θ_{MA} as a function of galactocentric radius from Hα (upper) and CO (lower) velocity fields. The position angles were obtained by fitting a cosine function to the distribution of observed velocity vs azimuthal angle at each radius.

Figures 2.4 and 2.5. Averaging over the radius range displayed in Figure 2.13, we obtain the same position angle of $\sim$177° as in the previous method. Again, the velocities in the interarms bias this determination of position angle, for the same reasons stated in the previous paragraph.

In order to understand the effect of streaming motions on the position angle of the major axis derived using the radial averaged and azimuthally fit methods, we apply these methods to streaming models with known position angles and streaming velocities. The model velocity fields are produced from our v_R and v_θ profiles obtained by assuming fixed values of θ_{MA}; we then apply the radial averaged and azimuthally fit methods to these model velocity fields. Both methods recover a θ_{MA} of $\sim$176°, for all models, similar to the actual M51 velocity field, even though the position angles assumed in generating the streaming models can be very different. This is because for different position angles,

the streaming velocities were derived from fits designed to best match the observed velocities. So in fact all the streaming models give virtually identical observed velocity fields regardless of assumed position angle.

However, if we recreate the models setting the radial component to be zero everywhere, then we correctly recover the assumed position angles. This is clear evidence that radial streaming affects methods to determine θ_{MA}, not only near the minor axis, as recognized by Tully, but also elsewhere including even the major axis.

In order to quantify the effect of the non-zero radial velocities on the apparent position angle, we apply the position angle determination methods to models with known constant radial velocities. In these artificial models tangential streaming velocities are assumed to vary with arm phase, but radial streaming is assumed constant. We found that for every ± 10 km s^{-1} in radial velocity, the derived position angle differs from the actual position angle by $\pm$ 3°. This degeneracy between the position angle and radial velocity renders it difficult to accurately identify the true position angle, or to map the radial velocity. In order to accurately determine the position angle, we need to know the radial streaming. But in our effort to map the radial and tangential velocities of M51, we need to know the position angle. Thus, as we carry out our investigation, we shall use a range of position angles in deriving the two dimensional velocity components of M51.

2.4.4 Inclination

Estimating the inclination based on the orientation of the isophotes is unreliable, as discussed in §2.4.3, due to the strong perturbations from the spiral arms and the tidal interaction. In principle, the inclination can be determined from a fit to the velocity field, as we did to obtain the systematic velocity in §2.4.2. However, the fit inclination is not well determined by the available data, presumably due to the streaming. To test the sensitivity of the v_R and v_θ fits to the inclination, i, in equation (2.2), we assume incorrect values of

the inclination that differ from the true value by Δi for the constant velocity model (where v_R and v_θ are constant). We then fit for v_R and v_θ. As expected, an error Δi results in errors in the fit value of v_R and v_θ with magnitudes $\propto \sin\Delta i$, along with small perturbations about this offset.

Since we find that error introduced in the velocity components due to an incorrect inclination can be large (although just a simple scaling), we sought other constraints on the inclination. In particular, the Tully-Fisher (Tully & Fisher 1977) relation can be used to estimate the inclination. The well known Tully-Fisher relation is a correlation between galaxy luminosity and maximum rotation speed. The inclination can be estimated by comparing the rotational velocity predicted by the Tully-Fisher relation with the observed velocity of the flat part of the rotation curve. We use the baryonic form of the Tully-Fisher relation discussed by McGaugh (2005) (see also McGaugh et al. 2000):

$$M_b = 50 V_c^4, \tag{2.3}$$

where M_b is the baryonic mass (in $M_\odot$), and V_c is the circular rotational velocity (in km s^{-1}). Since the dispersion in the Tully-Fisher relation, $L \propto V_c^4$, is relatively small, given the luminosity the uncertainty in V_c is small.

In order to determine the baryonic mass M_b, we require the stellar mass M_*, which is related to the B-band luminosity L_B and the B-band mass to light ratio (M/L_B),

$$M_* = L_B \cdot (M/L_B). \tag{2.4}$$

We use the correlation of the galaxy color with M/L discussed by Bell & de Jong (2001) applicable to the Charlot & Bruzual (1991) population synthesis models, to obtain (M/L_B):

$$(M/L_B) = 10^{[-0.63+1.54(B-V)]}. \tag{2.5}$$

The RC3 catalog (de Vaucouleurs et al. 1991) gives $(B-V) = 0.53$ for M51, so (M/L_B)=1.54.

The last quantity required to determine M_* is the luminosity L_B, which can be derived if we know the distance. Two independent studies have given similar M51 distance estimates: observation of planetary nebulae gives a distance modulus of $m-M$=29.62 $\pm$ 0.15 (Feldmeier et al. 1997), and a study of surface brightness fluctuations in the companion NGC 5195 gives $m-M$=29.59 $\pm$ 0.15 (Jensen et al. 1996). We thus employ a distance modulus of $m-M$= 29.6, corresponding to a distance of 8.4 $\pm$ 0.6 Mpc. Using the RC3 catalog value of $B = 8.67$, corrected for extinction,

$$L_B = 10^{-0.4(8.67-29.6-5.48)} L_\odot = 3.66 \times 10^{10} L_\odot. \tag{2.6}$$

Using this value and the (M/L_B) value of 1.54 (equation [2.5]) in equation (2.4), we obtain

$$M_* = 5.64 \times 10^{10}\,\mathrm{M}_\odot. \tag{2.7}$$

We can now apply the McGaugh (2005) relation in equation (2.3) to obtain the circular velocity:

$$V_c = [(M_* + M_{gas})/50]^{1/4} = 188\ \mathrm{km\,s^{-1}}, \tag{2.8}$$

where M_{gas} is the total gas mass; in the case of M51 the gas is predominantly molecular. From our CO observations, we compute $M_{gas} = 5.4 \times 10^9$ $\mathrm{M}_\odot$, using an X-factor of of 2×10^{20} cm^{-2} [K km s^{-1}]$^{-1}$ (e.g. Strong et al. 1988). Due to the small value of the exponent in equation 2.8, errors in the mass, due to variations in the X-factor, for example, will not significantly affect the resulting rotational velocity.

The observed velocity is related to the circular velocity by

$$V_{c,obs} = V_c \sin i. \tag{2.9}$$

Adopting the center, θ_{MA}, and V_{sys} described in this section, we apply a tilted-ring analysis to determine the flat part of the rotation curve. We obtain an observed circular velocity between 70 and 80 km s^{-1}, implying

$$22^\circ \lesssim i \lesssim 25^\circ \tag{2.10}$$

Therefore, for our subsequent fits, we adopt an inclination of 24°.[1]

2.4.5 Summary: System Parameter Values

In summary, we have shown that the fit values of v_R and v_θ are sensitive to the assumed values for the fixed parameters in equation (2.2), V_{sys}, θ_{MA}, and i. Uncertainties in the assumed position of the dynamical center are too small to significantly affect the derived streaming velocities. We have used three different methods to determine V_{sys}, which resulted in a value similar to the V_{sys} found by Tully. We have found it to be extremely difficult to constrain the value of the position angle of the major axis using the velocity field, due to the significant streaming that shifts the position angle of the extreme velocities. As a result, in fitting for v_R and v_θ, we allow for a range of plausible position angles. Lastly, we adopt an inclination of 24°, which is determined by using the baryonic Tully-Fisher relation (McGaugh et al. 2000) between the baryonic mass and rotational velocity. To estimate v_θ and v_R, we thus use the center position and systematic velocity listed in Table 2.1, but use a range of position angles and an inclination of 24°.

2.5 Results: Velocity Profile Fits

With our improved estimates of the global parameters, we apply the fitting algorithm to the observed velocity field in different annuli to determine the radial and tangential velocities v_R and v_θ as a function of arm phase ψ. We initially adopt a position angle θ_{MA} of 170°. We address the issue of a varying θ_{MA} in §2.6.2. Figures 2.14 and 2.15 show the CO and Hα v_R and v_θ fits in six overlapping annuli between a galactocentric radii of 21″ and 105″, and Figure 2.16 shows the corresponding overlapping annular regions.

[1]Employing the standard Tully-Fisher relation instead, we obtain a mean inclination of ∼23°, using the slope and zero-point fits from Verheijen (2001).

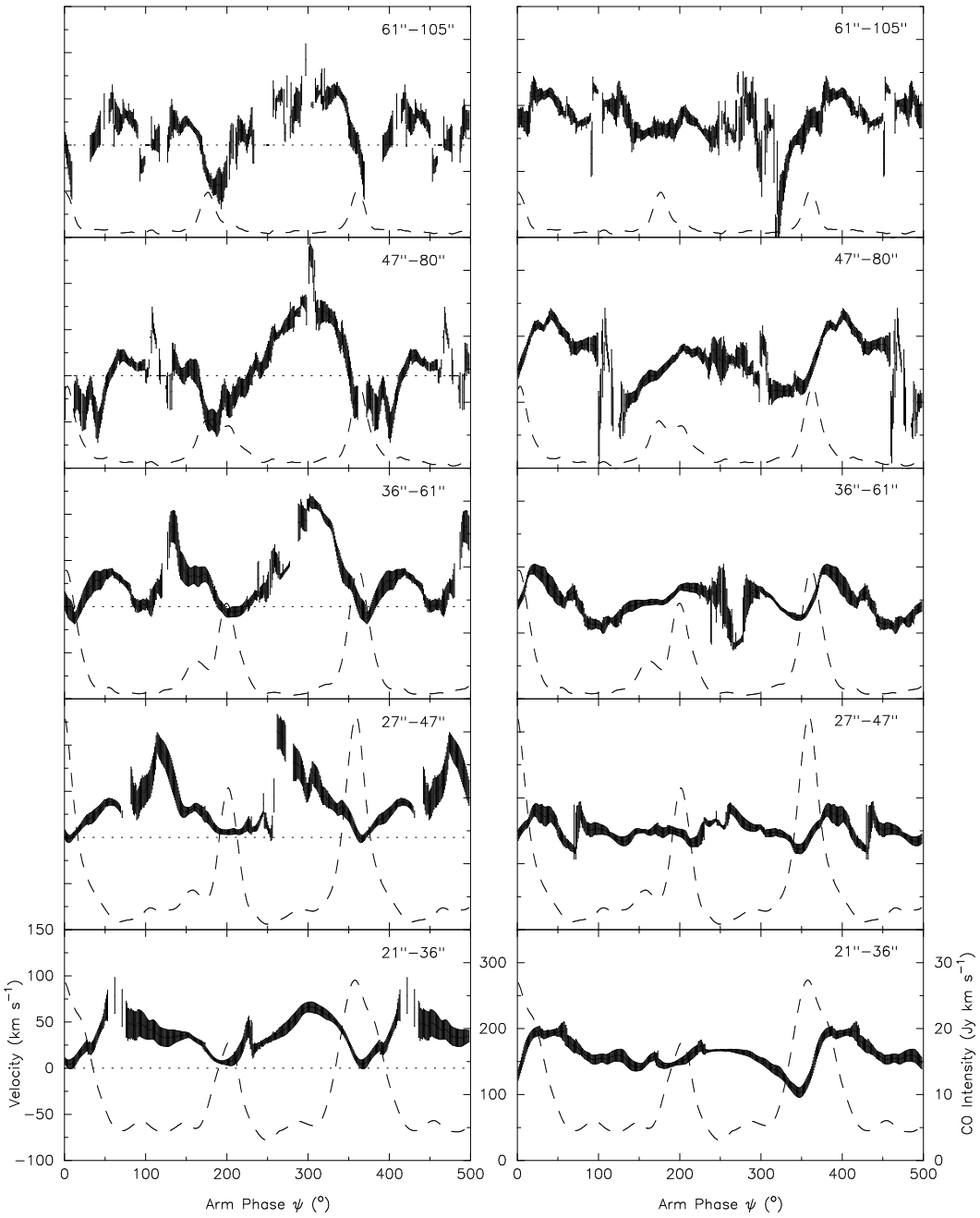

Figure 2.14: CO v_R (left panels) and v_θ (right panels) fits as a function of arm phase ψ in different annuli (with radii labeled in the upper right of each panel). The thickness of the line shows a range of $\pm 3\sigma$. Only v_R and v_θ fits with $3\sigma \leq 20$ km s^{-1} and ≤ 60 km s^{-1}, respectively, are shown. Dashed lines are the corresponding mean CO intensities, with the scale shown on the right ordinate. We assume a position angle of 170°, an inclination of 24° and the center position and systematic velocity listed in Table 2.1. Figure 2.16 shows the annular regions of M51 considered for these fits.

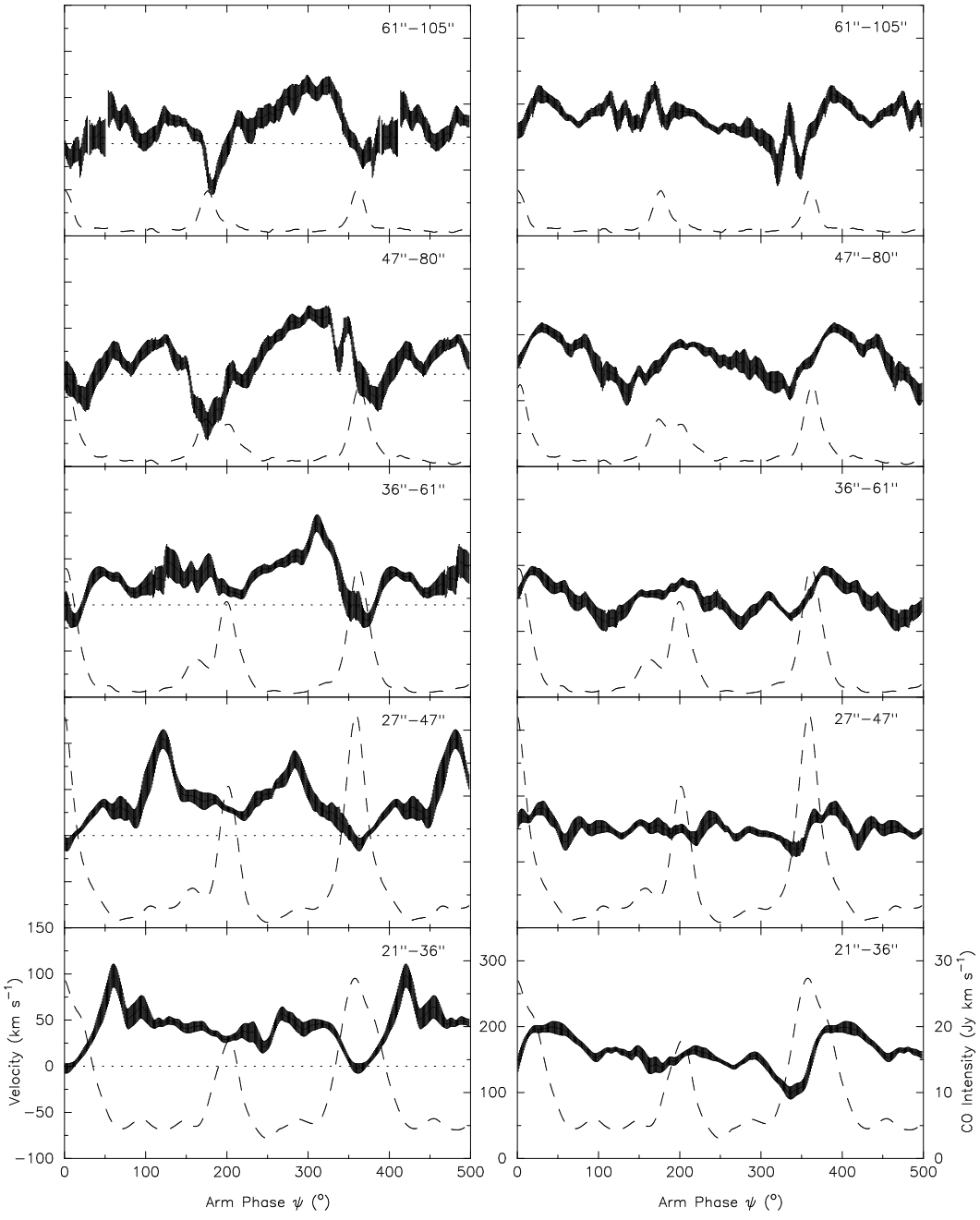

Figure 2.15: Hα v_R and v_θ fits as a function of ψ in different annuli, as in Figure 2.14.

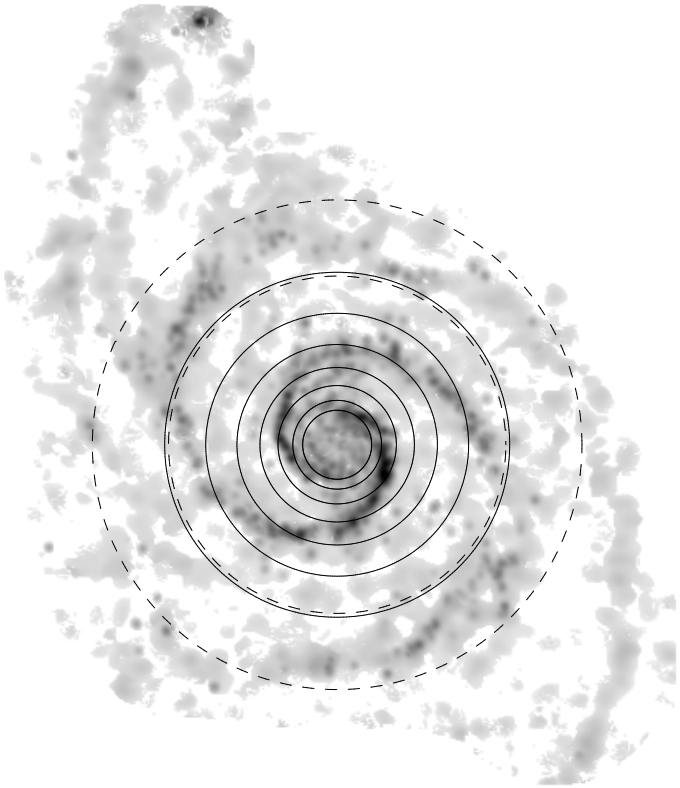

Figure 2.16: Deprojected CO map of M51 showing the overlapping annuli for which v_R and v_θ are fitted as a function of arm phase (shown in Figures 2.14 and 2.15). The radii of (solid) circles, from the inner to the outer, are: 21″, 27″, 36″, 47″, 61″, 80″, and 105″. The annulus marked by dashed circles (4.2 kpc $\leq R \leq$ 6.1 kpc) spans possible corotation radii corresponding to an adopted spiral pattern speed $\Omega_p = 38 \pm 7$ km s^{-1} kpc^{-1} (see §2.6.2).

An initial inspection of the streaming profiles indicates that the velocity structure is rather complex. Models of density wave streaming qualitatively predict that as gas encounters the arm, v_R, which was positive (i.e. outward) in the interarm, becomes negative, and that as the gas exits the arm it again becomes positive. The azimuthal velocity v_θ is predicted to increase rapidly as gas flows through the arm, and then decline more gradually in the interarm (e.g. Roberts & Stewart 1987, and §2.3). First we concentrate on Arm 1 (the brighter arm, shown at $\psi = 0^\circ$ and more fully at 360°). For v_R there is a pronounced minimum close to the arm position, seen in both CO and Hα. There is a boost in v_θ through the arm, again seen in both CO and Hα. For this arm, the streaming is

qualitatively as expected from steady-state spiral shock models. The velocities associated with Arm 2 (located at $\psi \sim 200^{\circ}$) however do not agree with simple predictions. For v_R, a clear minimum is only apparent in the outer annuli, and the boost in v_θ is weak or nonexistent. In the interarms, the structure appears somewhat more complex than the simple model expectation of a relatively constant or slowly rising v_R and a slowly declining v_θ. We suggest that Arm 1 matches simple theory because its structure is simple, i.e. well described as a log spiral of constant phase. By contrast, for Arm 2 the CO distribution is not as well described by a single log spiral segment. Instead, it has several segments with different pitch angles and jumps in phase; thus the velocities associated with this arm are complex.

One explanation for the differences in the two arms, as discussed by Rix & Rieke (1993), is that the spiral pattern in M51 is actually a superposition of a strong spiral mode with a m=2 Fourier component with weaker m=1 and m=3 components. Henry et al. (2003), using the spatial distribution of CO emission obtained from the BIMA CO map, found such a scenario to be feasible by explaining the bright arm as the result of constructive interference between the m=2 and m=3 components, and the weak arm the result of a destructive interference between the two components. There is evidence for interarm structure possibly supporting such a multiple density wave component description of the spiral arms, which would be expected to manifest itself in the kinematics. Recent *Spitzer* observations of M51 clearly show spiral structure between the main CO arms; the *Spitzer* image and interarm features are discussed in the next section.

There are also clear differences between different annuli. For example, in the $36''$ - $61''$ annuli, the v_R increase downstream from the weaker arm is much more pronounced than in the $21''$ - $36''$ annuli. In addition, there is a v_R decrease to as low as < -50 km s^{-1} in the arms of the outer regions, which perhaps can be attributed to an incorrect choice of a fixed position angle for the disk (see §2.4.3). There are also clear differences in the v_θ

gradients between different annuli.

By and large, similar velocity structure is apparent in both CO and Hα. For example, in the 47″ to 80″ annulus, the gradual rise in v_R from -50 km s^{-1} at ψ=180° to 70 km s^{-1} at ψ=300° is shown in both tracers. Further, there is a strong v_R peak at ψ=120° in the 27″ to 47″ annulus in both CO and Hα; however, such pronounced local extrema in the interarms are not expected in the theory for a single spiral mode. In general, the overall amplitude of the streaming and the location of most features coincide, and regions in which the velocity structure is somewhat different tend to be interarm regions where little CO is detected.

Such similarities are not unexpected due to the dynamical coupling between the different components. CO, which traces the molecular component, is dynamically cold, with a velocity dispersion of only 4 - 8 km s^{-1}. Thus, the molecular component of the disk reacts strongly to any perturbation, as evident in the strong v_R and v_θ gradients associated with the spiral arms. The spiral arms compress the gas, triggering star formation. The newly formed hot O and B stars subsequently ionize the surrounding gas, resulting in Hα emission. Due to the fact that much of the Hα emission comes from gas *near* the region of birth, observed Hα velocities will be similar to observed CO velocities. There may also be a diffuse ionized medium not closely associated with the O and B stars, and this medium is likely not dynamically coupled with the molecular gas. However, as can be seen in Figures 2.4 and 2.5, the brightest regions of Hα emission occur just downstream from the molecular spiral arms. Further, the generally good agreement between the velocity measurements from CO and Hα observations suggest that most of the ionized emission originates in gas associated with star forming regions. This similarity in velocity structure derived from independent observations also gives confidence that the fitted velocities are reliable and that the deviations from simple theory, including interarm features, are real.

The profiles in Figures 2.14 and 2.15 qualitatively agree with previous studies of

streaming in M51 involving 1D cuts along the major and minor axes (e.g. Aalto et al. 1999; Rand 1993). The gradients of the velocity profiles through the arms in different annuli is in accordance with the conclusion of Aalto et al. (1999) supporting the presence of shocks in the arms from a qualitative comparison of velocities along 1D cuts to streaming models of Roberts & Stewart (1987). In §2.6 we analyze the feasibility of a steady or quasi-steady spiral pattern in M51, which has been a working hypothesis for many analyses of the spiral arms of this galaxy.

2.5.1 Interarm Structure

In estimating the radial and tangential velocity components, we fit observed velocities along log-spiral segments. The slope of the slit is determined by the slope of the main CO arms on the logarithmic polar projection, i.e. the pitch angle of the arms. Though the slope of the CO arms, or at least the bright arm, is well defined, that slope may not be appropriate for the interarms. In other words, velocity may not be constant along the interarm log-spiral segments congruent to the main CO arms.

The recent *Spitzer* 8 μm image of M51 (Calzetti et al. 2005; Kennicutt et al. 2003), shows clear interarm features not seen in the CO map due to the lower resolution of the CO observations. Many of these features are spurs (or feathers) that have been found to be ubiquitous in grand design spirals (La Vigne et al. 2006). These interarm features will also cause kinematic perturbations. In fact, close inspection reveals that interarm perturbations in the velocity field of M51 coincide with strong interarm features apparent in the 8 μm image. Since the features have different pitch angles from the main CO arms, we are likely smearing out these finer interarm velocity perturbations. As a result, the interarm velocity profiles we have derived do not reveal the details of the velocity perturbations associated with interarm substructure; in a detailed study of the 2D velocity field between the main arms, the interarm structure would need to be considered.

In the next section, we use the v_R and v_θ fits to assess the feasibility of the hypothesis of a quasi-steady pattern. Again, our fitting method is designed to reveal streaming solely associated with the spiral arms, and does not capture smaller scale perturbations, such as those associated with interarm features. Both observations (Elmegreen 1980; La Vigne et al. 2006) and numerical simulations (Kim & Ostriker 2002; Shetty & Ostriker 2006) have shown that spurs and feathers are associated with star formation, indicating that these features are not long lasting. The modal theory, hypothesizing quasi-stationary grand design spiral structure, acknowledges that such smaller scale features can be transient (e.g. Bertin & Lin 1996). In this study, smearing out the interarm perturbations likely does not affect the overall conclusions we draw from the fitted velocity profiles.

2.6 Tests of Conservation Laws

2.6.1 Conservation of Vortensity

For a flattened system, the conservation of mass and angular momentum can be combined to yield

$$\frac{\partial}{\partial t}\left(\frac{\nabla \times \mathbf{v}_{inertial}}{\Sigma}\right) + \mathbf{v}_{inertial} \cdot \nabla \left(\frac{\nabla \times \mathbf{v}_{inertial}}{\Sigma}\right) = 0, \tag{2.11}$$

where Σ is the surface density, and $\mathbf{v}_{inertial}$ is the velocity in the inertial frame. Equation (2.11) states that the vorticity per unit surface density, known as vortensity, is conserved along streamlines. For steady systems, the conservation of vortensity can be simplified:

$$\frac{1}{\Sigma} \cdot \left(\frac{v_\theta}{R} + \frac{\partial v_\theta}{\partial R} - \frac{1}{R}\frac{\partial v_R}{\partial \theta}\right) = \text{constant along streamlines}, \tag{2.12}$$

because the temporal term in equation (2.11) vanishes. Even if the flow is not steady, portions of the galaxy that originated in a region of constant vortensity will maintain equal values of vortensity.

In order to test whether equation (2.12) is satisfied for the gas in M51, we need the surface density Σ, which we can estimate using the observed CO brightness to derive the corresponding H_2 column density.[2] Most studies suggest that the relationship between CO and H_2 is reasonably linear, although the conversion factor, known as the X-factor, is controversial. In our analysis, we will assume that CO is indeed a linear molecular tracer, and employ an X-factor of 2×10^{20} cm^{-2} [K km s^{-1}]$^{-1}$ (e.g. Strong et al. 1988).

We first test the vortensity condition from the velocity profiles derived in the 47″-80″ annulus, (see Figure 2.14 - 2.16). We choose this particular annulus because v_θ variations are relatively smooth in both arm and interarm regions, and are likely due primarily to spiral streaming. This annulus clearly shows the characteristic v_θ boost in the arm, and the more gradual interarm decrease in v_θ. We consider the fits derived from this annulus assuming a θ_{MA} = 170°(see Fig. 2.13). As shown in §2.4.3, changes in θ_{MA} affect v_θ only modestly.

For the first term in equation (2.12), v_θ/R, we use the mean value of the tangential velocities fit in the given region. To measure the radial gradient of the tangential velocity, which appears in the second term, we use

$$\left.\frac{\partial}{\partial R}\right|_\theta = \frac{1}{R \tan i_p} \frac{d}{d\psi}, \tag{2.13}$$

where i_p is the pitch angle of the spiral arms, and we assume negligible variation parallel to the arm. We adopt a pitch angle of 21.1° (which is also the slope of the "slit"). We fit straight lines to the velocity profiles in order to approximate the last two terms in equation (2.12). For the surface densities, we use the peak value for the arm, and for the interarm we use the value of Σ at phase separated by 90° from the arm. Again, we are assuming that CO directly traces the molecular abundance. Table 2.3 shows the vortensity values for the 47″-80″ annulus, including the values of each of the terms in equation (2.12).

[2]As we will describe in §2.6.2, H I can be neglected since the gas in M51 is mostly molecular in the region studied.

Table 2.3. Vortensity in the 47″ - 80″ Annulus

Region	$\overline{\Sigma}$[a]	$\left(\frac{v_\theta}{R}\right)$[b]	$\left(\frac{\partial v_\theta}{\partial R}\right)$[b]	$\left(\frac{1}{R}\frac{\partial v_R}{\partial \theta}\right)$[b]	Vortensity Value[c]
Arm 1 ($\psi \approx 360°$)	244	70 ± 1	103 ± 2	-30 ± 3	0.8 ± 0.2
Interarm 1 ($\psi \approx 90°$)	16	67 ± 1	-52 ± 3	6 ± 1	0.5 ± 0.2
Arm 2 ($\psi \approx 190°$)	128	63 ± 0.5	59 ± 3	-18 ± 3	1 ± 0.2
Interarm 2 ($\psi \approx 275°$)	19	59 ± 1	-31 ± 2	11 ± 1	0.9 ± 0.2

[a] $\left[M_\odot\ pc^{-2}\right]$; error of $\sim$20%

[b] $\left[km\ s^{-1}\ kpc^{-1}\right]$

[c] $\left[km\ s^{-1}\ kpc^{-1}\ (M_\odot\ pc^{-2})^{-1}\right]$

Table 2.3 shows that, within the errors, the arms and Interarm 2 have consistent vortensity values. The value for Interarm 1, however, is lower than in the other regions. The lower value for Interarm 1 can be inferred directly from the profile itself (Fig. 2.15). The tangential velocities in both arms are clearly rising, and v_θ in Interarm 2 (downstream from Arm 2 at $\psi = 200°$) is predominantly decreasing, suggesting that the spiral arms have the most significant influence on the velocities in these regions. In Interarm 1 (downstream from Arm 1 at $\psi = 0°$), however, there is more structure to the velocities, suggesting that there are other sources of perturbations in addition to the spiral arms. We find that for most of the velocity profiles in Figure 2.14 and 2.15 the vortensity values are consistent between the two arms, within the errors. However, in the interarms, the vortensity values differ. We find varying vortensity values in all interarm regions except for Interarm 2 indicated in Table 2.3. Overall, the agreement between vortensity in arm regions in each annulus indicates either that a steady state depiction of the vortensity is valid and there is very little radial migration of gas, or else that in a given annulus much of the gas originated in a region of constant vortensity and has been conserved along streamlines as gas in a whole annulus flows inward or outward.

2.6.2 Conservation of Mass

Flux Weighted Average v_R

In the QSSS scenario, the spiral pattern — as defined by its amplitude, phase, and rotation rate — would not change significantly over the course of a few revolutions in a frame rotating along with the spiral pattern (Bertin & Lin 1996; Lindblad 1963). Such a framework suggests that on average any accretion of material into the arms should be balanced by the same amount of material exiting downstream. This condition corresponds to conservation of mass for a steady state system; if this condition holds it should be apparent in the variation of observed velocities with spiral arm phase.

As can be seen in Figures 2.14 and 2.15, the spiral arms clearly perturb v_θ with deviations of ≥ 100 km s^{-1} but v_θ always remains positive, indicating that the orbital flow is in one direction only. However, the radial velocities do change sign, indicating both inflow and outflow. If the spiral arms are indeed a quasi-stationary pattern, then large amounts of matter should not be undergoing net inflow or outflow; i.e. the mass-weighted average radial velocity cannot be too large. A large or spatially strongly variable mass-weighted average v_R would imply a very dynamic system. In particular, if the sign of this quantity changes, then there would be a buildup or depletion of mass in one or more radial locations.

As discussed in §2.4.3, the fit for v_R is very sensitive to the assumed value of the position angle. Thus, in investigating the mass-weighted average radial velocity, we consider a range of position angles. Figure 2.17 shows the v_R fits for Hα in annuli with radii of $47''$ - $80''$ and $61''$ - $105''$ for three different position angles, 170°, 175°, and 180°. The CO fits are similar, but noisier and have larger error bars (see Figs. 2.14 - 2.15). A striking aspect of the fits in Figure 2.17 is the large magnitude of inflow in the arms for all three position angles; the radial velocity drops to as low as -75 km s^{-1}, suggesting significant inflow

for gas in the spiral arms. In the upstream regions v_R is positive, approaching 70 km s^{-1} for some parameter choices. For a region farther in, in the 27″ - 47″ annulus shown in Figures 2.14 and 2.15, the fitted radial velocity (assuming θ_{MA} = 170°) reaches values greater than 100 km s^{-1}, indicating tremendous outflow in the inner regions; assuming a position angle of 180° for this annulus only reduces the peak velocity from ≈100 km s^{-1} to ≈75 km s^{-1}.

Figure 2.18 shows the flux-weighted average radial velocity, $\langle v_R \rangle$, for different position angles in the different annuli used in the fitting process. With the canonical position angle of 170°, there is significant outflow in the inner regions of M51. On the other hand, a position angle of 180° seems appropriate for the innermost regions of M51, since this yields a lower value of $\langle v_R \rangle$. However, with such a position angle we find significant inflow in the outer region. If we adopt an intermediate position angle of 175°, there is outflow in the inner regions and inflow in the outer regions. For a θ_{MA} of 175°, $\langle v_R \rangle$ = 0 for the 36″ - 61″ annulus, with mean radius $\langle R \rangle$ = 1.98 kpc, while adjacent annuli have $\langle v_R \rangle$ = 10 and −20 km s^{-1}, for $\langle R \rangle$ = 1.5 kpc and 2.6 kpc respectively (1″ = 40.7 pc at a distance of 8.4 Mpc). If this were true, then the gas would all collect near $R \approx 2$ kpc in less than one orbital time-scale (∼200 Myr), which is not consistent with a steady state.

This analysis leads us to conclude that if the spiral pattern is long-lived, the large variations in the radial velocity shown in Figure 2.18 suggests that the position angle must vary with radius, indicating a disk that is not coplanar. This trend suggesting a larger position angle in the inner regions and a smaller position angle in the outer regions is also in accordance with the position angle tests described in §2.4.3 (see Figure 2.13).

We schematically show a disk with a varying position in Figure 2.19; the position angles of the ellipses are arranged as indicated by Figure 2.13. As discussed, one effect of a variation of position angle is a disk that is not coplanar. The inclination in this schematic is exaggerated; the observed morphology, including the apparent spiral structure, depends

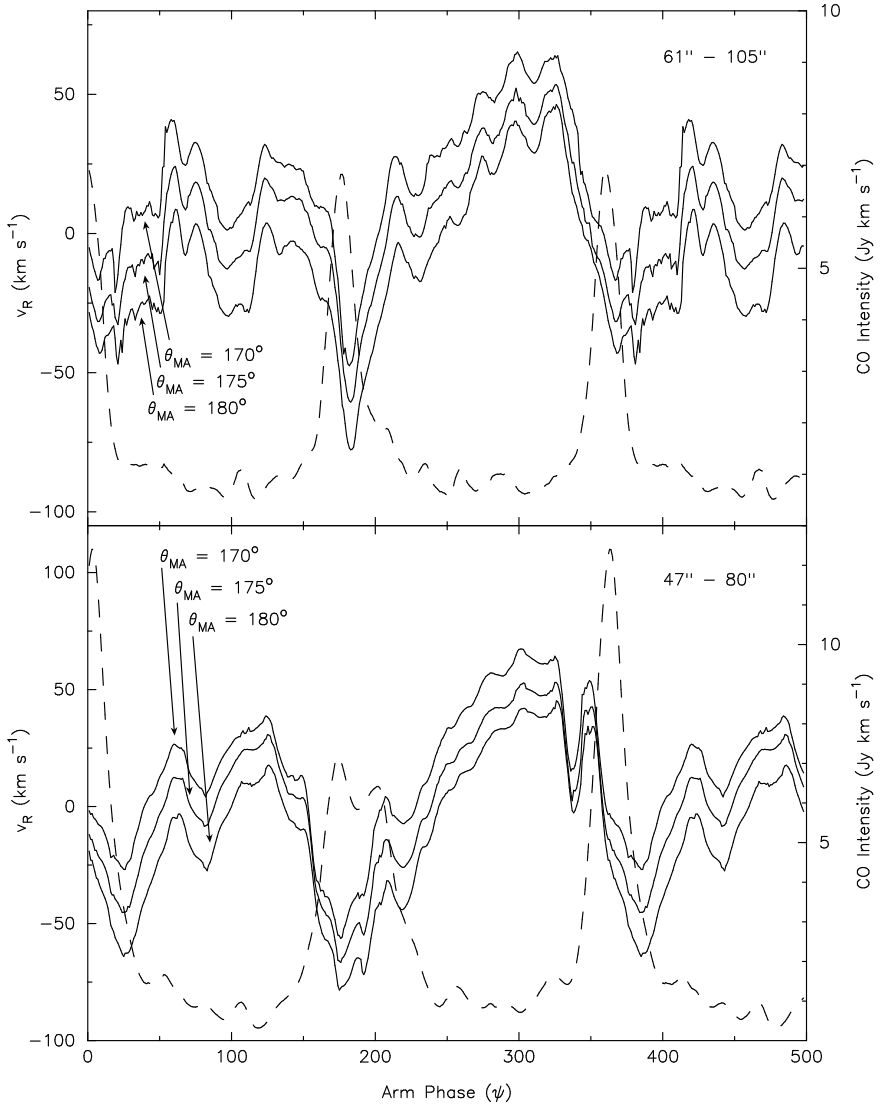

Figure 2.17: Hα v_R fits as a function of arm phase for 3 different position angles θ_{MA}, 170°, 175°, and 180°, for two annuli (47″ - 80 ″ and 61″ - 105″). We fix the inclination at 24°, and other parameters used in the fitting are shown in Table 2.1. The dashed line is the mean CO intensity along the arm for a θ_{MA} of 170°, which varies only slightly with θ_{MA}. The error bars are not shown because they are similar to those shown in Figure 2.15.

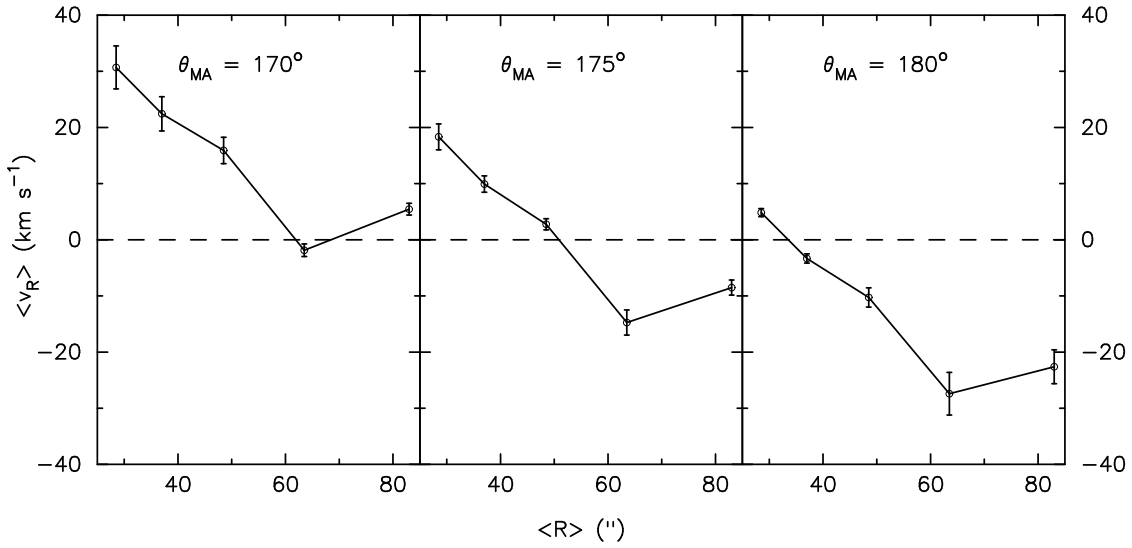

Figure 2.18: Mass-weighted average radial velocities $\langle v_R \rangle$ in the different annuli, two of which are shown in Figure 2.17. The abscissa indicates the mean radius $\langle R \rangle$, in arcsecs, of each annulus. The three panels show the mass-weighted average v_R assuming three different values for the position angle θ_{MA}. The error bars include both fitted errors in v_R (see Fig. 2.14) and an estimated error of 20% in Σ.

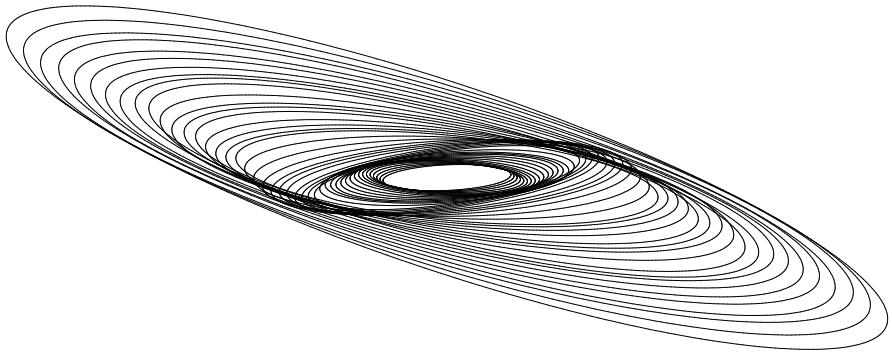

Figure 2.19: Model disk showing the variation of the position angle with radius. The position angle profile is taken from Fig. 2.13. The inclination is exaggerated to show a more edge-on view.

on the viewing angle, among other factors.

Continuity and Spiral Pattern Speed

In this section we explore the plausibility of QSSS using the gas continuity equation. The continuity equation for gas flow in a two-dimensional system is

$$\frac{\partial \Sigma}{\partial t} + \nabla \cdot (\Sigma \mathbf{v}) = 0; \tag{2.14}$$

this holds in any frame, e.g. whether the velocity is measured in an inertial frame or one rotating at a constant pattern speed. The first term, $\partial\Sigma/\partial t$, represents the temporal growth or decay of the surface density Σ at any given radius R and azimuthal angle θ in the plane of the galaxy, where those coordinates are with respect to the frame in which the velocity is being measured.

If the flow is in a steady state, then the temporal term vanishes, leaving only the mass flux term $\Sigma\mathbf{v}$. If the gas is responding primarily to a single dominant spiral perturbation, as would be required for a fixed spiral pattern, and when $\mathbf{v}$ is measured in the frame rotating at the pattern angular velocity Ω_p,

$$\nabla \cdot [\Sigma(\mathbf{v}_{inertial} - \Omega_p R\hat{\theta})] = 0. \tag{2.15}$$

Thus, for an exact steady state the mass flux into a region is equal to the mass flux out of the region (in the frame rotating with the same angular velocity as the spiral mode). For a quasi-steady state, the temporal variations in Σ will only be small, and thus variations in mass flux would also be small. This condition can be further simplified using a reference frame aligned locally with the spiral arms. Figure 2.20 shows this reference frame; the x and y coordinates are the directions perpendicular and parallel to the local spiral arm, respectively. The transformation between cylindrical coordinates and this arm frame is achieved using

$$\hat{x} = \cos i_p \hat{R} + \sin i_p \hat{\theta}, \tag{2.16}$$

$$\hat{y} = -\sin i_p \hat{R} + \cos i_p \hat{\theta}, \tag{2.17}$$

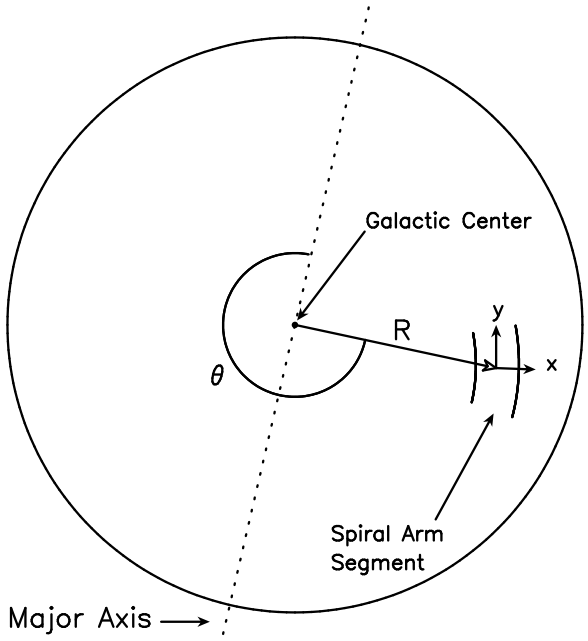

Figure 2.20: Coordinate transformation geometry, from (R,θ) galactocentric coordinates to the (x,y) spiral arm frame.

where i_p is the pitch angle of the arms.

The velocities in the arm frame are given by

$$v_x = v_R \cos i_p + (v_\theta - \Omega_p R) \sin i_p, \tag{2.18}$$

and

$$v_y = -v_R \sin i_p + (v_\theta - \Omega_p R) \cos i_p. \tag{2.19}$$

From the maps shown in Figures 2.1 and 2.4, it is apparent that the intensity and velocity vary significantly more across the arms, in the x-direction, than along them, in the y-direction. Thus, the variation in the product of Σv_y along $\hat{y}$ is much smaller than the variation in the product of Σv_x along $\hat{x}$, reducing equation (2.15) to

$$\Sigma v_x \approx \text{constant along } \hat{x}. \tag{2.20}$$

Namely, for a steady pattern, as the gas decelerates (in the x direction, perpendicular to the arm), mass accumulates and the surface density increases; as the gas velocity increases, the surface density decreases.

One difficulty in testing whether equation (2.20) holds is that neither θ_{MA} nor Ω_p is well constrained. Errors in θ_{MA} yield errors in the fitted value of v_θ of $\approx v_R \sin\Delta\theta_{MA}$ and in the fitted value of v_R of $\approx -v_\theta \sin\Delta\theta_{MA}$. If $\Delta\Omega_p$ is the error in the pattern speed, then the fitted value of v_x will be approximately given by $v_x + (-v_\theta \sin\Delta\theta_{MA}\cos i_p + v_R \sin\Delta\theta_{MA}\sin i_p - \Delta\Omega_p R \sin i_p)$. Since the v_R term has two factors of the sin of small angles, that term will be much smaller compared with the other two terms. The true value of v_x will therefore differ from the fitted value by $C_x \approx v_\theta \sin\Delta\theta_{MA}\cos i_p + \Delta\Omega_p R \sin i_p$.

In order to assess whether steady state continuity as expressed by equation (2.20) holds in the case of M51, we therefore consider the quantity

$$\Sigma\tilde{v}_x = \Sigma(v_R \cos i_p + (v_\theta - \Omega_p R)\sin i_p + C), \tag{2.21}$$

where v_R and v_θ are fitted values and $C \equiv \langle C_x \rangle$, i.e. the (unknown) azimuthally-averaged correction due to the errors in θ_{MA} and Ω_p. We apply equation (2.21) by solving for the value of C using the values of v_R, v_θ, and Σ in the two arm segments of an annulus:

$$C = \frac{[v_{R,arm1}\cos i_p + (v_{\theta,arm1} - \Omega_p R)\sin i_p]\Sigma_{arm1} - [v_{R,arm2}\cos i_p + (v_{\theta,arm2} - \Omega_p R)\sin i_p]\Sigma_{arm2}}{\Sigma_{arm2} - \Sigma_{arm1}}. \tag{2.22}$$

We then test whether the value of C obtained using equation (2.22) also satisfies equation (2.21) in the interarm regions. If equation (2.21) is satisfied for both interarm and arm regions, it would suggest an approximate steady state.

We again focus on the $47''$-$80''$ annulus, where the v_R (and v_θ) are relatively "smooth." The v_R profiles for this annulus is shown in Figure 2.17, assuming three different values of the position angle. Table 2.4 shows the relevant values associated with equation (2.21) for the arms and interarm regions. We employ the pattern speed of 38 ± 7 km s^{-1} kpc^{-1}, calculated by Zimmer et al. (2004) by applying the Tremaine-Weinburg method CO observations of M51. Corotation corresponding to this pattern speed is marked on Figure 2.16. After solving for C using quantities from the arms, it is clear that the flow

in the interarm region is not consistent with a steady state description. A position angle of 170° produces large negative mass flux in the arms, and positive flux in one interarm region. Even variations in the X-factor cannot resolve this discrepancy. Assuming larger values of the position angle still produces mass fluxes with vastly different magnitudes, and even different signs. Increasing the error in C up to an order of magnitude still cannot result in consistent mass fluxes between the arm and interarm. This suggests that any reasonable changes to the values of θ_{MA} or Ω_p will still result in varying mass fluxes. We have checked the mass flux in other annuli using the same method as for the 47″-80″ annulus, as well as in other localized regions not presented here, and found similar discrepancies in the mass flux.

In our analysis of continuity so far, we have not taken into account the contribution from the atomic component of the disk. In fact, in most galaxies the majority of the gas exists in the form of H I. In M51, Tilanus & Allen (1989) showed that the downstream offset of H I relative to the dust lanes is likely due to dissociation of molecular gas by recently formed massive stars. However, the inner disk of M51 has an unusually large fraction of molecular gas, so even at peaks of the H I photodissociation arms, the contribution of atomic gas to the total gas surface density is negligible. Using the H I maps of Rots et al. (1990), we find that the atomic column density N(H I) is significantly less than the molecular column density $N(H_2)$ in the vast majority of locations in the inner disk ($21'' \leq R \leq 105''$); N(H I) exceeds $N(H_2)$ in only $\sim$ 7% of the inner disk. The mean value of $N(H_2)/N$(H I) throughout the inner region is $\sim$10. Though we used a constant X-factor to obtain the molecular surface density, moderate variations in the X-factor (for M51, see Nakai & Kuno 1995) will not be sufficient to account for the discrepancy. Nevertheless, no change in the X-factor, or in the contributions of the molecular or atomic matter to the total mass, can account for the change in sign of the mass flux; the varying sign of Σv_x can only be due to a sign change in v_x, not Σ.

Table 2.4. Mass Flux in the 47″ - 80″ Annulus

Region	Σ[a]	$v_R \cos i_p$[b]	$(v_\theta - \Omega_p R)\sin i_p$[b]	C[c]	$\Sigma\tilde{v}_x$[d]
$\theta_{MA} = 170°$:					
Arm 1 ($\psi \approx 360°$)	244	-24	41	-58 $\pm$ 30	-10113
Arm 2 ($\psi \approx 190°$)	128	-53	32	-58 $\pm$ 30	-10113
Interarm 1 ($\psi \approx 90°$)	16	23	18	-	-259
Interarm 2 ($\psi \approx 275°$)	19	49	21	-	237
$\theta_{MA} = 175°$:					
Arm 1 ($\psi \approx 360°$)	244	-41	41	-32 $\pm$ 18	-8103
Arm 2 ($\psi \approx 190°$)	128	-63	32	-32 $\pm$ 18	-8103
Interarm 1 ($\psi \approx 90°$)	16	12	18	-	-38
Interarm 2 ($\psi \approx 275°$)	19	36	21	-	464
$\theta_{MA} = 180°$:					
Arm 1 ($\psi \approx 360°$)	244	-59	41	-8 $\pm$ 17	-6345
Arm 2 ($\psi \approx 190°$)	128	-71	32	-8 $\pm$ 17	-6345
Interarm 1 ($\psi \approx 90°$)	16	1	18	-	182
Interarm 2 ($\psi \approx 275°$)	19	27	21	-	761

[a] $\left[\mathrm{M}_\odot\ \mathrm{pc}^{-2}\right]$; error of $\sim$20%

[b] $\left[\mathrm{km\ s}^{-1}\right]$

[c] $\left[\mathrm{km\ s}^{-1}\right]$; error largely due to errors in Σ and Ω_p

[d] $\left[\mathrm{M}_\odot\ \mathrm{pc}^{-2}\ \mathrm{km\ s}^{-1}\right]$

Our conclusion, after analyzing the mass flux, is that the kinematics are not consistent with a quasi-steady spiral pattern in a flat disk. We find that no single pattern speed can satisfy quasi-steady state continuity, suggesting that the QSSS hypothesis is not applicable to M51. It is essentially the tremendous variations of the radial velocity within a given annulus — amounting to ~ 100 km s^{-1} — that lead the QSSS hypothesis into difficulty. One explanation for the transient nature of the spiral arms in M51, perhaps due to the interaction with its companion, is a spiral perturbation with a constant pattern speed, but with time-varying amplitude. Or, there may be multiple modes at work in the disk of M51, which may be construed as a mode with a radially varying pattern speed (e.g.

Merrifield et al. 2006). Multiple patterns speeds in M51 have been previously suggested by Vogel et al. (1993) and Elmegreen et al. (1989). However, the extreme variations in the radial velocity cannot be explained by multiple patterns alone. Possible causes for the large observed v_R gradients are large out-of-plane motions or a variation in inclination; since the inclination of M51 is small, a variation in i due to a warped or twisted disk will produce large variations in the observed velocity due to projection effects.

2.6.3 Discussion

We have shown that the density and velocity structure in M51 does not support a quasi-steady state depiction for the spiral pattern, using measurements of the mass flux. Further evidence that the observed structure is inconsistent with steady state can be obtained by adopting the fitted 2D velocity field, and demonstrating that the density structure is then non-steady. We have carried out this exercise using a modified version of the `NEMO` task `FLOWCODE` (Teuben 1995). In this exercise, a disk is populated with gas tracer particles using the intensity profiles averaged along spiral segments, reproducing the spiral density pattern of M51. Each location in the disk has an associated v_R and v_θ, given by the fitted velocity profiles (e.g. Figures 2.14 and 2.15), and an assumed value of the pattern speed. The motion of the particles is then integrated using `FLOWCODE`: after a suitably small time step, the particles take on new velocities depending on their location in the disk. In essence, this simulation is a purely kinematic test to determine whether the steady state continuity equation (eqn. [2.15]) is satisfied or not, using the density and fitted velocity profiles of M51 (Figs. 2.14-2.15). We find that the input spiral pattern vanishes in less than one orbital timescale ($\sim$200 Myr), regardless of what values of the position angle and pattern speed we assume.

The precise nature of the velocities is one of a number of issues that need to be considered in further studying the the global spiral pattern in M51. For example, our result

suggests the role of a warp certainly needs to be taken into account. There are strong indications that the outer disk of M51 is warped; our finding suggests that the disk is not coplanar even further inward. The non-coplanar attribute may be the result of the tidal interaction between M51 and its companion.

The possible warp and/or twist in the disk of M51 would of course affect the projected velocities, and would present itself as gradients in the velocity components, as discussed in the previous section. If this were indeed the case, then the single or multiple in-plane modes would have to be in phase with the vertical mode in order to sustain a spiral pattern. The inherent uncertainty in deriving three velocity components from the single observed component leads to difficulty in estimating and analyzing both the vertical and in-plane modes.

2.7 Summary

We have analyzed the velocity field of M51, using CO and Hα observations, to investigate the nature of the spiral structure. We summarize the main results here:

1) The velocity field is quite complex. Observed velocities show significant azimuthal streaming associated with the spiral arms, as well as strong gradients in the radial velocities.

2) The aberrations in the velocity field strongly suggest that the disk is not coplanar, perhaps as far in as $20''$ ($\sim$800 pc) from the center.

3) We obtain fitted radial and tangential velocity profiles by assuming that velocities in any annulus vary only with arm phase. Strong gradients in the radial and tangential velocities are found in the profile fits. In general, the shape of both the v_R and v_θ profiles are in qualitative agreement with theory of nonlinear density waves, and support the presence of shocks.

4) In detail, the velocity profiles from different radial regions of M51 differ significantly. In addition, velocity profiles associated with the two arms also show differences in a given annulus. For the arm that is well described by a logarithmic spiral (bright arm), the associated velocities are in good agreement with simple theoretical spiral shock profiles. For the other arm, which is not as well described by a logarithmic spiral, the velocities are more complex.

5) The velocity profile fits from CO and Hα emission are rather similar, suggesting that most of the Hα emission originates from gas associated with star forming regions.

6) When we assume a single value for the position angle of the major axis of M51 and inclination, we find that large amounts of material flows toward an annulus of intermediate radius, due to the large gradients and change of sign in the flux weighted average radial velocity. As a result, either the position angle of the major axis or the inclination must vary with radius, suggesting that the disk of M51 is warped and twisted.

7) We analyze conservation of vortensity, using the radial and tangential velocity profile fits. We find that vortensity is fairly consistent within a given annulus, indicating that the gas there all originated in a region of uniform vortensity.

8) Using the equation of continuity, we find that the density and fitted velocity profiles are inconsistent with quasi-steady state mass conservation in any frame rotating at a constant angular speed, at least for a planar system. Variations in the pattern speed, position angle, and X-factor alone cannot account for the differences in the mass flux, suggesting that spiral arms are quite dynamic, and possibly that out-of-plane motions are significant.

Acknowledgments

We are grateful to S. McGaugh for his help in using the baryonic Tully-Fisher relation to estimate the inclination of M51. We thank W. T. Kim for useful discussions, and G. Gomez for providing velocity profiles from his hydrodynamic models. We also thank the anonymous referee for raising many interesting questions and useful suggestions. This research was supported in part by grants AST 02-28974 and AST 05-07315 from the National Science Foundation.

Chapter 3

Global Modeling of Spur Formation in Spiral Galaxies

Abstract

We investigate the formation of substructure in spiral galaxies using global MHD simulations, including gas self-gravity. Local modeling by Kim & Ostriker (2002) previously showed that self-gravity and magnetic fields cause rapid growth of overdensities in spiral arms; differential compression of gas flowing through the arms then results in formation of sheared structures in the interarms. These sheared structures resemble features described as spurs or feathers in optical and IR observations of many spiral galaxies. Global modeling extends previous local models by including the full effects of curvilinear coordinates, a realistic log-spiral perturbation, self-gravitational contribution from five radial wavelengths of the spiral shock, and variation of density and epicyclic frequency with radius. We show that with realistic Toomre Q values, self-gravity and galactic differential rotation produce filamentary gaseous structures with kpc-scale separations, regardless of the strength – or even presence – of a stellar spiral potential. However, a sufficiently strong spiral potential is required to produce "true spurs", consisting of interarm struc-

tures emerging from gas concentrations in the main spiral arms. In models where Q is initially constant, filaments due to interarm self-gravity grow mainly in the outer regions, whereas true arm spurs grow only in the inner regions. For models with $Q \propto R$, outer regions are intrinsically more stable so "background" interarm filaments do not grow, but arm spurs can develop if the spiral potential is strong. Unlike independently-growing "background" filaments, the orientation of arm spurs depends on galactic location. Inside corotation, spurs emanate outward, on the convex side of the arm; outside corotation, spurs grow inward, on the concave side of the arm. Based on orientation and the relation to arm clumps, it is possible to distinguish "true spurs" that originate as instabilities in the arms from independently growing "background" filaments. We measure spur spacings of $\sim$3 - 5 times the Jeans length in the arm, and arm clump masses of $\approx 10^7$ $M_\odot$. Finally, we have also studied models without self-gravity, finding that magnetic fields suppress a purely hydrodynamic instability recently proposed by Wada & Koda (2004) as a means of growing interarm spurs and feathers. Our models also suggest that magnetic fields are important in preserving grand design spiral structure when gas in the arms fragments via self-gravity into GMCs.

3.1 Introduction

Observations of disk galaxies reveal that arm substructures are prevalent in grand design spirals. Some of the most prominent secondary features are spurs and feathers, which are structures that emanate from the primary spiral arm and are usually seen to sweep back to trail the flow in the interarm region. Historically, in the observational literature the term "spur" has denoted stellar features seen in optical emission (Elmegreen 1980), whereas the term "feathering" has been used to denote a series of extinction features that overlies the bright portion of a stellar spiral arm (Lynds 1970). Elmegreen (1980) concluded that

spurs are long-lived features, based on observations in multiple bands, including the I band, which generally traces the older stellar component. Recent high-resolution observations, such as the Hubble Heritage image of M51 (Scoville & Rector 2001) and several galaxies in the *Spitzer* SINGS sample (Kennicutt et al. 2003), have revealed examples of these features in extraordinary detail. An archival study of *Hubble Space Telescope* (*HST*) images has established that spurs and feathers are in fact ubiquitous in galaxies with well-defined spiral arms and that single continuous structures evidence evolution from primarily gaseous to primarily stellar composition (La Vigne et al. 2006). Taken together, these observations indicate that feathers and spurs are an essential aspect of spiral structure that should be accounted for by theoretical modeling of disk galaxies.

Many studies of spiral structure, both theoretical and observational, have applied the hypothesis of a quasi stationary spiral structure (QSSS) (Lin & Shu 1964). Under the QSSS framework, the general shape of the spiral pattern is assumed to remain steady for many galactic revolutions. The stellar spiral arms themselves arise as self-consistent density waves (or modes). Roberts (1969) demonstrated that shocks can develop in the gaseous component as it responds to an "external" spiral potential arising from the stellar disk, and predicted values of the gas velocity both upstream and downstream from the shocks. Such velocity profiles have been observed for many galaxies, such as M51 (e.g. Aalto et al. 1999; Rand 1993; Shetty et al. 2007), and M100 (e.g. Rand 1995). M81 has also been studied extensively in support of density wave theory (e.g. Lowe et al. 1994; Visser 1980b).

A number of theories consistent with the QSSS concept have been proposed to explain substructure in spiral galaxies. Shu et al. (1973) suggest that ultra-harmonic resonances between the motion of the primary spiral pattern and the background gas flow can be responsible for the secondary features in spiral galaxies. Chakrabarti et al. (2003) (hereafter CLS) performed hydrodynamic simulations of self-gravitating gaseous disks to study the

role of ultraharmonic resonances. They showed that the spiral arm bifurcates and that strong branches, which in observations are large scale dust lanes similar in angular extent to the main arms, occur near resonant radii (see also Artymowicz & Lubow (1992)).

The origin and nature of observed smaller-scale feathers and spurs, however, has not yet been firmly established. Balbus (1988) attributed these features to the growth of gravitational instabilities in the gas component in preferred directions. Kim & Ostriker (2002), hereafter KO, performed numerical simulations focused on a local patch of a gaseous spiral arm in a galactic disk, and showed that the growth of prominent, nonlinear spurs[1] can occur due to the mutual contributions of self-gravity and magnetic fields, via the so-called "magneto-Jeans Instability." Within the arm, the radial gradient in angular velocity is reversed, so that spurs in the models of KO are initially locally leading. Well into the interarm regions, background galactic shear causes the spurs to become trailing features. This characteristic shape is evident in the Hubble Heritage image of M51 (Scoville & Rector 2001). On the other hand, Wada & Koda (2004), hereafter WK, suggest that the growth of spurs results from purely hydrodynamic effects. In their two-dimensional models (excluding magnetic fields and self-gravity), the spiral shocks become unstable; this instability causes the growth of clumps and subsequently leading interarm features, which they refer to as spurs. They suggest the mechanism responsible for the growth of these spurs is the Kelvin-Helmholtz instability. Using smoothed particle hydrodynamics (SPH) simulations, Dobbs & Bonnell (2006) also investigate the non-self-gravitating case, and suggest that feather and spur formation requires gas temperatures < 1000K. Contemporary with the current work, Kim & Ostriker (2006) extended their 2D local self-gravitating models to 3D; that work also investigates the effects of vertical structure on hydrodynamic Kelvin-Helmholtz modes.

[1]We adopt the term "spur", following KO, to describe interarm gas features in hydrodynamic and MHD models.

Here we model isothermal gaseous disks under the influence of both magnetic and self-gravitational effects. We extend the local simulations of KO into the global regime, which allows us to study the growth of spurs using more realistic models. In particular, whereas in KO the unperturbed disk had uniform density, a linear shear profile, and did not treat curvature effects, the present models relax all of these idealizations. Our global models, which extend over more than an order of magnitude in radius, allow for arbitrary density profiles and rotation curves, and solve the full equations of magnetohydrodynamics (MHD) in cylindrical symmetry. To assess the effect of self-gravity, we first consider just a disk of rotating gas, varying initial conditions such as the magnetic field strength and Toomre stability parameter. We then apply an external spiral potential, which reorganizes the gas to form a spiral pattern. In models with and without a spiral potential, we follow the evolution of the gas far into the nonlinear domain as self-gravity takes hold and investigate the properties of the interarm features and clumps that arise.

This paper is organized as follows: In §3.2 we present the relevant equations of MHD and gravity, and describe the models, parameters, and numerical algorithms we use to simulate disk galaxies with spiral arms. In (§3.3), we consider models without including self-gravity, both with and without magnetic fields. Next, in §3.4, we present the models including self-gravity. We show how self-gravity causes the growth of condensations in the gas, and how this effect is crucial for the growth of interarm structures in disks with an external spiral potential. In §3.5 we analyze and discuss various aspects of our results. In §3.5.1, we explore the issue of distinguishing whether observed interarm structures are true arm spurs or independent background features with a superposed large-scale spiral structure; in §3.5.2 we quantify masses and spacings of clumps and spurs; and in §3.5.3 and §3.5.4 we discuss the issue of gas/star arm offsets and disk thickness, respectively. We conclude in §3.6 with a summary.

3.2 Modeling Methods

3.2.1 Basic Equations

Our simulations involve the gaseous response to an external spiral potential, including effects of self-gravity and magnetic fields, in a two-dimensional galactic disk model. The gas is initially in pure circular motion around the galactic center. We adopt a flat rotation curve, i.e. a constant azimuthal velocity v_c. A non-axisymmetric variation in the stellar component is responsible for an external spiral perturbation, and is modeled as a rigidly rotating potential with a pattern speed Ω_p. We investigate the formation and evolution of arms, spurs, clumps, and other features by integrating the MHD equations in a polar (R,ϕ) coordinate system.

The relevant equations of MHD and gas self-gravity are

$$\frac{\partial \Sigma}{\partial t} + \nabla \cdot (\Sigma \mathbf{v}) = 0, \tag{3.1}$$

$$\frac{\partial \mathbf{v}}{\partial t} + \mathbf{v} \cdot \nabla \mathbf{v} + \frac{1}{\Sigma} \nabla p = \frac{2H}{4\pi\Sigma} (\nabla \times \mathbf{B}) \times \mathbf{B} - \nabla(\Phi_{ext} + \Phi), \tag{3.2}$$

$$\frac{\partial \mathbf{B}}{\partial t} = \nabla \times (\mathbf{v} \times \mathbf{B}), \tag{3.3}$$

$$\nabla^2 \Phi = 4\pi G \delta(z) \Sigma. \tag{3.4}$$

where Σ is the gas surface density and $\mathbf{v}$, p, and $\mathbf{B}$ are the vertically averaged velocity, vertically integrated pressure, and vertically averaged magnetic field, respectively. The semi-thickness of the disk is H, such that $\Sigma/2H$ is the mid-plane density ρ_0. For our models, we assume an isothermal equation of state, so that $p = c_s^2 \Sigma$, where c_s is the sound speed. The terms Φ_{ext} and Φ, respectively, represent the external spiral potential and the gaseous self-gravitational potential. The external spiral potential Φ_{ext} is specified at time t, in the inertial frame, by

$$\Phi_{ext}(R,\phi;t) = \Phi_{ext,0} \cos[m\phi - \phi_0(R) - m\Omega_p t] \tag{3.5}$$

where m, $\phi_0(R)$, and Ω_p are the number of arms, reference phase angle, and spiral pattern speed, respectively. We assume the spiral arms have a constant pitch angle i, implying a logarithmic spiral, so that

$$\phi_0(R) = -\frac{m}{\tan i}\ln(R) + constant. \tag{3.6}$$

Since we simulate disks in an inertial frame of reference, explicit corrections to equation (3.2) for Coriolis and centrifugal forces are not required.

3.2.2 Model Parameters

For the simulations presented in this paper, we use a constant sound speed c_s, which we set to 7 km s^{-1} for scaling our solutions. We use a constant rotational velocity v_c, which is set to 210 km s^{-1}. Because our models are isothermal, in fact our results would hold for any model with the same ratio v_c/c_s = 30. The code length unit is L_0, which for convenient scaling of our solutions we set to 1 kpc. With c_s = 7 km s^{-1}, this implies a time unit for scaling of $t_0 = L_0/c_s = 1.4 \times 10^8$ years. This time corresponds to one orbit $t_{orb} = 2\pi/\Omega_0$ at a fiducial radius R_0 which is given by $R_0 = L_0 v_c/2\pi c_s$. With L_0 = 1 kpc, the value of R_0 is 4.77 kpc. Our results can be rescaled to other values of R_0 and L_0 with the same ratio.

We explore a range of values for the parameters required to specify the spiral perturbation. The amplitude of the potential perturbation $\Phi_{ext,0}$ in equation (3.5) is characterized by the ratio F of the maximum radial perturbation force to the radial force from the background axisymmetric potential (responsible for v_c), i.e.

$$F \equiv \frac{\Phi_{ext,0} m}{v_c^2 \tan i}. \tag{3.7}$$

We model spiral disks with external potential strengths F = 10%, 3%, and 1%. We apply the spiral perturbation gradually, increasing from zero and settling to the maximum level

F at time $t = t_{orb}$. Since it has proved to be difficult to locate corotation from observations, we also explore a range in Ω_p/Ω_0 = 0.19 to 0.96. For our fiducial values of L_0 and c_s, Ω_p ranges from $\sim$8 to 42 km s^{-1} kpc^{-1}, corresponding to corotation radii of 25 to 5 kpc for a circular velocity of 210 km s^{-1}. The pitch angle i in most of our simulations is 10°. We will show that changing the pitch angle does not strongly affect the formation and properties of substructures. For all our models, we have an m = 2 (two-armed) pattern.

The initial surface density Σ_0 at the fiducial radius R_0, along with the constant circular velocity v_c, determines the value of the Toomre stability parameter at R_0,

$$Q_0 \equiv \frac{\kappa_0 c_s}{\pi G \Sigma_0}, \tag{3.8}$$

where κ_0 is the initial epicyclic frequency; for a constant circular velocity, $\kappa_0 = \sqrt{2}\Omega_0 = \sqrt{2}v_c/R_0$. Thus, the initial background surface density at R_0 is

$$\Sigma_0 = \frac{32}{Q_0}\,\mathrm{M}_\odot\,\mathrm{pc}^{-2}\left(\frac{c_s}{7\,\mathrm{km\,s^{-1}}}\right)\left(\frac{\kappa_0}{62\,\mathrm{km\,s^{-1}\,kpc^{-1}}}\right). \tag{3.9}$$

As described below, we explore a couple of initial density distributions, including a $\Sigma \propto R^{-1}$ density distribution for which Q is initially constant for the whole disk.

We characterize the initial magnetic field strength by the ratio β of the midplane gas pressure to the midplane magnetic field pressure

$$\beta = \frac{P_{gas}}{P_B} = \frac{8\pi c_s^2 \Sigma}{2HB^2}. \tag{3.10}$$

The initial magnetic field lines $\mathbf{B} = B\hat{\phi}$ lie in the plane of the disk, and are directed in the $\hat{\phi}$ direction only. From equation (3.10) the value of the magnetic field (with c_s, β, and H constant) varies $\propto \Sigma^{1/2}$. Taking H = 100 pc and Q_0 = 2, the value of B at the fiducial radius is

$$B_0 = \left(\frac{4c_s^3\kappa_0}{Q_0 HG\beta}\right)^{1/2} = \frac{8.2}{\sqrt{\beta}}\,\mu G. \tag{3.11}$$

3.2.3 Numerical Methods

We follow the evolution of the gaseous disk by integrating equations (3.1) - (3.4) using a cylindrical polar version of the ZEUS code. ZEUS (Stone & Norman 1992a,b) is a time-explicit, operator-split, finite difference method for solving the equations of MHD on a staggered mesh. ZEUS employs "constrained transport" to ensure that $\nabla \cdot \mathbf{B} = 0$, and the "method of characteristics" for accurate propagation of Alfvénic disturbances. The hydrodynamic/MHD portion of our cylindrical-polar code has been verified using a standard suite of test problems. These include advection tests, shocks aligned and not aligned with the coordinates, a magnetized rotating wind (Stone & Norman 1992b), and a rotating equilibrium disk with both magnetic and pressure gradients.

The (R, ϕ) staggered mesh for our version of the code has a constant logarithmic increment in the radial dimension, i.e. $R_{i+1} = (1 + \delta)R_i$, for some $\delta > 0$. We consider only the perturbed gas density (by subtracting the initial density) in determining the self-gravitational potential at each time step. The contribution of the initial axisymmetric gas disk to the total potential is assumed to be included in the axisymmetric potential responsible for the constant circular velocity v_c. To compute the self-gravitational potential Φ, we use one of two methods described in the Appendix (§A.2). One method uses a combination of a Fourier transform in the azimuthal direction and a Green's function in the radial direction, while the other method uses Fourier transforms in both directions on an expanded, zero-padded grid. For both methods, we allow for a finite disk thickness using a softening parameter H. Except as noted, we adopt H = 100 pc. We give detailed descriptions of our methods, tests, and comparisons in the Appendix. Fast Fourier transforms are performed using the free software FFTW (Frigo & Johnson 2005).

The standard computational domain for our models has 512 radial and 1024 azimuthal zones, covering a radius range of 1 - 15 kpc, and an azimuthal range of 0 - π radians. With

this resolution, the Jeans length ($\lambda_J = c_s^2/G\Sigma$) from our initial surface density distributions are well resolved at all radii, satisfying the Truelove criterion (Truelove et al. 1997). The radial range allows ≈ 5 radial wavelengths of the spiral pattern. Given the extended range in the radial dimension, we implement outflow boundary conditions, since loss of gas at the boundary will not affect the majority of the disk. We also taper the spiral potential near the boundaries, which helps minimize loss of matter near the edges. In the azimuthal direction, we use periodic boundary conditions. Although the azimuthal range is only half of a complete disk, the gravitational potential includes the contribution from the other half which is not explicitly simulated (see Appendix).

3.3 Simulating Spiral Galaxies Without Gas Self-Gravity

We first investigate the flow of gas in a spiral potential without including the gaseous self-gravitational potential. These preliminary simulations will indicate whether, for a given parameter set and numerical resolution, long lasting spiral patterns can be sustained. We will also investigate the effect of magnetic fields on the resulting flow and spiral morphology. As these models are similar to the hydrodynamic simulations of WK, we are able to investigate the "wiggle instability" that they propose, and to assess how magnetic fields affect this process. Table 3.1 shows the relevant parameters used for each model. Column (1) lists each model. Column (2) lists β, which characterizes the magnetic field strength (see eq. [3.10]). The external potential strength F (from eq. [3.7]) is listed in column (3). Column (4) gives the pattern speed Ω_p (used in eq. [3.5]). The pitch angle i is listed in column (5). We note that although the computational domain only simulates half the disk, with periodic azimuthal boundary conditions, we replicate the simulated half in presenting snapshots of the models.

Table 3.1. Parameters for Models Without Gas Self-Gravity

Model (1)	β (2)	F (%) (3)	Ω_p (km s^{-1} kpc^{-1}) (4)	i (°) (5)
HD1	∞	3	8.4	10
HD2	∞	10	8.4	10
HD3	∞	10	42	10
HD4	∞	10	8.4	20
MHD1	1	10	8.4	10

3.3.1 Pure Hydrodynamic Models

We begin by considering simple cases where the rotating gas in a disk only responds to an external spiral potential, without including magnetic fields or gas self-gravity. Model HD1 has a weak (F = 3%) and slowly rotating external spiral potential, as well as a small pitch angle (10°). Figure 3.1 shows density snapshots of model HD1. At t/t_{orb} = 1, when the external potential reaches its maximum amplitude, the spiral arms are weak but distinct. Figures 3.1(b) and 3.1(c) shows that two orbits after the potential is fully applied, the spiral arms are still distinct and rather regular. At t/t_{orb} = 3 , in the inner regions, shown in Figure 3.1(d), the spiral arms are not as distinct as the rest of the galaxy. The main arms grow weaker, and leading spiral like features grow between the main (trailing) arms. Nevertheless, a global spiral pattern persists throughout the galaxy, indicating that a weak perturbing potential can sustain a global, long lasting, spiral pattern.

Figure 3.2 shows density snapshots of model HD2, with the same scale as shown in Figure 3.1 for model HD1. As expected, since F is increased to 10 %, the spiral arms are much stronger. The global pattern persists for many orbits, but the arms are clearly more dynamic. As early as one orbit after the potential is fully applied (at $t/t_{orb} = 2$), the spiral arms at ∼7.5 kpc, indicated by the arrow in Figure 3.2(b), bifurcates. This region

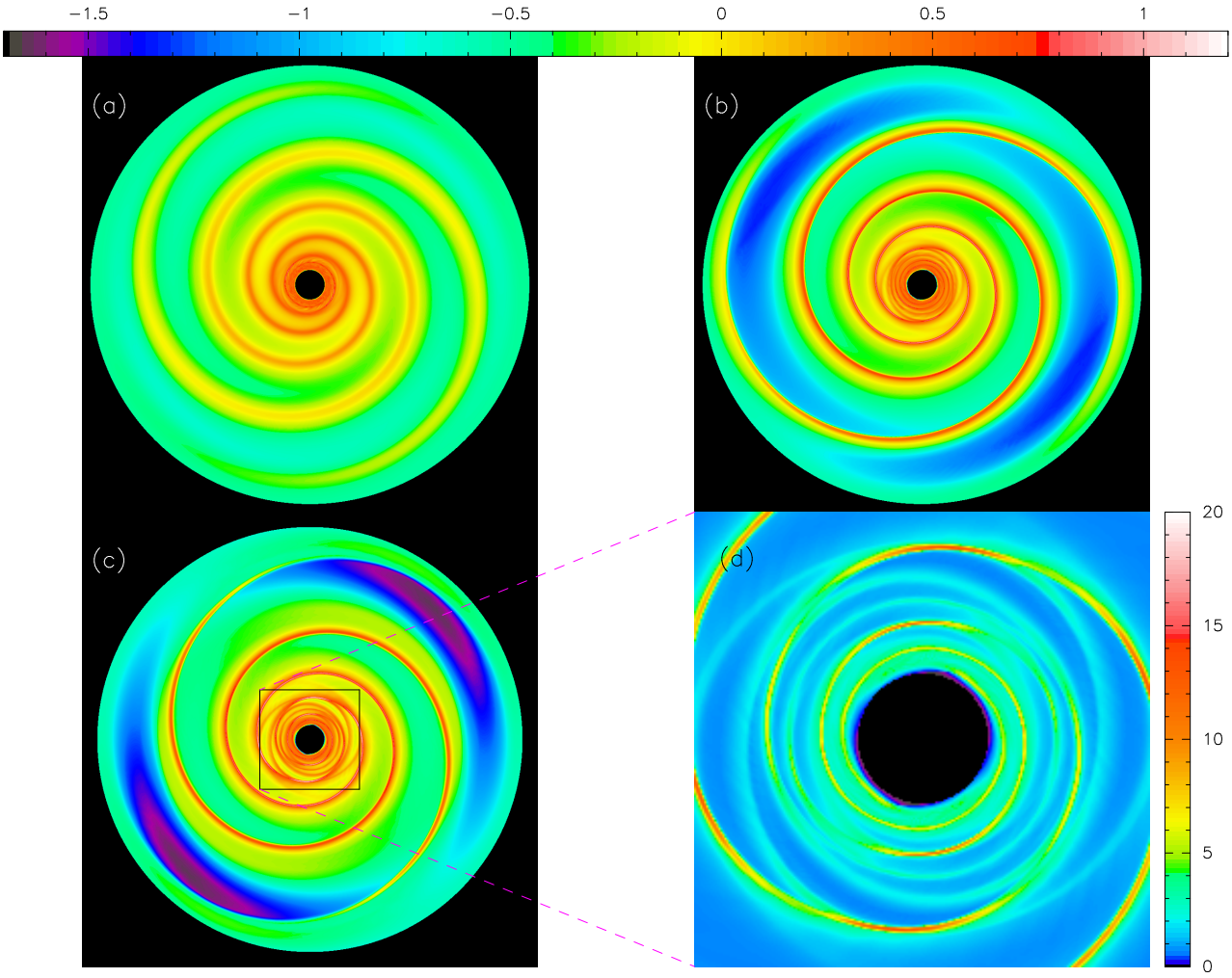

Figure 3.1: Snapshots from non self-gravitating, unmagnetized model HD1 (weak external spiral potential, F = 3%). Surface density at (a) $t/t_{orb} = 1$, when the external potential is turned on fully, (b) $t/t_{orb} = 2$, and (c) $t/t_{orb} = 3$. (d) Inner 6.8 $\times$ 6.8 kpc^2 box shown in (c). The color scale for (a), (b), and (c) is shown above (a) and (b), in units of $\log(\Sigma/\Sigma_0)$. Color scale for (d) is shown adjacent to (d), in units of Σ/Σ_0.

is near the inner Lindblad resonance (ILR). The bifurcation causes the arm at $\sim$7 kpc to lose matter, and it thus becomes weaker than the arms located farther inward. Further, the arm at $\sim$9.3 kpc has a much different pitch angle from the arms at different locations. After an additional orbit, the bifurcated part of the inner arm has moved radially outward and connected with the outer arms. In the meantime, the arms that lost matter during bifurcation regain strength and attain a surface density similar to the arms in the inner regions.

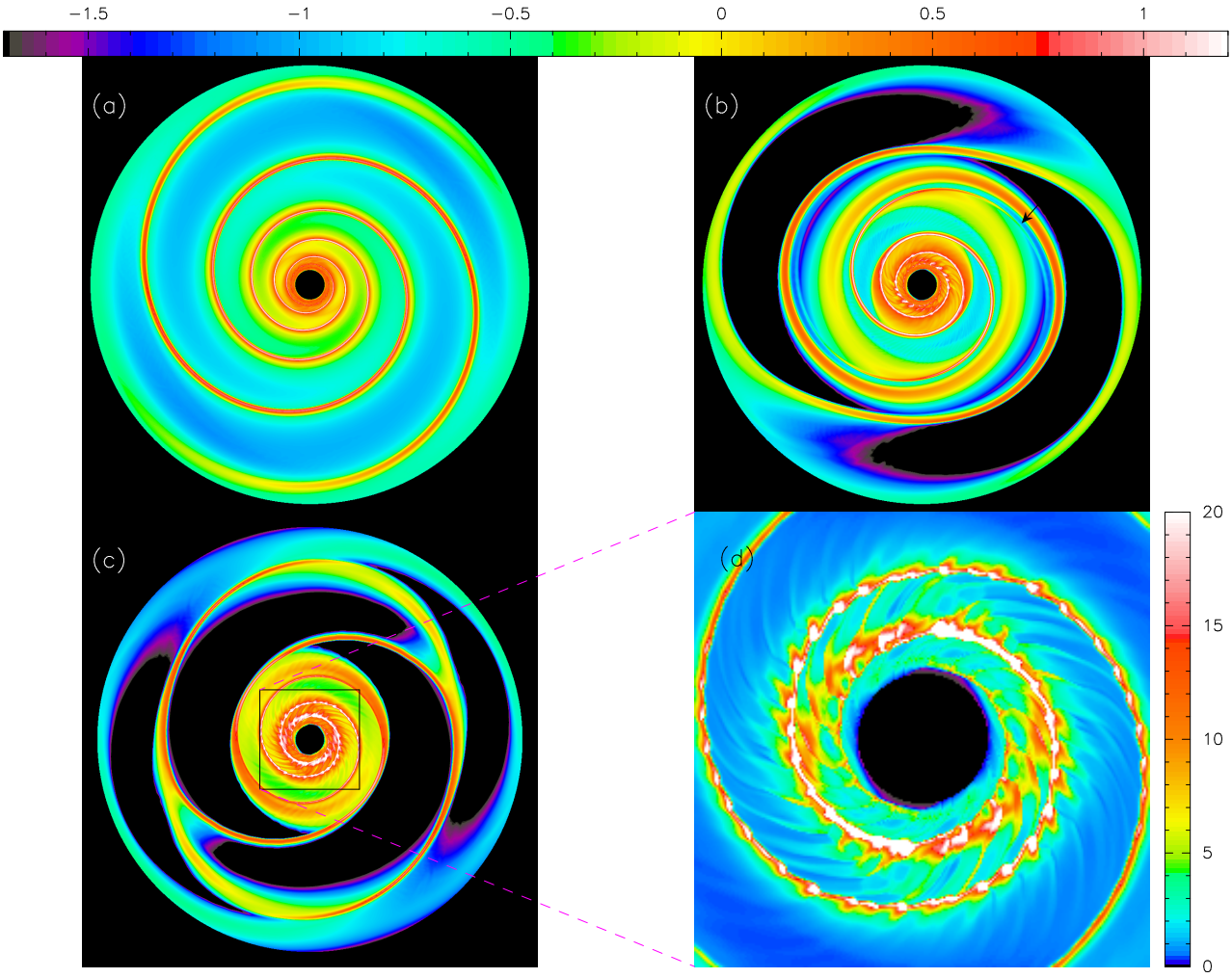

Figure 3.2: Snapshots from non self-gravitating, unmagnetized model HD2 (strong external spiral potential, F = 10%). Surface density at (a) $t/t_{orb} = 1$, when the external potential is turned on fully, (b) $t/t_{orb} = 2$, and (c) $t/t_{orb} = 3$. (d) Inner 6.8 × 6.8 kpc^2 box shown in (c). The color scales are arranged in the same manner as in Figure 3.1.

Figure 3.2(d) shows the central regions of model HD2 at t/t_{orb} = 3. Here, unlike in the case with a weaker potential (Fig. 3.1(d)), the arms remain continuous and distinct. However, there are also prominent interarm filamentary features, some even connecting two adjacent arm segments. Such features can be seen to develop as early as t/t_{orb} = 2, in Figure 3.2(b). WK found similar features, which they identified as spurs or fins, in their hydrodynamic models (the detailed morphology differs because they use a different rotation curve). They attribute the formation of their spurs or fins to the Kelvin-Helmholtz

instability. In our models, these features only grow in the innermost regions; we show in the following section that magnetic fields prevent their formation.[2] We further show that it is the combination of magnetic fields *and* self-gravity that results in spurs forming everywhere in a disk, not just in the innermost regions.

Another difference between models HD1 and HD2 is the relative location of the gas density peaks of the arms. The gaseous arms in model HD1 (F = 3%) form farther downstream than in model HD2 (F = 10%). We discuss the offset between the dust lanes and the spiral potential minimum in §3.6, as well as compare with the results from the recent study by Gittins & Clarke (2004).

Changing the pattern speed of the spiral potential does not dramatically alter the resulting spiral structure. Figure 3.3(a) shows a snapshot of model HD3, one orbit after the external spiral potential with $F = 10\%$ is fully applied. Here, the corotation radius is at 5 kpc, instead of 25 kpc. The spiral structure is similar to that shown in Figure 3.2(b), but the arms are not as dynamic, and the bifurcation region is shifted inward, as expected if this phenomenon is indeed due to a resonance. For all our models the shock locus transitions from the concave to the convex side of the gaseous arm at or near corotation. Inside this radius, the shock front is located on the concave side of the gaseous spiral arm. Farther out in the disk, the shock front moves to the outer, convex side of the arm.

Figure 3.4 shows the density and velocity profiles relative to the external spiral potential in two regions inside and outside corotation for model HD3. For both regions, the gas peaks occur downstream from the minimum of Φ_{ext}. Inside corotation, the gas shocks after the gas passes through the spiral potential. Outside corotation, the spiral pattern passes through the gas, leaving the shocked gas behind. The shock front itself is always upstream from the density peak. Thus, inside corotation the shock occurs on the inside

[2]Recent models by Kim & Ostriker (2006) have also shown that the instability identified by WK is suppressed by three-dimensional effects even in unmagnetized models.

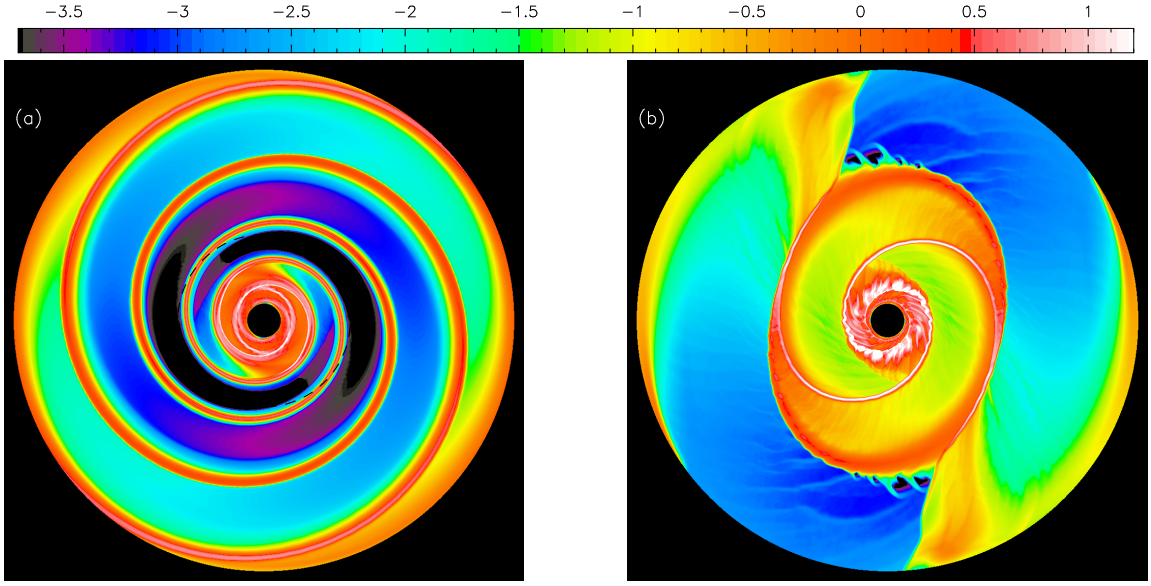

Figure 3.3: Snapshots at $t/t_{orb} = 2$, from models HD3 (a) and HD4 (b). Parameters are the same as in model HD2 (Fig. 3.2), but with (a) Ω_p = 42 km s^{-1} kpc^{-1}, and (b) $i = 20^{\circ}$. The dashed circle in (a) indicates the corotation radius of 5 kpc. The color scale shows $\log(\Sigma/\Sigma_0)$.

face of the spiral arm, while outside corotation the shock forms on the outer face of the arm. The density and velocity profiles in Figure 3.4 are quite similar to those obtained using local models (e.g. Figs. 2, 3 of KO). We note that in regions closer to corotation, the gas peaks lie near the minimum in Φ_{ext}, and shocks cannot be clearly distinguished.

The secondary density hump in the profile inside corotation occurs near the 4:1 ultraharmonic resonance, where $\Omega_p - \Omega = -\kappa/4$ (if pressure effects are ignored). CLS also identified similar secondary features in their global hydrodynamic models, which they denote as "branches." They also find such branches near locations of the 6:1 ultraharmonic resonance. Qualitatively, the formation and subsequent evolution of the branch features in our models are similar to those shown in CLS.

Models with a larger pitch angle show some differences from those with more tightly wrapped arms. Figure 3.3(b) is a snapshot of model HD4, again one orbit after the full spiral potential is applied. Similar to the results of WK, this model shows that loosely wound spiral arms are much more unstable than tightly wound arms, because the shock is

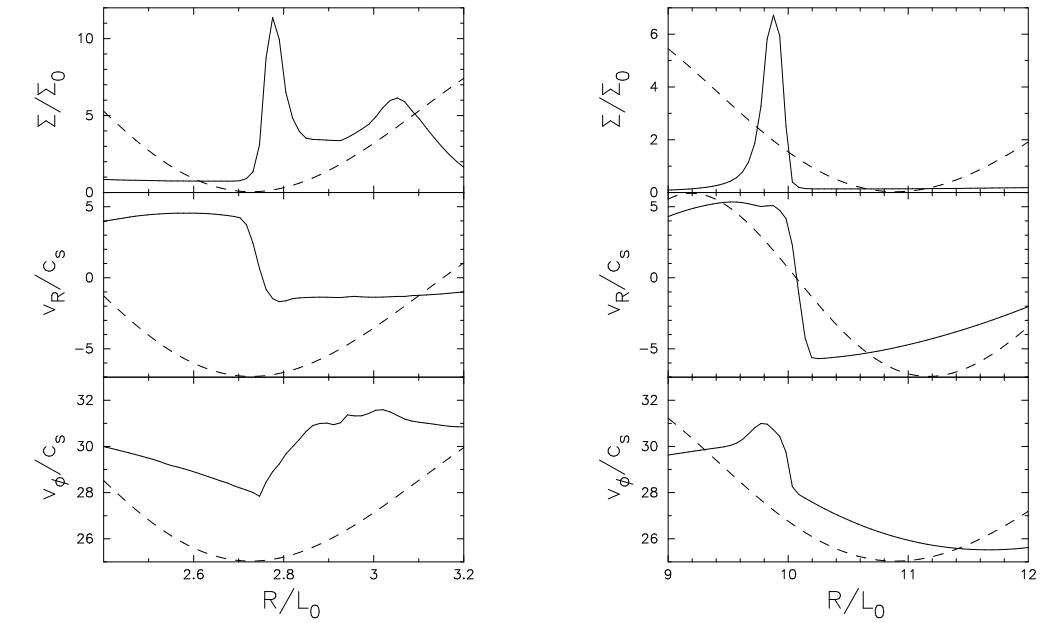

Figure 3.4: Density, radial, and tangential velocity as a function of radius from model HD3 (shown in Fig. 3.3(a)), at time t/t_{orb} = 1.26. Quantities are taken from locations of constant azimuth, from a region inside corotation (left), and a region outside corotation (right). The corotation radius is R_{CR}/L_0 = 5. The dashed line in each plot shows the external spiral potential.

stronger. The bifurcation is clearly evident, and results in replenishment of the depleted arms in the outer regions after an additional orbit. The interarm sheared filamentary features in the inner region of the galaxy are more pronounced than in the corresponding model with i=10°, shown in Figure 3.2(b).

3.3.2 Magnetohydrodynamic Models

Before including self-gravity, we test the effect of magnetic fields on non-self-gravitating disks with a spiral potential. Figure 3.5 compares snapshots at $t/t_{orb} = 2.0$, of a model without magnetic fields, HD2, to one with magnetic fields, MHD1. Clearly, the interarm features described in the previous section no longer appear in the magnetized case. Thus, equipartition-strength magnetic fields are able to suppress the "wiggle instability" identi-

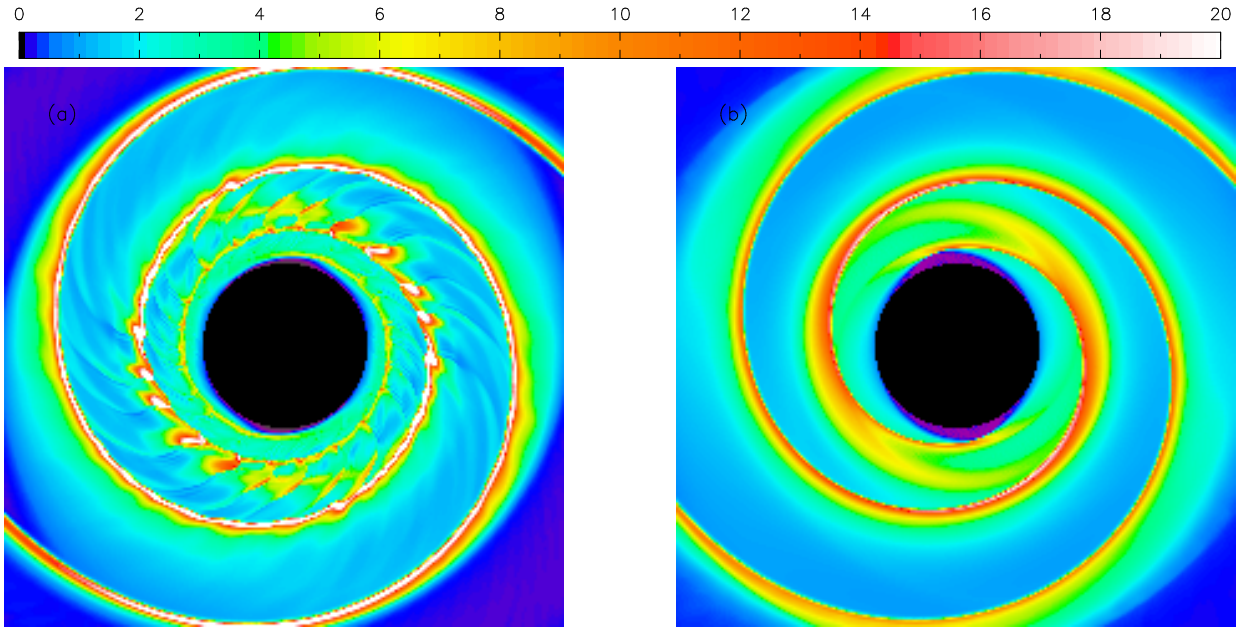

Figure 3.5: Snapshots at $t/t_{orb} = 2$ of the inner 6.8×6.8 kpc^2 of model (a) HD2 and (b) MHD1. The color scale is in units of Σ/Σ_0.

fied by WK in large F simulations (for a small enough F, as seen in model HD1, there is stability even in unmagnetized models).

3.4 Models Including Gas Self-Gravity

To include self-gravity in our simulations, we must introduce an additional parameter, which we choose to be the Toomre parameter Q_0 evaluated at R_0, given in equation (3.8). Table 3.2 shows the input parameters for models including self-gravity. The first five columns are the same as those in Table 3.1, and column (6) gives the value of Q_0. As shown in equation (3.8), $Q \propto \kappa/\Sigma$.

Table 3.2. Parameters for Models Including Gas Self-Gravity

Model [a] (1)	β (2)	F (%) (3)	Ω_p (km s^{-1} kpc^{-1}) (4)	i (°) (5)	Q_0 (6)
SHDne1	∞	0	-	-	1
SHDne2	∞	0	-	-	2
SMHDne	1	0	-	-	1
SMHD1	1	3	8.4	10	2
SMHD2	1	10	8.4	10	2
SMHD3	1	10	8.4	10	1
SHD1	∞	10	8.4	10	2
SMHD4	1	10	42	10	2
SMHD5	1	10	8.4	20	2

[a]Models listed in the text with a prime (e.g. SHDne1′) have $\Sigma \propto R^{-2}$; otherwise, $\Sigma \propto R^{-1}$

3.4.1 Disk Stability Tests for Constant Q Models

For disks with constant circular velocities, the epicyclic frequency $\kappa \propto R^{-1}$; thus if the initial density distribution $\Sigma \propto R^{-1}$, Q will be constant for the whole disk. We first consider models in which the initial surface density profiles are indeed inversely proportional to the galactocentric radius. Such a distribution is consistent with many surface density profiles shown in Regan et al. (2001); Wong & Blitz (2002).

To test the inherent stability of disks with constant Q, we consider cases with self-gravity, but with no external potential, models SHDne1, SHDne2, and SMHDne, shown in Figure 3.6. Since the initial density has random white-noise 0.1% perturbations, the over-dense regions can grow due to self-gravity. As these regions grow, they also become stretched azimuthally due to the background shear. The runaway growth of the over-dense regions eventually causes neighboring regions to have extremely large velocities, such that the Courant condition would require an extremely small time step; we therefore

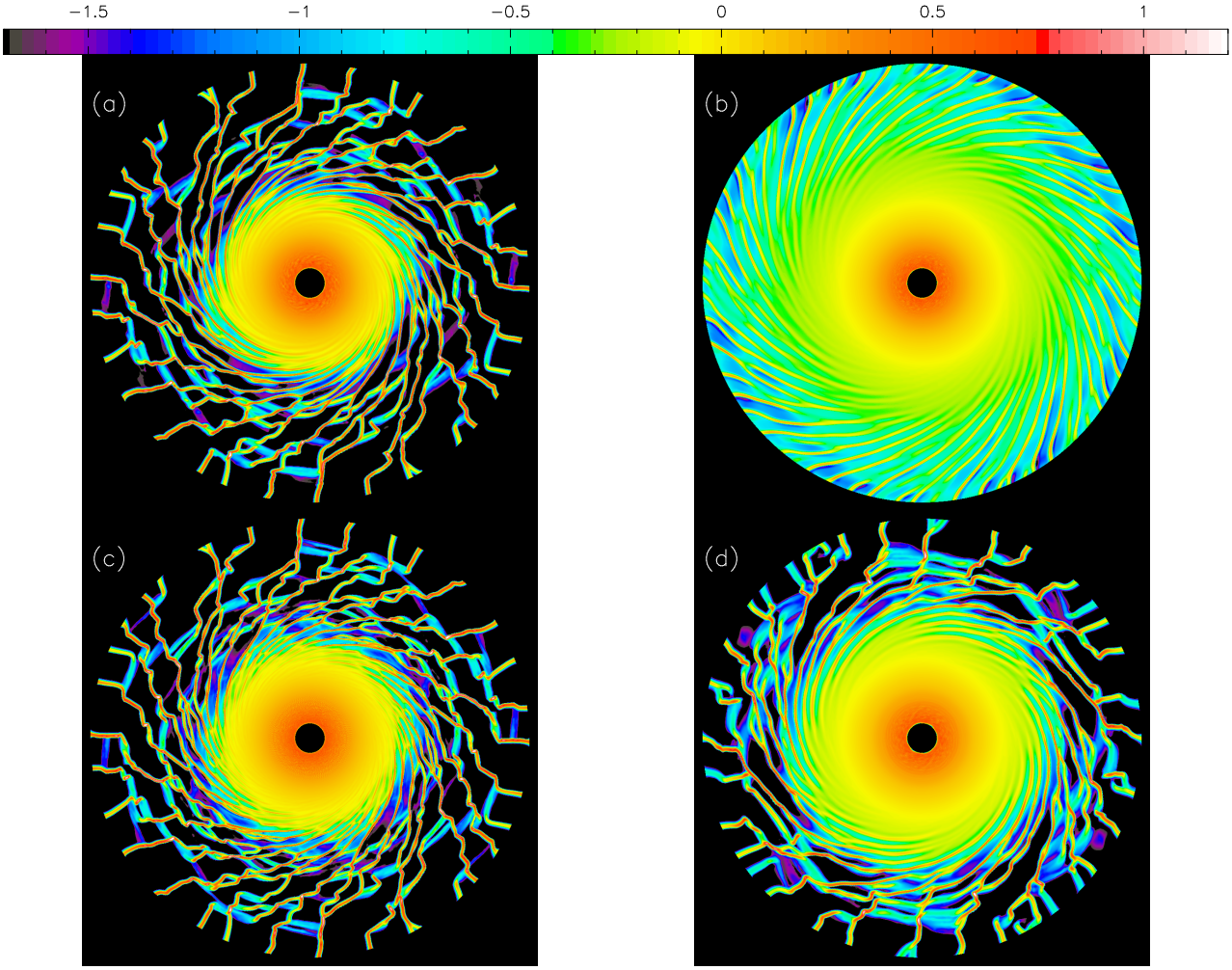

Figure 3.6: Snapshots of models with self-gravity but no external potential. (a) SHDne1 ($Q_0 = 1$) at $t/t_{orb} = 0.97$, (b) SHDne2 ($Q_0 = 2$) at $t/t_{orb} = 0.97$, (c) SMHDne ($Q_0 = 1$, $\beta = 1$) at $t/t_{orb} = 0.97$, and (d) SHDne2 ($Q_0 = 2$) at $t/t_{orb} = 1.49$. The color scale is in units of $\log(\Sigma/\Sigma_0)$.

halt the simulation. Model SHDne1 has Q_0=1, and becomes unstable very rapidly (within one orbit at R_0), as shown in Figure 3.6(a). Figure 3.6(b) shows model SHDne2, with Q_0 = 2, at the same time as the Q_0 = 1 model in Figure 3.6(a). Since the Q_0 = 2 model is more stable, not enough time has yet elapsed for the over-dense regions to dominate.

The addition of magnetic fields, as shown in Figure 3.6(c) from model SMHDne with Q_0 = 1, does not affect the growth of filaments significantly. The subtle difference is that the magnetic fields slow the growth of over-dense regions slightly. As a result, models

including magnetic fields evolve longer before the flow velocities in some zones becomes extreme. Figure 3.6(d) is the last snapshot of model SHDne2 at t/t_{orb} = 1.5 orbits. Here, the outer regions have evolved to the point that the structure is similar to that in Figure 3.6(a). However, it is clear that the radius of the stable inner region in the Q_0 = 2 model is larger than that of the Q_0 = 1 model (SHDne1). As expected, increasing the value of Q_0 increases the area of stability in the inner regions, and requires more time for the instability in the outer regions to grow.

The stability tests show that filament-like structures will grow in a shearing disk with sufficient gas surface density, regardless of the presence of magnetic fields. The Toomre stability parameter governs which regions are prone to gravitational instabilities. As Q_0 increases, the outer disk becomes more stable, and more time is required for growth of instabilities. In the models presented thus far, we have considered disks for which the initial surface densities vary as R^{-1}, so that Q is initially constant everywhere in the disk. The reason that the outer disk becomes unstable even when the inner disk does not is that the disk thickness H is constant throughout the disk. The finite thickness stabilizes the inner disk more than the outer disk, because the ratios of H/λ_T and H/λ_J vary as R^{-1} for constant Q models, where the Toomre wavelength $\lambda_T = 4\pi^2 G\Sigma/\kappa^2$ and the Jeans wavelength $\lambda_J = c_s^2/G\Sigma$. We discuss this effect in §3.5.4.

3.4.2 Disk Stability Tests for $Q \propto R$ Models

The models we have presented so far have an initial surface density distribution proportional to R^{-1}, yielding a constant value of the Toomre parameter with R. However, the surface density distributions shown by Wong & Blitz (2002) are in many cases approximately consistent with a surface density distribution proportional to R^{-2}. Further, in the observational analysis of Martin & Kennicutt (2001), Q varies with radius for many galaxies. A variety of radial distributions are evident, some close to R^{-1} and others close

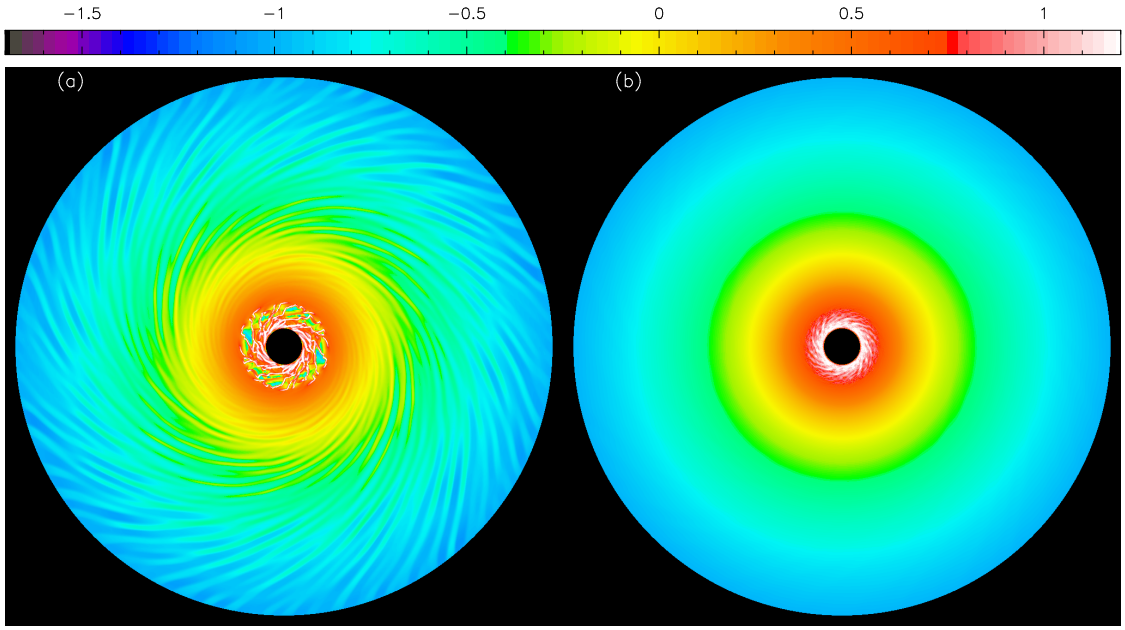

Figure 3.7: Snapshots at t/t_{orb} = 1.0 of models with $Q \propto R$; (a) SHDne1′ ($Q_0 = 1$) and (b) SHDne2′ ($Q_0 = 2$). The color scale shows $\log(\Sigma/\Sigma_0)$.

to R^{-2}. We thus consider models similar to those presented thus far, but with initial R^{-2} surface density distributions, such that $Q \propto R$. The labels of such models follow the convention of those already presented, but with the addition of a prime ($\prime$).

Figure 3.7 shows snapshots of disk models without an external potential, SHDne1′ and SHDne2′, at $t/t_{orb} = 1.0$. For SHDne1′, the value of Q ranges from 0.21 at the inner boundary to 3.15 at the outer boundary. The respective values are twice as large in model SHDne2′. When compared with Figure 3.6, it is clear that these models are much more stable. Only the innermost region in SHDne1′ shows more instability than SHDne1, the corresponding disk with Σ initially $\propto R^{-1}$ (Fig. 3.6(a)). As expected, since Q increases with R, the outer regions of the disk are more stable, and thus less susceptible to gravitational instabilities. In fact, there has been very little growth of perturbations in model SHDne2′ (Q_0 = 2) at one orbit (Fig. 3.7(b)). However, given enough time, the instabilities eventually begin to grow in this disk, and will appear similar to the snapshot in Figure 3.7(a).

3.4.3 Spiral Models with Constant Q

To investigate the interaction between gaseous self-gravity and the global spiral structure, we focus our presentation on six spiral models with parameters shown in Table 3.2. In addition to these models, we have performed additional simulations with a wide range of values and combinations of the chosen parameters, with similar characteristic results. For our fiducial model, $\beta = 1$, Ω_p = 8.4 (corresponding to a corotation radius of 25 kpc, which is outside the edge of the disk), $i = 10^\circ$, and Q_0 = 2. The external potential strength F will be indicated, as will cases where the other parameters differ from the fiducial one.

Figure 3.8 shows the fiducial model with F = 3% and 10%, SMHD1 and SMHD2, respectively, each at t/t_{orb} = 1.0 and 1.125. The most striking aspect of the snapshots, besides the spiral arms, are the interarm features. These features differ significantly between the two models, with the differences enhanced at the later times. This is shown for the central region in detail in Figure 3.9. With a weak external potential (SMHD1), the interarm features are strong as far inwards as 7 kpc. However, with the strong external potential (SMHD2), the interarm features are strong in the outer regions, but at radii of $\sim$5 - 11 kpc they are weak. In the inner regions, at R 5 kpc, the interarm features are again much stronger than the background; there are no strong interarm features in the innermost region of SMHD1. The reason for this difference in interarm features is clear in the structure of the arms themselves. In the F = 3% model, the arms inside 7 kpc are smooth. In the F = 10% models, on the other hand, the arms are broken into many clumps. The strong external potential in model SMHD2 has gathered more matter into the spiral arms, and self-gravity causes concentrations to grow, with much of the gas eventually collapsing into clumps. Gas flowing through the arms can be concentrated by these growing clumps, and returned to the interarm regions as overdense spurs. Since the stronger spiral potential of model SMHD2 concentrates more gas in the arms, the interarm regions at radii of $\sim$5

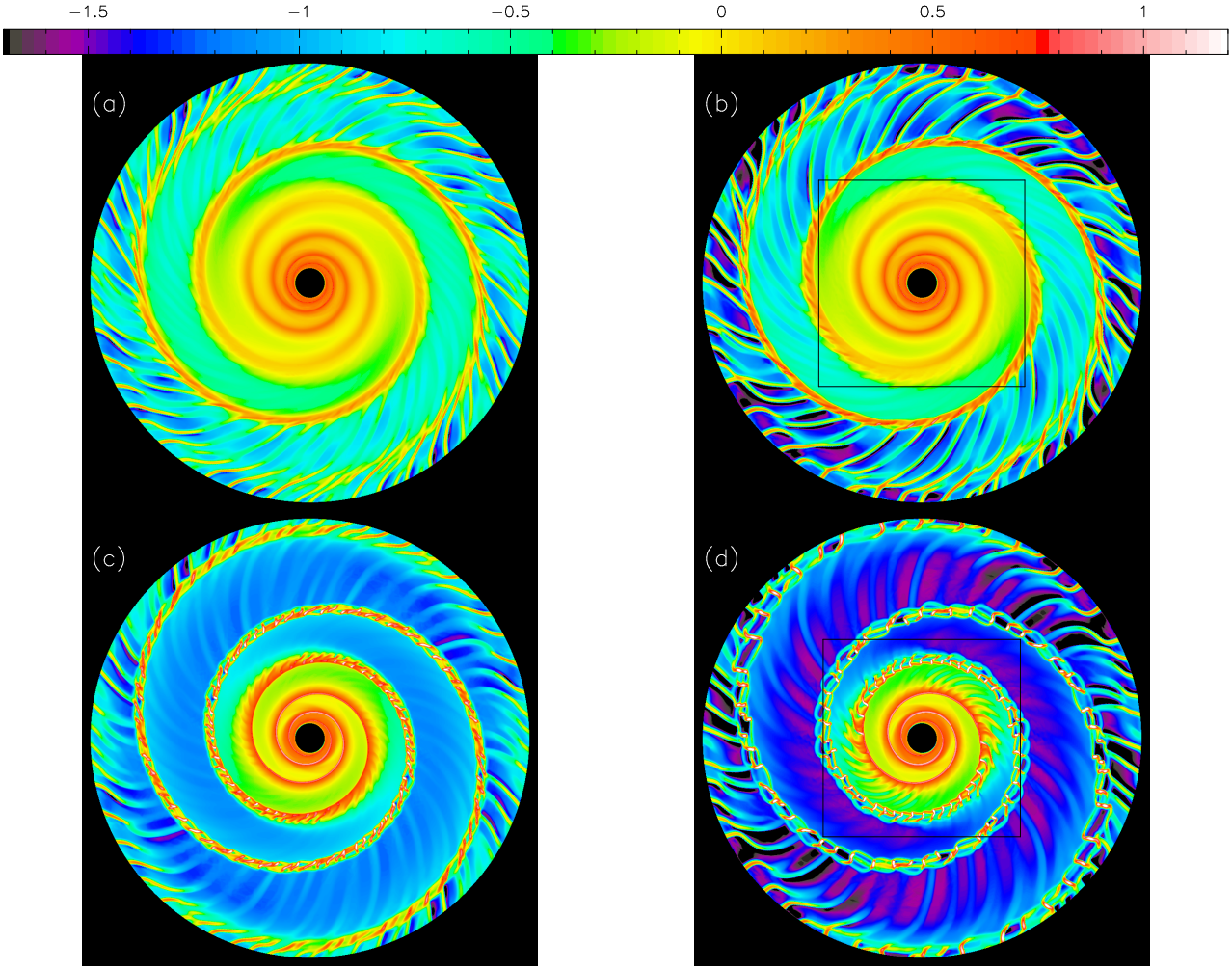

Figure 3.8: Models SMHD1 ($F = 3\%$) and SMHD2 ($F = 10\%$). SMHD1 at (a) t/t_{orb} = 1.0 and (b) t/t_{orb} = 1.125. SMHD2 at (c) t/t_{orb} = 1 and (d) t/t_{orb} = 1.125. The boxed regions in (b) and (d) are the inner 14 $\times$ 14 kpc^2 shown in detail in Figure 3.9. Units of color scale are $\log(\Sigma/\Sigma_0)$.

- 11 kpc has less gas compared to model SMHD1 with a weak spiral potential; as a result the interarm features in this region are weaker in model SMHD2.

The boxed region from Figure 3.9(b) is shown in detail in Figure 3.10 with the instantaneous velocities, including the unperturbed velocity field. Far from the spiral arms, the instantaneous velocities do not differ much from the initial circular velocities. As expected, the velocities of gas near the arms are significantly perturbed. Furthermore, the over-dense clumps in the arm flow along the arm. At this stage, gravitationally bound

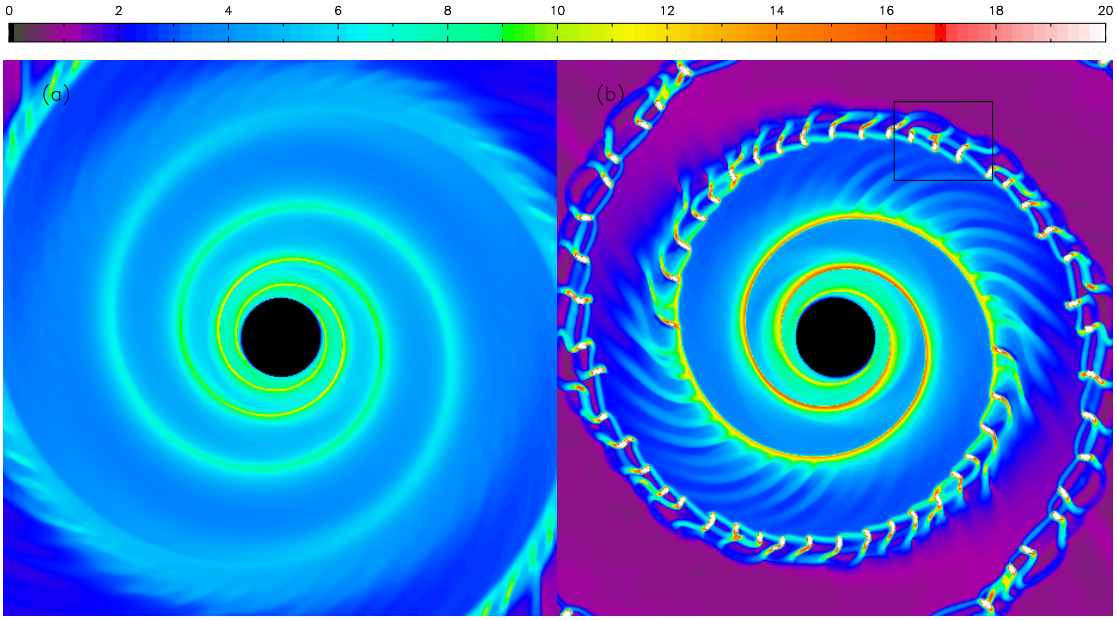

Figure 3.9: Inner 14 $\times$ 14 kpc^2 of Figure 3.8(b) and 3.8(d). (a) Detail of F = 3% model from box shown in Figure 3.8(b), and (b) detail of F = 10% model from box shown in Figure 3.8(d). The color scale shows Σ/Σ_0. The boxed region in (b) is shown in Figure 3.10.

structures do not leave the gaseous spiral arm, but continue to build in mass as matter from the interarm regions flows into the arm. If kept unchecked, the arm clumps would grow in a runaway fashion.

The overlaid contours in Figure 3.10 indicate magnetic field lines. Initially, the magnetic field is directed only in the azimuthal direction. As the spiral arms increase in density, the magnetic field is concentrated in the arms, thereby weakening the field in the interarms. The growth of the clumps along the arms further perturbs the field lines. However, only strong density enhancements produce field perturbations; the interarm features emerging from the clumps and the background features that grow in models without an external spiral potential do not strongly affect the magnetic field.

Figure 3.11 shows snapshots from a model without magnetic fields. Both the interarm features and clumps within the arms grow much more rapidly compared with the corresponding model with magnetic fields, SMHD2 (in Fig. 3.8). As early as t/t_{orb} = 1.0, the

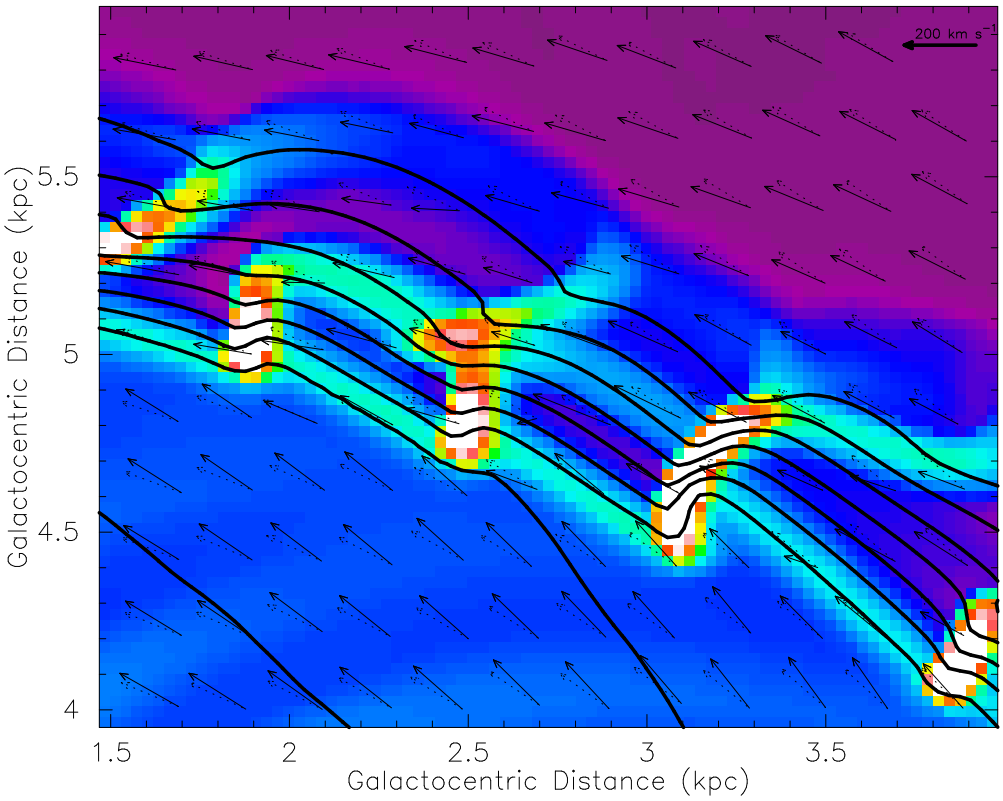

Figure 3.10: Boxed region from Figure 3.9(b) (Model SMHD2). Solid vectors show the instantaneous gas velocity in the frame rotating with the spiral potential ($\Omega_p = 8.4$ km s^{-1} kpc^{-1}, R_{CR} = 25 kpc). Dotted vectors show the initial velocities (pure circular motion). Scale of the vectors is shown by the thick vector (top right). Contours show magnetic field lines.

arm coherence in the outer regions is weakened due to the rapid growth of over-dense regions. Even in models with $\beta = 10$ (not shown here), the arms rapidly fragment. Similar to the models without self-gravity, strong magnetic fields act to preserve the overall arm shape, and suppress the growth of interarm features, either those caused by self-gravity, or by hydrodynamic effects.

Interarm features also grow more rapidly as the initial Toomre parameter Q_0 is reduced. Figure 3.12 shows the snapshots of SMHD3, a model similar to model SMHD2 except that $Q_0 = 1$ instead of 2. Even though this model has magnetic fields, the interarm features still grow relatively rapidly. Similar to low Q models without an external potential, this model is more susceptible to the growth of perturbations at smaller radii than the

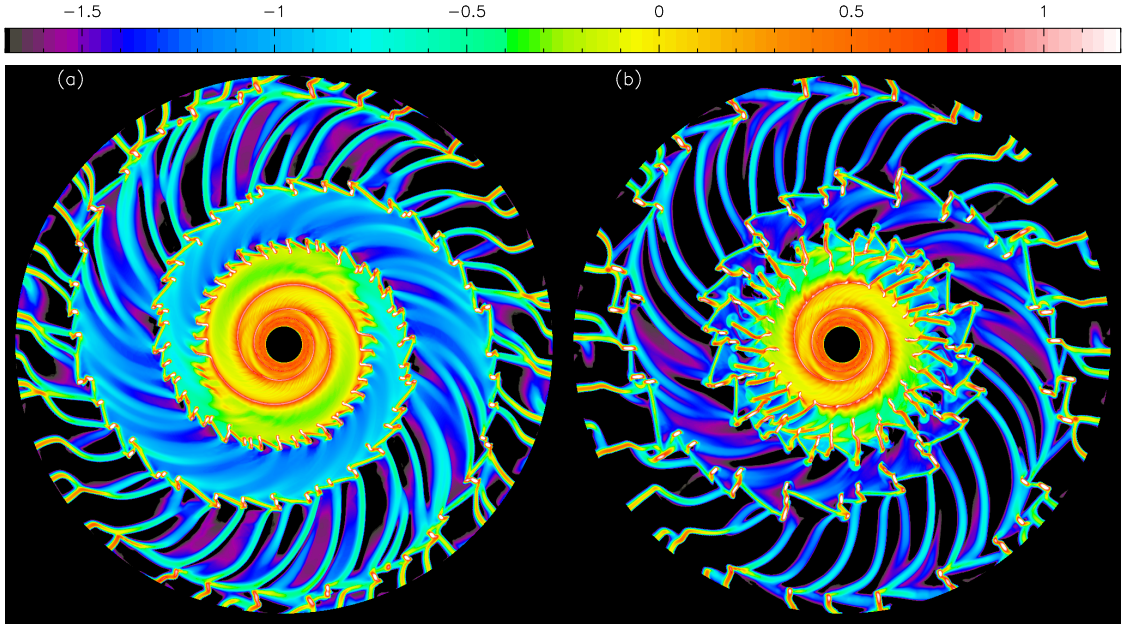

Figure 3.11: Model SHD1 ($F = 10\%$, $\beta = \infty$) at (a) t/t_{orb} = 1.0, and (b) t/t_{orb} = 1.125. The color scale is in units of $\log(\Sigma/\Sigma_0)$.

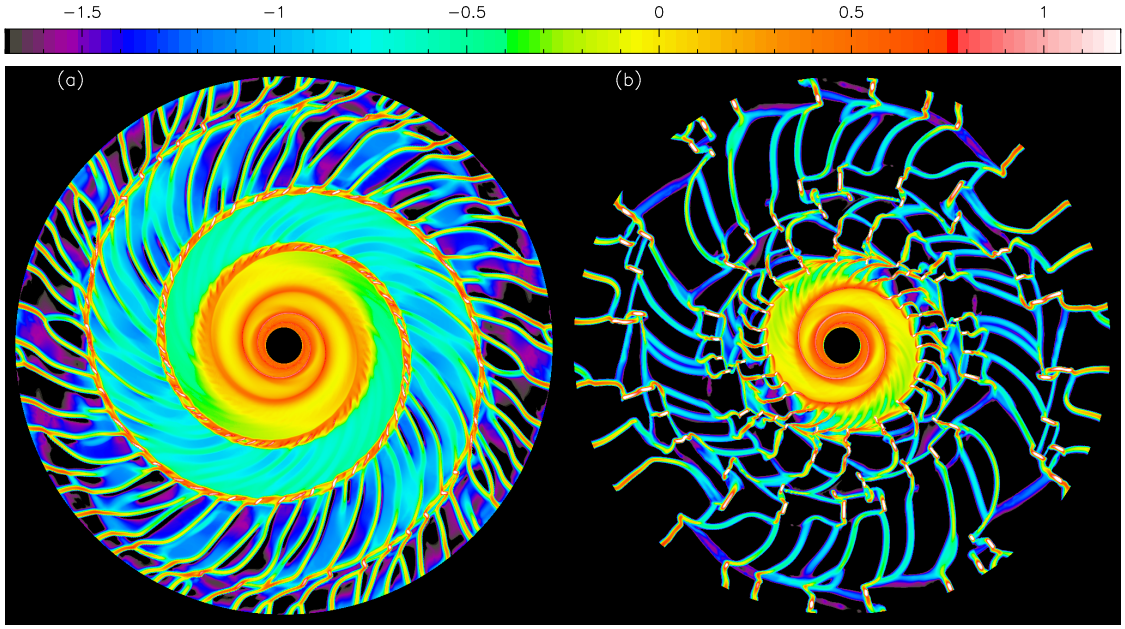

Figure 3.12: Model SMHD3 ($F = 10\%$, Q=1) at (a) t/t_{orb} = 0.75, and (b) t/t_{orb} = 1.0. The color scale shows $\log(\Sigma/\Sigma_0)$.

Q_0 = 2 model.

We have also explored models with varying values of the pattern speed and spiral pitch angle. Figure 3.13(a) shows snapshots after one orbit of model SMHD4. Model

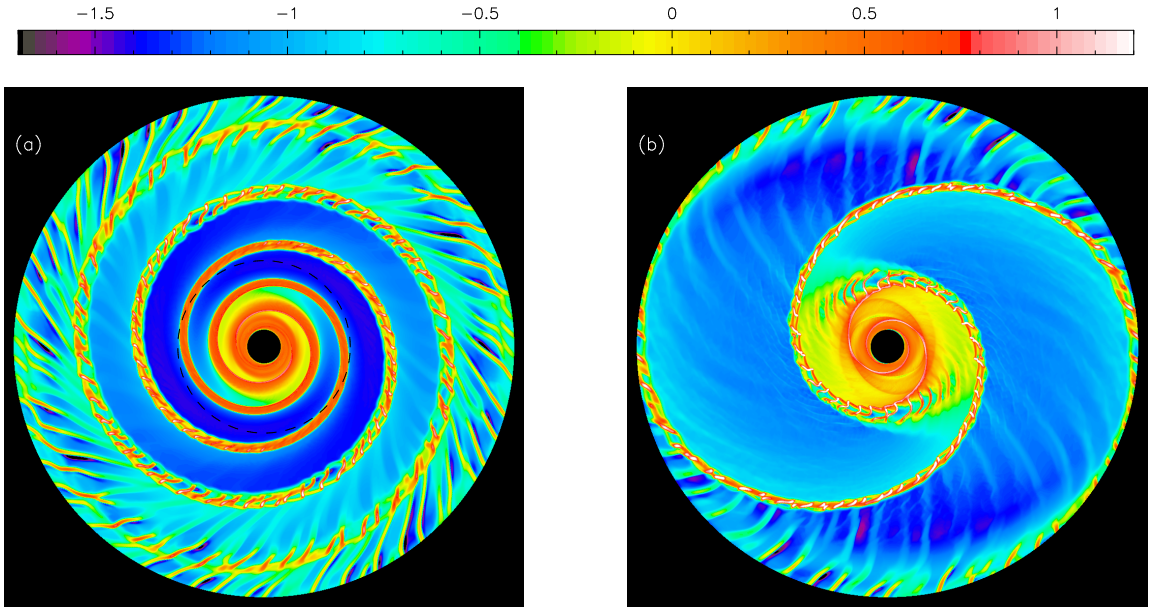

Figure 3.13: Snapshots at t/t_{orb} = 1 of model (a) SMHD4 (F = 10%, Ω_p = 42 km s^{-1} kpc^{-1}), with the corotation radius indicated by the dashed circle, and (b) SMHD5 (F = 10%, i = 20°). Units of color scale are $\log(\Sigma/\Sigma_0)$.

SMHD4 is similar to the fiducial model SMHD2, except that Ω_p = 42 km s^{-1} kpc^{-1}. The corotation radius for such a pattern speed is 5 kpc. At first glance, this snapshot may seem rather similar to the snapshot of model SMHD2 in Figure 3.8. However, in regions outside corotation the interarm features protrude inwards, towards the galactic center. The arms still have the over-dense knots, but the stretched features near the arms project in the opposite direction from those in the fiducial model. This is as expected, because outside corotation, the rotating spiral potential has a greater angular velocity than the gas. The flow enters the arms from the outer (convex) side, and leaves from the inner (concave) side. Azimuthally varying over- or underdense regions created within the arm return to the interarm region on the inside of the arm and are sheared into trailing structures. This reversed orientation is even more apparent in models where the Toomre parameter $Q \propto R$, as presented in §3.4.4. The trailing features in the outermost part of the disk arise in a different way, however, as we discuss in §3.5.

Model SMHD5, shown at t/t_{orb} = 1 in Figure 3.13(b), is similar to the fiducial model

but with a larger pitch angle of $i = 20^\circ$. Besides the expected difference in the shape of the spiral arms, many of the other features evident in SMHD2 (in Figs. 3.8(c) and (d)), such as the knots of matter in the arm and the trailing features in the outermost and innermost regions, are also present.

3.4.4 Spiral Models with $Q \propto R$

For spiral models with initial surface density distributions $\propto R^{-2}$, we only present cases with magnetic fields ($\beta = 1$); we have shown that magnetic fields act to keep the arms intact. Otherwise, self-gravity causes the runaway growth of the clumps in the arms. Figure 3.14 shows snapshots of model SMHD3′ (Q_0 = 1) and SMHD2′ ($Q_0 = 2$). Comparing with Figures 3.8, 3.9, and 3.12, these models are much more stable in the outer regions, as expected. Nevertheless, strong interarm trailing structures do grow in the inner $(14\ \mathrm{kpc})^2$. Since these models are more stable, the interarm features do not extend as far away from the spiral arms as those in the constant Q models. These features grow in both the $Q_0 = 1$ and 2 models, but are stronger in the $Q_0 = 2$ case. It is also clear that the interarm features connect with the most dense clumps in the arms, which are more dense in model SMHD2′ than SMHD3′.

Even though the self-gravitational force is stronger in model SMHD3′ ($Q_0 = 1$) than in model SMHD2′ (because the absolute Σ is larger in SMHD3′), the clumps in the arms of model SMHD2′ are more dense (relative to Σ_0). This results because more gas flows into the spiral arms in the more stable disk of model SMHD2′. As shown from the corresponding disk stability tests in Figure 3.7, the inner regions of models with $Q_0 = 1$ are much more unstable than models with $Q_0 = 2$. These background instabilities will grow regardless of the presence of an external spiral potential. For a stable disk as in model SMHD2′, stability of the background disk allows more gas to flow into the arms, resulting in stronger arms as well as clumps.

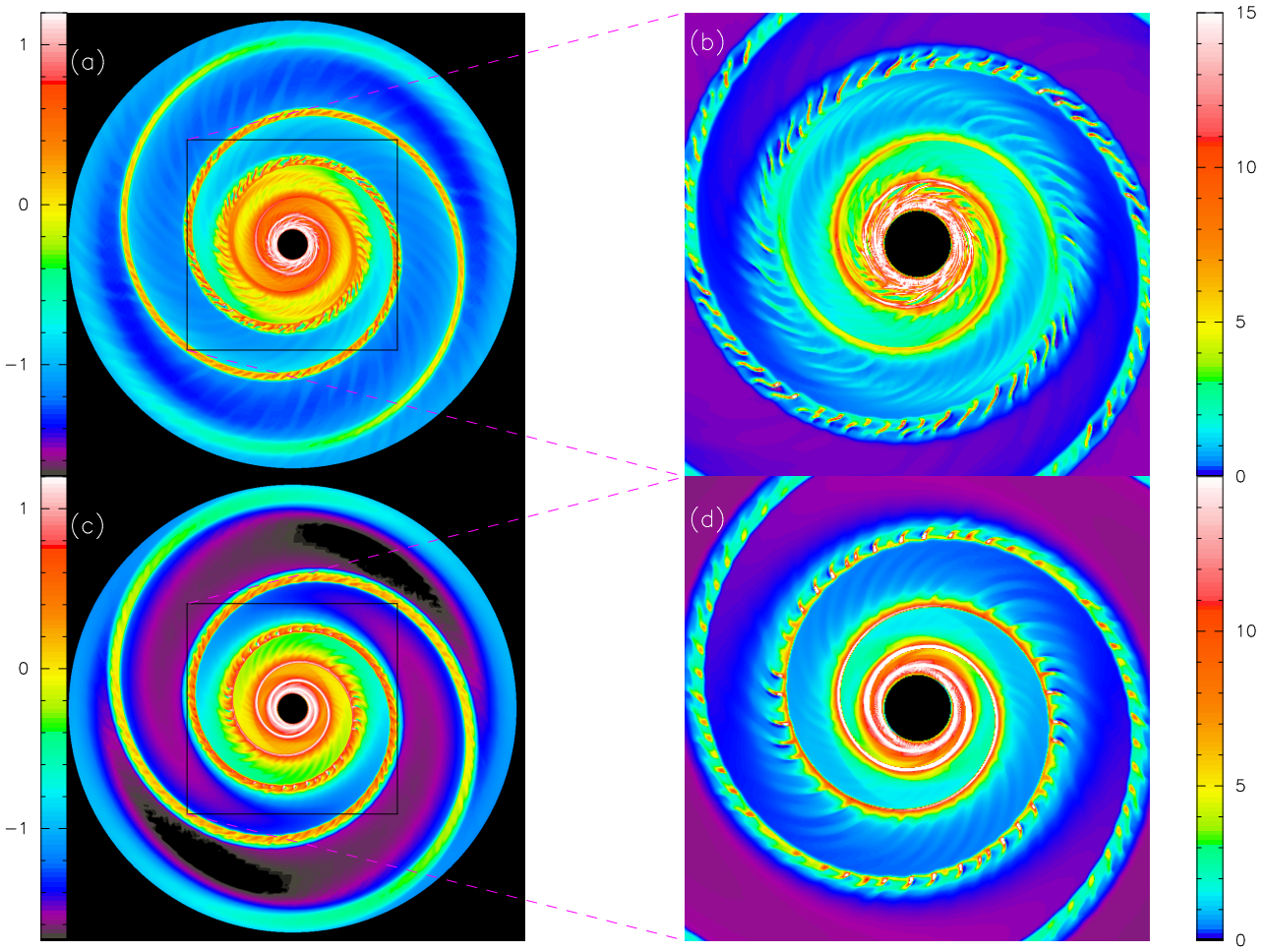

Figure 3.14: Snapshot of (a) SMHD3′ ($Q_0 = 1$, $F = 10\%$) at t/t_{orb} = 0.875 and (c) SMHD2′ ($Q_0 = 2$, $F = 10\%$) at t/t_{orb} = 1.125, along with the inner 14 × 14 kpc of each snapshot in (b) and (d). The color scales of (a) and (c) are in units of $\log(\Sigma/\Sigma_0)$, and scales for (b) and (c) are shown in units of Σ/Σ_0.

Figure 3.15 shows a snapshot of model SMHD4′, with large pattern speed (Ω_p = 42 km s^{-1} kpc^{-1}) at t/t_{orb} = 1.25. The corotation radius of 5 kpc is indicated as well. For this model, Q in the initial conditions varies from 0.4 at the inner radius to 6.3 at the outer radius. The nature of the interarm features in this model is much more clear than in the corresponding model with constant Q (SMHD4, shown in Fig. 3.13(a)). Inside corotation, the interarm features, which are connected with the arm clumps, occur exterior to the main spiral arms. However, outside corotation, the interarm sheared features emanate inwards from the main arms in the opposite sense from those inside corotation. This direction is

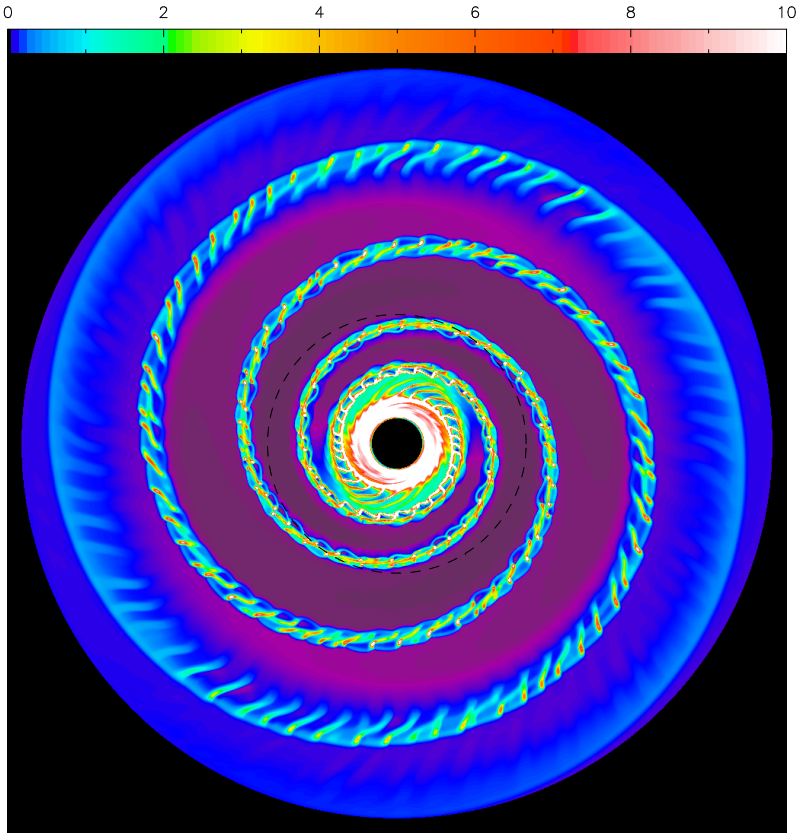

Figure 3.15: Snapshot of model SMHD4′ (Ω_p = 42 km s^{-1} kpc^{-1}) at t/t_{orb} = 1.25. The corotation radius is indicated by the dashed circle. The color scale is in units of Σ/Σ_0.

downstream from the arms, as seen in a frame rotating at Ω_p. Near corotation, clumps in the arms exist, but do not extend much either interior or exterior to the arms.

3.5 Analysis and Discussion

3.5.1 Arm Spurs or Sheared Background Features?

In our presentation and description of the models in §3.4, we have referred to the interarm structures we identify as "features," not "spurs." We define spurs as interarm features that are distinctly associated with spiral arms, intersecting the main spiral arms at locations where self-gravity caused the growth of clumps. Using this definition, spurs in the present global models would therefore be analogies of the structures studied in the local models

of KO.

Of course, it is well known that self-gravitating instabilities grow when the surface density is large enough, whether or not there is an external potential. The resulting overdense entities, which grow via swing amplification, are stretched due to the shear in the disk. The interarm features arising in our models with spiral perturbations have shapes similar to those in the stability test models, since the interarm shear profile is similar to that of the unperturbed velocity field. At first glance, it is therefore not obvious whether the interarm features in the spiral models are specifically due to the spiral perturbation, or whether they would arise regardless of the presence of the spiral perturbation.

Given, however, the dependence of the orientation of dense interarm features on the spiral pattern speed (or the corotation radius) as seen in Figures 3.13(a) and 3.15, it is clear that the external potential can have a significant effect. Depending on whether the spiral potential sweeps through the gas (outside corotation), or whether the gas overtakes the spiral potential (inside corotation), the interarm features in these cases grow inward or outward from the arm, respectively. This reversal of orientation indicates that the growth of such features is dependent on the spiral potential. These dense features, furthermore, are all connected to distinct arm clumps; they therefore fit our definition of "true spurs." On the other hand, the lower density interarm features evident in Figures 3.8(b) and 3.12(b) are similar to the structures seen in Figure 3.6 that grow in the absence of a spiral potential, provided the interarm surface density is sufficiently high. These "background features" are often *not* associated with arm clumps when they are present; we therefore do not consider them "true spurs."

We can quantify the effect of the spiral potential on outer-disk features by computing the dimensionless wavenumber of the background features $K_{y,feature} = \lambda_J/\lambda_{feature}$, where, $\lambda_J = c_s^2/(G\Sigma)$ is the local two-dimensional Jeans length, and $\lambda_{feature}$ is the mean azimuthal separation of the background features. Table 3.3 shows the feature separation

Table 3.3. Scale of Interarm Features

F [a]	$\lambda_{feature}$ [b]	$K_{y,feature}$ [c]
0	1.3	1.1
1%	1.3	1.1
3%	1.4	1.0
10%	1.7	0.8

[a]External Potential Strength

[b]Feature separation (kpc)

[c]$\lambda_J/\lambda_{feature}$; $\lambda_J = 1.4$ kpc

and the wavenumber for MHD models ($\beta = 1$) with the external potential strengths F = 0%, 1%, 3%, and 10%, for a region in the outer part of the disk. The other parameters are the same as the fiducial model: i = 10°, Ω_p = 8.4 km s^{-1} kpc^{-1}, and Q_0 = 2 (with initial surface density distribution $\propto R^{-1}$). For the feature separation $\lambda_{feature}$, we use the mean of the distances between the peaks of the interarm features at a radius of R = 9.9 kpc, along an arc of 80°, at $t/t_{orb} = 1$ (the feature separation does not vary much with time). At R = 9.9 kpc, using the initial surface density we find $\lambda_J = 1.4$ kpc. The table shows that the feature separation does not vary much with the strength of the external potential, suggesting that these outer-disk features are not "true spurs." In fact, the feature separation is always approximately the Jeans length. For model SMHD3 ($Q_0 = 1$, $F = 10\%$), the feature separation at the same radius is 1.2 kpc. The value of λ_J is half that of the $Q_0 = 2$ model, while the feature spacing decreases by 30%. This gives a ratio $K_{y,feature}$ that is $\approx 30\%$ smaller when $Q = 1$ than when $Q = 2$, but is still close to unity.

From Figure 3.9, it is clear that a strong external potential is required for interarm features to grow in the inner regions. Similarly, in $Q \propto R$ models (Fig. 3.14), stretched interarm features only grow near the arms in models with a strong external potential.

In models having $Q \propto R$ without an externally imposed spiral potential (Fig. 3.7(b)), sheared trailing features do not grow in the inner regions. Furthermore, the features that do grow in models with strong spiral potentials are connected to the clumps that form in the spiral arm itself. Thus, we identify the interarm features in the inner regions as true arm spurs, and for measuring the separation we replace the symbol $\lambda_{feature}$ by λ_{spur}. At $R \approx 4.5$ kpc, we measure values of $\lambda_{spur} \approx 0.6$ kpc, and $\lambda_J \approx 0.6$ kpc using the initial surface density. We find that the spur separation is again approximately equal to the Jeans length at ambient densities. If, instead, we had used the value of Σ in the arm, λ_J would decrease, giving the ratio $\lambda_{spur}/\lambda_{J,arm} \sim 5$.[3] For model SMHD3 ($Q_0 = 1$), both the values of λ_{spur} and the arm surface density (therefore $\lambda_{J,arm}$) are comparable to the values of those quantities in model SMHD2, although the initial background surface densities differ by a factor of 2. Thus, for $Q = 1$ the ratio $\lambda_{spur}/\lambda_{J,background} \approx 2$, and $\lambda_{spur}/\lambda_{J,arm} \approx 5$. Evidently, for "true spurs" the spacing depends more directly on $\lambda_{J,arm}$ than on $\lambda_{J,background}$. Even though spurs will grow in the inner regions only if there is a strong spiral potential, the distance between the spurs is still within a factor of 2 of the minimum scale length required for gravitational instability under uniform conditions; when $Q = 2$ the ratio $\lambda_{spur}/\lambda_{J,background}$ is indistinguishable from the case of "background features" that grow in the outer regions independent of the spiral potential. For realistic Q values near 2, the separation of filamentary structures is thus not sufficient in itself to determine their origin. The additional consideration of whether structures are connected to arm clumps or not discriminate between "true spurs" and swing-amplified "background features."

[3] In this region, $\Delta R \sim 25$ pc and $R\Delta\theta \sim 15$ pc, so the Jeans length using arm densities is resolved.

3.5.2 Spurs and Arm Clumps

As discussed above, we term the interarm features that grow out of arm condensations "true spurs." When interarm features grow as background effects, strong condensations can also grow within and remain in the arm. In this case, however, there is not a one-to-one relationship between interarm features and arm condensations (see e.g. the outer regions of Fig. 3.8(d) and Fig. 3.12(a)). In both situations, however, the arm condensations that grow are generally regularly spaced, similar to the "beads on a string" of bright HII regions often observed in spiral galaxies. The spacings between the clumps in the $Q_0 = 2$ model (SMHD2) at $R \approx 4.5$ kpc is typically $\sim$630 pc, comparable to $5\lambda_{J,arm}$ (measured using arm surface densities before fragmentation). In other models with distinct arm clumps, such as SMHD3 ($Q_0 = 1$), SMHD4 ($R_{CR} = 5$ kpc) and SMHD5 ($i = 20^\circ$) we measure clump spacings of $\sim$3 - $5\lambda_{J,arm}$.

We also measured the width W of the spiral arms. For the fiducial model SMHD2 ($Q_0 = 2$ and F = 10%), the FWHM $W \approx 210$ pc, for the same region of the arm for which the clump or spur spacing was measured. The ratio $\lambda_{spur}/W \sim 3$ is consistent with the observational study of Elmegreen & Elmegreen (1983) and the theoretical analysis of Elmegreen (1994). For the $Q_0 = 1$ model, SMHD3, we measure an arm width of $W \approx 600$ pc, and clump or spur spacing of ≈ 600 pc. Thus, when $Q_0 = 1$ the ratio λ_{spur}/W is close to unity. The measured ratio $\lambda_{spur}/\lambda_{J,arm}$ is therefore more consistent between our differing Q models than the ratio λ_{spur}/W, possibly due to magnetic fields and the physics of MJI (see KO). In practice, however, the observed range of Q might not be large enough to distinguish a difference.

For models shown in Figure 3.8 (and 3.9), only model SMHD2, with a strong spiral potential, shows distinct clumps in the arms. In the case with a weaker potential, the density transitions smoothly from the arm to the interarm features. Using the clump

finding algorithm `clumpfind` (Williams et al. 1994), we consistently measure the clump masses to be $M_{cl} \approx 10^7$ M$_\odot$ in the arms of model SMHD2. In terms of the Jeans mass,

$$M_J = \frac{c_s^4}{G^2 \Sigma} \tag{3.12}$$

and $M_{cl} \approx 10 M_J$ using mean arm surface densities. We measure similar values for the other models with distinct arm clumps. We find that altering the contour levels for the clump finding algorithm does not significantly change the total mass of clumps, but only increases the number of clumps found, giving similar masses for the new clumps. For models with weaker spiral potentials, strong clumps are not found in the spiral arms, so we cannot define clumps in the arm as easily; as discussed, the interarm features in models with weak potentials are not true arm spurs.

In observations of many galaxies, especially the *HST* and *Spitzer* images of M51 and other galaxies in the SINGS sample (Kennicutt et al. 2003; Scoville & Rector 2001), the strong interarm features indeed tend to intersect the brightest regions in CO along the main dust lanes (La Vigne et al. 2006). Vogel et al. (1988) found molecular complexes with masses of $10^7 - 10^8$ M$_\odot$ in M51, which they named giant Molecular associations (GMAs). In spiral galaxies for which the gaseous component is not predominantly molecular, large HI clouds have also been found to have masses of $\sim 10^7$ M$_\odot$; these are termed "superclouds" by Elmegreen & Elmegreen (1983). Both the GMAs and superclouds are analogous to the arm clumps in our simulations, which do not include the chemistry of the gas. In addition, La Vigne et al. (2006) measure feather spacings of $\sim$7 - 11λ_J in M51 and $\sim 1.5\lambda_J$ in NGC 0628, using surface densities in the arm to compute λ_J. These measurements assume the same value of c_s for both cases, and may be affected by uncertainty in the conversion of CO luminosity to gas mass. The consistency of clump masses and spur separations and the clump/spur connection in our models to the GMA masses, interarm feather separations, and GMA/feather association in M51 suggests that the strong spiral potential is directly responsible for producing these structures.

The orientation of spiral arm spurs indicates whether a given region is inside or outside corotation. Thus, the location of corotation can be identified if the transition from inward to outward directed spurs is observed. As discussed in KO, however, there are presently no known galaxies that exhibit clear inward projected spurs for a number of possible reasons, such as relatively weaker arms outside corotation, and current resolution limits.

3.5.3 Offset between Gaseous Arm and Potential Minimum

As indicated in §3.3, the relative location between the gaseous arm peak and the minimum in the spiral potential varies depending on the strength of the potential and the corotation radius. Figure 3.16 shows the azimuthal locations of these peaks, which would be observed as the main dust lanes, as a function of radius for three models relative to the potential minimum. The location of the potential minimum for models HD1 and HD2 at any given time is the same; only the strength of the potential differs. Inside corotation, the gaseous arms from models (including those not shown here) with stronger potentials form closer to, although always downstream from, the potential minimum. As shown in Figure 3.16(b), the gaseous arm shifts from downstream to upstream from the potential minimum at corotation.

Gittins & Clarke (2004), hereafter GC, find via the one-dimensional shock-fitting procedure of Shu et al. (1973) with local non-self-gravitating models, that the gas shock occurs upstream from the potential minimum. The magnitude of the offset depends on various parameters. They find that this offset approaches $-\pi$ at corotation, suggesting that the location of corotation can be constrained by measuring offsets between the arm in K band (tracing the potential) and molecular (gas) observations. In the cases studied by GC, the potential minima and the gaseous shock intersect well inside corotation. The location of this intersection varies depending on the strength of the spiral potential.

There are a number of possible reasons for the differences in offsets between our mod-

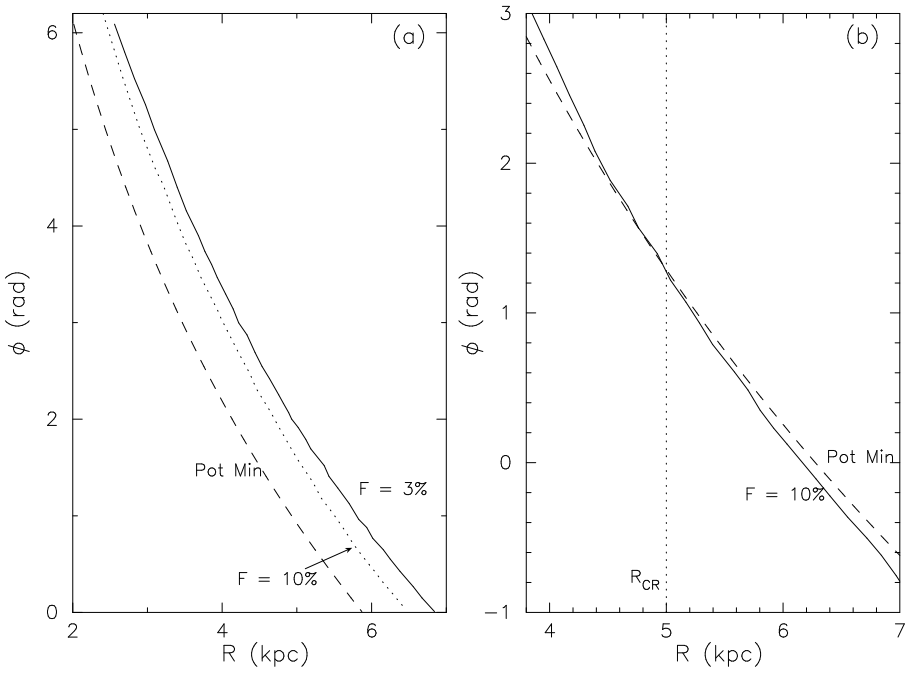

Figure 3.16: Location of potential minimum and gaseous arm peaks. (a) Models HD1 and HD2 with $F = 3\%$ and 10%, respectively, and (b) model HD3, with F = 10% and R_{CR} = 5 kpc.

els and the results of GC. Perhaps most importantly, we use a flat rotation curve, whereas GC use a velocity profile that varies with radius. In addition, we measure the position of the density peak (shocks are difficult to distinguish near corotation at our resolution) while GC report the position of the shock, which may be upstream from the density peak. Such differences between the parameters and analysis methods in our models and those of GC prevent a direct comparison of the results. We note that both studies include the effect of the stellar disk only as a fixed rotating spiral potential, i.e. an unresponsive component. The relative locations of the gaseous and stellar arms may well depend on the mutual self-consistent interaction between the two components, an important issue for future investigation.

3.5.4 Effect of Disk Thickness on Stability

In our calculation of the gaseous self-gravity, we (approximately) include the effect of disk thickness H (see Appendix). Including this disk thickness approximation, the local axisymmetric dispersion relation for an unmagnetized medium becomes:

$$\omega^2 = \kappa^2 + c_s^2 k^2 - \frac{2\pi G\Sigma|k|}{1+|k|H}. \tag{3.13}$$

When $H = 0$, the dispersion relation takes on its familiar form for razor thin disks (e.g Binney & Tremaine 1987). In order to solve for the minimum value of ω, we define

$$k_0 \equiv \frac{\pi G\Sigma}{c_s^2} = \frac{\kappa}{Qc_s}, \tag{3.14}$$

and

$$y \equiv k/k_0, \tag{3.15}$$

so that at ω_{min},

$$y(1+k_0 H y)^2 = 1. \tag{3.16}$$

The critical value of Q (where $\omega_{min}^2 = 0$) is then given by

$$Q_{crit}^2 + y^2 - \frac{2yQ_{crit}}{Q_{crit} + y(\frac{\kappa H}{c_s})} = 0. \tag{3.17}$$

We solve equations (3.16) and (3.17) simultaneously, and Figure 3.17 shows how Q/Q_{crit} varies with R, for disks with Q = 2. With the modified dispersion relation of equation (3.13), and H = constant, disk stability decreases with increasing R. As shown in Figure 3.17, in the inner regions disks with large values of H are much more stable than razor thin disks, for which $Q_{crit} = 1$ (Toomre 1964).

The stability profile for axisymmetric perturbations will also influence the stability of non-axisymmetric perturbations (e.g. Goldreich & Lynden-Bell 1965; Kim & Ostriker 2001; Toomre 1981). As seen in Figure 3.6, the outer regions of constant Q, constant H disks are unstable. The maximum radius of the inner stable region, R_{crit}, depends on Q,

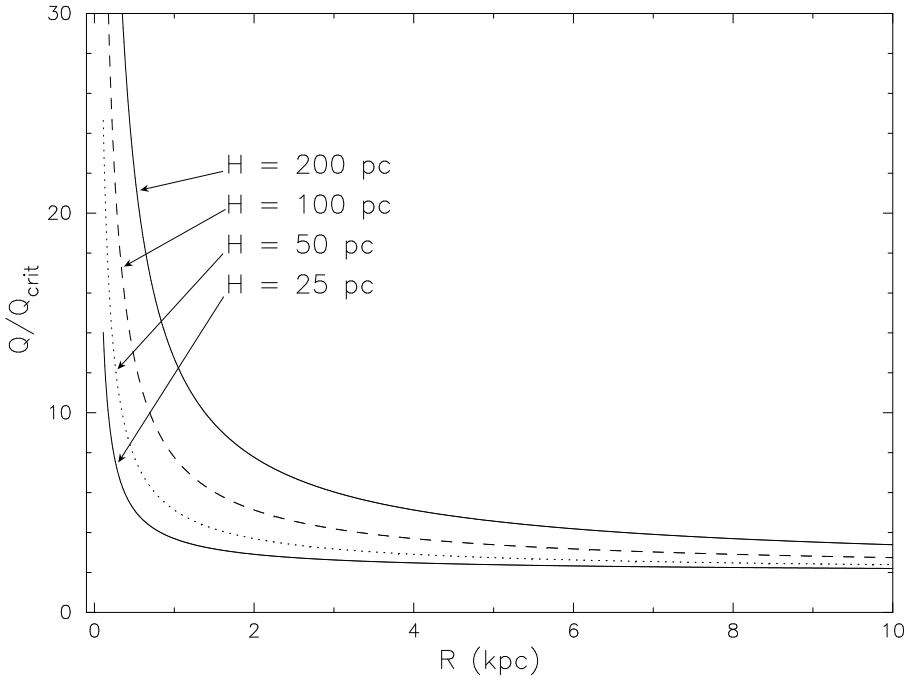

Figure 3.17: Q/Q_{crit} for Q = 2 models when disk thickness is included (see eqns. [3.13] - [3.16]).

and is constant in time. Models with varying thicknesses show that R_{crit} increases with larger values of H, qualitatively consistent with the stability profiles in Figure 3.17. We note that R_{crit} in our models with different values of H does not simply correspond to Q/Q_{crit} = constant, however. For example, with H = 25 pc, we measure R_{crit} = 5.2 kpc empirically, and Q/Q_{crit} = 2.4 at this location. On the other hand, for H = 200 pc, we measure R_{crit} = 7.8 pc, and Q/Q_{crit} = 3.7 at this location. Thus, the value of Q obtained from a modified dispersion relation (including the effect of thickness) is not sufficient for a complete characterization of non-axisymmetric stability limits in global models.

We also find that in models with smaller values of H, the instabilities (outside R_{crit}) grow sooner than in models with larger values of H. Furthermore, the spacing between the perturbations also vary if H is altered significantly. We find that increasing H by a factor of 8 increases the perturbation separation by a factor of $\sim$2.5. Slightly varying the thickness does not strongly affect the perturbation spacing, however. We also note that in

our implementation H = constant, which favors structures growing in the outer regions; other choices of the thickness profiles, such as H/R = constant, can result in stable outer regions combined with unstable inner regions.

3.6 Summary

We have investigated the growth of interarm features in self-gravitating gaseous disks of spiral galaxies using global MHD simulations. Our models are two-dimensional, but we account for the thickness of the disk in an approximate way in the computation of self-gravity. Gaseous spiral arms grow as a result of an externally-imposed rotating spiral potential, representing the stellar spiral arms of a galaxy. We explore a range of values for the physical parameters describing the properties of the disk. The main results are as follows:

1) In the inner regions of disks without self-gravity or magnetic fields, we are able to reproduce the interarm features that WK found in their models. When spiral shocks are strong enough, hydrodynamic instabilities cause the growth of knots in the spiral arms, and the shear causes interarm features to spread from these knots. However, we find that including magnetic fields gives more tensile strength to the spiral arms and suppresses the growth of such features.

2) In disks with a low amplitude (external) spiral potential but without self-gravity, our simulations show long lasting spiral patterns in the gas. We also obtain bifurcation features (arm branches) near locations of Lindblad and ultraharmonic resonances, similar to features discussed in CLS.

3) To assess the intrinsic stability of disks for growth of moderate-scale ($\sim$kpc scale) structure, we simulated self-gravitating disks without an external spiral potential. Slightly over-dense regions grow (nonlinearly) in density due to self-gravity, and subsequently be-

come stretched due to the rotational shear. For disks with a constant Toomre parameter Q (equivalently, with initial surface density distribution $\propto R^{-1}$) and thickness H, the instability initially grows in the outermost regions. Only the inner regions remain stable. For disks with a lower value of Q_0, the size of the inner stable region decreases, and the instabilities grow sooner. As the thickness of the disk decreases, so does the size of the inner stable region.

4) In self-gravitating disk models with an external spiral potential, interarm feather-like features can arise in two distinct ways. One way these features can develop is essentially the same as in models without spiral structure summarized in (3) above, i.e. via swing amplification in the interarm region. Stronger spiral potentials changes the spacing of these features only slightly. However, strong spiral potentials can lead to the growth of self-gravitating knots strung out like beads along the arms. Growing arm condensations in turn can produce interarm feathering in a second way, by concentrating gas as it flows from the arm into the interarm regions. If we define "true spurs" as distinct interarm features associated with the brightest regions in the arm, these structures only form in self-gravitating disks with strong ($F \approx 10\%$) external potentials.

5) Bound clumps that grow in the spiral arms have masses of $\sim 10^7$ $M_\odot$. The spacings of these clumps, or equivalently, spurs, are measured to be $\sim 3\lambda_{J,arm}$ - $5\lambda_{J,arm}$. In models where $Q_0 = 2$, the ratio of clump spacing to arm width is consistent with the prediction $\lambda/W \approx 3$ from Elmegreen (1994) and the observational study of Elmegreen & Elmegreen (1983). In many galaxies large clouds, such as GMAs and superclouds, are observed to have masses and spacings similar to the knots in our models.

6) We find that without magnetic fields, the arms in self-gravitating models rapidly fragment, destroying the continuous, distinct spiral arm shape. Thus, magnetic fields may be important for maintaining the integrity of grand design spiral structure in the ISM, even as self-gravity (and star formation) works to destroy these large-scale patterns.

7) The distribution and extent of interarm features that grow in self-gravitating models depend on the surface density distribution (or, equivalently, the instability parameter Q). For R^{-1} surface density distributions, for which Q is initially constant, strong feathering grows early on in the outer regions of the disk. At later times in the inner regions, spurs grow from the arm clumps and extend out to nearly the adjacent arm. For R^{-2} surface density distributions, Q increases with radius. For these disks, spur formation in the outer regions is suppressed, but prominent spurs still grow in the inner regions. Our models have adopted H = constant; if H increases with R, it is possible to have inner-disk instability and outer-disk stability even with Q = constant.

8) The orientation of the spurs with respect to the arms depends on the pattern speed of the spiral potential. Inside corotation, spurs extend outward from the convex side of the main dust lanes, as this is the downstream side of the arm. Outside corotation, the potential rotates faster than the gas, so the spurs form inside the main dust lanes. In principle, a reversal in the orientation of spurs in observed galaxies could be used to determine the position of the corotation radius.

Although we were able to produce spurs and quantify the conditions necessary for the growth of spurs with the models of this work, we were unable to follow the subsequent evolution of the disk for many orbits. Runaway growth of the massive clumps in the spiral arms causes the surrounding gas to have large velocities, which implies short time steps in order to satisfy the Courant condition. In addition, the densities become sufficiently large and the clumps so small that they are not well resolved by our grid. However, the physicality of the simulation itself can be questioned at late times, because real condensations would not grow uninhibited. The agglomeration of gas in galaxies into GMCs eventually leads to the formation of stars. The photoionization and mechanical inputs from H II regions and supernovae associated with massive star formation in GMCs return much of their gas to the diffuse phase. In future work, we plan to implement feedback mech-

anisms, using appropriate energy injection rates from typical star formation processes to disperse the clumps formed in the arms. We also plan to include heating and cooling processes to simulate a realistic multi-phase medium. By including processes of this kind, it will be possible to study the spur structure morphology and GMC formation rates and properties consistent with quasi-steady-state conditions.

Acknowledgments

We thank W. T. Kim and S. N. Vogel for stimulating discussions, and G. C. Gomez for his role in implementing cylindrical polar coordinates in ZEUS. We are also grateful to P. J. Teuben for assistance using NEMO software (Teuben 1995) for data analysis and visualizations. We thank B. G. Elmegreen for a helpful and insightful referee's report. This research is supported by the National Science Foundation under grants AST-0228974 and AST-0507315.

Chapter 4

Cloud Formation and Feedback in Disk Galaxies

Abstract

We include feedback in global hydrodynamic simulations in order to study the star formation properties in gaseous disks. In previous work, we studied the growth of clouds and spiral substructure due to gravitational instability. In order to further evolve those models, we implement feedback through the input of mechanical energy to disperse the cloud gas back into the surrounding ISM. For models with large supernovae momenta, colliding flows occur, and corresponding density enhancements also lead to cloud formation; on average, masses of clouds formed in this manner are lower than clouds formed in large scale sheared structures and spiral arms. In general, we find a relationship between the star formation rate density and the surface density consistent with a power law with index $\sim$2 for our models with the largest dynamic range. We suggest that the value of the exponent in numerical simulations (and likely in nature) may be dependent on the thickness of the disk. The overall star formation rates do not strongly depend on the rate or efficiency of star formation in dense gas (which are input parameters). The velocity dispersion is

primarily dependent on the input feedback momentum. We find that large feedback velocities, which contribute to high levels of large-scale turbulence, suppress star formation, due to the efficient destruction of dense clouds. Additionally, we find that the star formation rates are $\sim$2-3 times larger in models with an external spiral perturbation compared with models without one. With our simple feedback prescription, any global spiral pattern cannot be sustained; less correlated feedback and smaller scale turbulence may be required for any spiral pattern to persist.

4.1 Introduction

A crucial intermediary for the formation of stars in the ISM is the gaseous cloud. Stars form deep within Giant Molecular Clouds (GMCs), and GMCs themselves may be embedded in large atomic haloes, which are referred to as superclouds (Elmegreen & Elmegreen 1983). The dispersal of cloud gas, resulting from the ionizing radiation from newly born stars, stellar winds, and supernovae (SN), subsequently has an impact on the formation of the next generation of stars. Supernovae also play a significant role in maintaining and/or determining the phase of the ISM (McKee & Ostriker 1977; Norman & Ikeuchi 1989), and are thought to be the main source of turbulence, at least in most of the diffuse ISM , which has been invoked as the primary mechanism regulating star formation (e.g. Ballesteros-Paredes et al. 2007; Mac Low & Klessen 2004; McKee & Ostriker 2007). Consequently, the star formation process is directly associated with the formation, evolution, and destruction of the gaseous clouds.

The formation and growth of clouds is dependent on the gravitational stability of the diffuse gaseous environment. In disk galaxies, galactic rotation and thermal pressure, among other factors, act to oppose the growth of perturbations due to gravity. The Toomre Q parameter indicates the susceptibility of axisymmetric perturbations to grow in

uniform disks: for $Q < 1$, the surface density is sufficiently large for gas self-gravity to overwhelm the restoring effects of shear and pressure (Toomre 1964). Non-linear simulations have shown that for non-axisymmetric perturbations the threshold $Q \approx 1.5$ (Kim & Ostriker 2001, 2007; Kim et al. 2002; Li et al. 2005b). The observed cutoff in star formation activity at large radii supports the idea that stars form in gravitationally unstable regions with densities above a critical value (Kennicutt 1989; Martin & Kennicutt 2001). In general, magnetic fields cannot prevent but only slow the collapse of gas; however, in conjunction with other physical mechanisms, magnetic fields may enhance instability, as is the case when the magneto-rotational instability (MRI, Kim et al. 2003) is present, or via the magneto-Jeans instability (MJI, Kim et al. 2002). Potential sources for the perturbations are variations in the gravitational potential, such as the stellar spiral arms, as well as shocks due to supernovae.

The formation of stars within GMCs occurs soon after the clouds themselves form. The inception of star formation must occur soon after the gas accumulates to form the clouds, because almost all GMCs contain stars. Ionizing radiation from newly formed stars subsequently dissociates the molecules and even disperses the surrounding gas; some fraction of the gas may remain molecular, but in unbound clouds. The massive O and B stars reach the end of their lifetimes in $\sim$2 - 20 Myr; the cumulative effect of feedback from all the contiguously forming stars contribute to the short estimated GMC lifetimes of $\sim$20-30 Myr (e.g. Blitz et al. 2007). These feedback mechanisms drive turbulence. This turbulence could prevent the formation of stars in nearby regions, but could also potentially trigger collapse events resulting in the formation of stars elsewhere. Collisions between supernovae blast waves can result in sufficiently large densities for gas to collapse and form stars. Thus, feedback from stars that form in a cloud significantly affects the formation rate and efficiency of later star formation, as well as the evolution of the parent cloud itself, and, potentially, the larger scale ISM.

Despite the host of processes that impact the formation of stars, observations have shown a clear correlation between the star formation rate density and the gas surface density, with power-law forms $\Sigma_{SFR} \propto \Sigma_g^{\alpha}$, now known as the Kennicutt-Schmidt law (Kennicutt 1998b; Schmidt 1959), provided that the density is above the critical value. A power law with $\alpha \approx 1.3 - 1.4$ has been found to fit a range over four orders of magnitude in globally averaged surface densities (e.g. Heyer et al. 2004; Schuster et al. 2007); Kennicutt et al. (2007) recently studied the local $\Sigma_{SFR} - \Sigma$ relationship in M51, and found a similar power law relationship. Additionally, Bouche et al. (2007) found a universal Kennicutt-Schmidt law in their high-redshift study of galaxies out to z=2.5, with $\alpha \sim 1.7$. A second empirical law described by Kennicutt is $\Sigma_{SFR} \approx 0.1\Sigma_g/\tau_{dyn}$, where τ_{dyn} is the local orbital time of the gas.

Many theoretical studies have attempted to explain the observed relations between the star formation rate and the gas surface density. Simple analytic prescriptions can be obtained that depend on the star formation efficiency per cloud free-fall time or cloud lifetime, and yield consistency with power law scalings (McKee & Ostriker 2007). Using global 3D numerical simulations, including gas self-gravity and a prescription for star formation, Tasker & Bryan (2006) were able to reproduce the slope of the Kennicutt-Schmidt power law. Li et al. (2006), using SPH simulations, were also able to reproduce the slope and normalization. Their simulations included gravity and sink particles to track the collapsing gas, but did not treat feedback. Wada & Norman (2001) performed larger scale 2D simulations to investigate the gas dynamics and phase evolution of inner galactic disks, in models with and without feedback. They focused on the thermal distribution of the various gas components, as well as large scale turbulence. Wada & Norman (2007) extended their simulations to include 3D, mainly to test the relationship between the star formation rate and an ISM with log-normal density distribution, as described by Elmegreen (2002). They found that observed star formation rates can be reproduced if the

density distribution in the ISM is log-normal. In this work we investigate how supernovae driven feedback affects subsequent star formation in gas disks.

The evolution of large gas clouds is also relevant in studies of spiral structure. In previous work (Shetty & Ostriker 2006, hereafter Chapter 3) we simulated global disks with an external spiral potential, and found that gravitational instability causes gas in the spiral arms to collapse to form clouds with masses $\sim 10^7 M_\odot$, similar to masses of HI superclouds observed by Elmegreen & Elmegreen (1983) and large GMCs, known as Giant Molecular Associations (GMAs), found in M51 by Vogel et al. (1988). We found that gas self-gravity is also crucial for the growth of spurs (or feathers), which are interarm features that are connected to the spiral arm clouds (see also Kim & Ostriker 2002). Observations have shown that spurs are indeed ubiquitous in grand design galaxies, and are likely connected with large clouds in the spiral arms (Elmegreen 1980; La Vigne et al. 2006). If grand design spiral structure is long lasting, as hypothesized by density wave theory (Bertin & Lin 1996; Lin & Shu 1964, and references therein), then feedback mechanisms dispersing the spiral arm clouds must nevertheless leave the global spiral pattern intact. One of the goals of this work is to assess the effect of supernovae driven feedback in clouds on the global spiral morphology.

Conversely, the spiral arms also affect the initial formation of clouds, and therefore star formation. Observations show that most Hα emission in grand design galaxies occur downstream from the primary dust lanes. An explanation for these observations is that gas is compressed as it flows through the spiral potential minimum, leading to cloud formation; then at some later time stars form within these compressed gas clouds. This description of the observed offsets is still under debate, due to both observational limitations and opposing theoretical views on the star formation process. Further, the relative importance of spiral arm triggering is still not completely understood. Vogel et al. (1988) found that the star formation efficiency (in molecular gas) in the grand design galaxy M51

is only larger by a factor of a few compared with a galaxy without a strong density wave. Other observational studies found similar results (see Kennicutt 1998a, and references therein). As a result, density waves may only gather gas to form clouds in the spiral arms, but may not affect the star formation efficiency within these clouds. Without a large-scale density wave, a similar fraction of gas might still collapse (per galactic orbit) to form clouds via other mechanisms (including large-scale gravitational instabilities), but not in a coherent fashion. Here, we explore the differences in cloud formation properties in gaseous disks with and without an external spiral driving mechanism.

In this work we are interested in the effect of feedback from star formation in large clouds, such as GMAs, on the star formation rate, as well as the overall dynamics and subsequent cloud formation in galaxy disks. This work extends the models presented in Chapter 3: numerical hydrodynamic simulations of global disks with gas self-gravity. With the resolutions of our models, massive GMAs do not fragment into smaller GMCs, so significant energy input is required to unbind the gas in these concentrations. If this energy is provided by star formation feedback, multiple massive stars would be needed to destroy the GMAs. We model feedback by considering the destruction of the large clouds by single energetic events. In practice, this could represent multiple correlated supernovae; this can also be considered simply as an expedient but cleanly parameterizable feedback model. We then study the resulting nature of the turbulent gaseous disk, as well as the formation and evolution of the clouds that form in the turbulent medium. In the next section, we describe our numerical simulation, including model parameters and the feedback algorithm. We then present and analyze our simulation results in §4.3. In §4.4 we summarize our results after a discussion.

4.2 Modeling Method

4.2.1 Basic Hydrodynamic Equations

To study the growth of clouds in a gaseous disk, we simulate the evolution of the gaseous component by integrating the equations of hydrodynamics. As in Chapter 3, we include the gravitational potential of the gas. The governing hydrodynamic equations, including self-gravity, are:

$$\frac{\partial \Sigma}{\partial t} + \nabla \cdot (\Sigma \mathbf{v}) = 0, \tag{4.1}$$

$$\frac{\partial \mathbf{v}}{\partial t} + \mathbf{v} \cdot \nabla \mathbf{v} + \frac{1}{\Sigma} \nabla p = -\nabla(\Phi_{ext} + \Phi), \tag{4.2}$$

$$\nabla^2 \Phi = 4\pi G \delta(z) \Sigma. \tag{4.3}$$

Here, Σ, $\mathbf{v}$, and p are the gas surface density, vertically averaged velocity, and vertically integrated pressure, respectively. The semi-thickness of the disk is H, such that $\Sigma/2H$ is the mid-plane density ρ_0. For our models, we assume an isothermal equation of state, so that $p = c_s^2 \Sigma$, where c_s is the sound speed. The term Φ is the gaseous self-gravitational potential. To grow gaseous spiral arms, we include an external spiral potential Φ_{ext} to model the perturbation produced by the non-axisymmetric stellar distribution, which is specified at time t in the inertial frame, by

$$\Phi_{ext}(R, \phi; t) = \Phi_{ext,0} \cos[m\phi - \phi_0(R) - m\Omega_p t] \tag{4.4}$$

where m, $\phi_0(R)$, and Ω_p are the number of arms, reference phase angle, and spiral pattern speed, respectively. We only consider models with a constant pitch angle i, so that

$$\phi_0(r) = -\frac{m}{\tan i} \ln(R) + constant. \tag{4.5}$$

4.2.2 Model Parameters

Similar to work presented in Chapter 3, the sound speed c_s and rotational velocity v_c are constant in space and time, $c_s = 7$ km s^{-1}, and v_c = 210 km s^{-1}. We adopt the code unit of length $L_0 = 1$ kpc. Using c_s as the code unit for velocity, the time unit $t_0 = L_0/c_s = 1.4 \times 10^8$ years, which corresponds to one orbit $t_{orb} = 2\pi/\Omega_0$ at a fiducial radius $R_0 = L_0 v_c/2\pi c_s = 4.77$ kpc. Our results will scale to other values of R_0 and L_0 with the same ratio, as well as models with the same ratio $v_c/c_s = 30$.

In Chapter 3, we explored different external spiral potential strengths,

$$F \equiv \frac{\Phi_{ext,0} m}{v_c^2 \tan i} \tag{4.6}$$

which is the ratio of the maximum radial perturbation force to the radial force responsible for a constant rotational velocity v_c. We found that spurs form in disks with strong external potential strengths. Since one of our objectives is to assess the evolution of the spurs in disks including feedback, here we only simulate disks with F = 10%, for both 2 arm and 4 arm spiral galaxies (m=2 and m=4). The pattern speed for spiral models is 8.4 km s^{-1} kpc^{-1}, corresponding to a corotation radius of 25 kpc. We also simulate disks with no external spiral forcing.

In our computation of gas self-gravity, we include the effect of the thickness of the disk, which also acts as softening. We assume a Gaussian vertical gas distribution, with $H \propto R$, so the disk flares at larger radii (see §A.4). As described in Chapter 3 and Kim & Ostriker (2007), including the effect of thickness stabilizes the disk. For most of our simulations, we use H/R = 0.01.

As in Chapter 3, the Toomre parameter $Q_0 \equiv \frac{\kappa_0 c_s}{\pi G \Sigma_0}$ and the surface density Σ at R_0 are related by:

$$\Sigma_0 = \frac{32}{Q_0} \mathrm{M}_\odot \,\mathrm{pc}^{-2} \left(\frac{c_s}{7\,\mathrm{km\,s^{-1}}} \right) \left(\frac{\kappa_0}{62\,\mathrm{km\,s^{-1}\,kpc^{-1}}} \right). \tag{4.7}$$

For flat rotation curves, the epicyclic frequency $\kappa = \sqrt{2}\Omega = \sqrt{2}v_c/R$. Our models initially have $\Sigma \propto R^{-1}$, so that Q is constant for the whole disk.

4.2.3 Numerical Methods

Since this work is an extension of previous work, we refer the reader to Chapter 3 for a description of the cylindrical-symmetry version of the ZEUS code (Stone & Norman 1992a,b) that we use to carry out our simulations. We use a parallelized version of the hydrodynamic code and gravitational potential solver, allowing us to increase the number of zones in the grid relative to the models of Chapter 3. For our standard grid we limit the azimuthal range from 0 - $\pi/2$ radians and the radial range from 4 - 11 kpc. We implement outflow and periodic boundary conditions in the radial and azimuthal directions, respectively. These models have 1024 radial and 1024 azimuthal zones. Since the radial grid spacing is logarithmic, the resolution varies: the linear resolution in each dimension (ΔR, $R\Delta\phi$) varies from $\sim$(4 pc, 6 pc) in the innermost region to $\sim$(11 pc, 17 pc) at the outer boundary. These high resolutions allow the Truelove criterion (Truelove et al. 1997) to be satisfied throughout the simulation as gas collapses to form self gravitating clumps.

In this work we use a different method to compute the gravitational potential compared with the approach presented in Chapter 3. Here, we use a method derived from that described by Kalnajs (1971) in polar coordinates (see also Binney & Tremaine 1987). This method employs the convolution theorem for a disk decomposed into logarithmic spiral arcs. We implement softening to account for the non-zero thickness of the disk. We describe the method in detail in the Appendix (§A.4).

We note that for simulations with the standard grid and including a spiral potential, the limit in azimuth requires that m=4 (4 arms). However, we also explore some models with m=2 patterns, with the azimuthal range 0 - $\pi/2$, using higher resolution than the standard grid.

4.2.4 Feedback: Event Description and Algorithm

Equations (4.1)-(4.3) only describe the flow as gas responds to self gravity, and to the external spiral perturbation, if one is present. However, those equations do not describe any feedback that would occur after a self-gravitating cloud forms and fragments into smaller-scale structures, ultimately forming stars with a range of masses. In the real ISM of galaxies, clouds are dispersed by the combination of photo-evaporation by UV radiation from massive stars, and the "mechanical" destruction by expanding HII regions and supernovae.

We include in our simulations a very simple feedback prescription by implementing "feedback events," each representing momentum input from a number of supernovae (or, alternatively, multiple overlapping expanding HII regions). The supernova rate, R_{SN}, averaged over all mass M_{dense} above a chosen threshold density in a galaxy is

$$R_{SN} = \frac{Number\,of\,Supernovae}{M_{dense}\,time}. \tag{4.8}$$

When this rate is applied to an individual cloud of mass M_{cl} with a lifetime t_{cl}, the average number of supernovae in a cloud will be

$$N_{SN} = R_{SN} \cdot M_{cl} \cdot t_{cl}. \tag{4.9}$$

If the total mass of stars of all masses formed per single supernova is M_{SN}, and the star formation efficiency over a cloud lifetime is ε_{SF}, then

$$N_{SN} = \varepsilon_{SF} \frac{M_{cl}}{M_{SN}}. \tag{4.10}$$

Equating expressions (4.9) and (4.10), the mean cloud lifetime is

$$t_{cl} = \frac{\varepsilon_{SF}}{R_{SN} M_{SN}}. \tag{4.11}$$

In a given time interval δt, such as the time between successive computations in the numerical evolution, the probability P that a cloud (of lifetime t_{cl}) is destroyed is $\delta t / t_{cl}$.

Thus,

$$P = \delta t \cdot R_{SN} M_{SN} / \varepsilon_{SF} \tag{4.12}$$

In our algorithm, clouds are defined as regions above a chosen density threshold with a prescribed bounding radius. If a particular zone is a local density maximum, that zone is selected as the center of the cloud. For any such identified cloud, a star formation event is initiated with a probability per time step given by equation (4.12). In each cloud that is determined to undergo feedback, gas is evenly spread out in a circular region with the predetermined radius. Gas in each zone in the circular region is assigned an outward velocity (relative to the cloud center) to expand the feedback "bubble." A constant velocity is also added such that total angular momentum is conserved. The velocity profile inside the bubble is proportional to the distance from the bubble center. For most of our simulations, we choose a radius of the feedback bubble to be 75 pc, which corresponds to 12-23 pixels, depending on the radial location. In this way, the initially collapsing cloud gas is forced back into the surrounding ISM.

In our simulation, we only consider the isothermal expansion of the clouds, since we assume an isothermal equation of state. Thus, we can only consider the net energy input at a stage when expansion of the shell has become strongly radiative. Numerical simulations show that for a single SN of energy $E_{SN} \approx 10^{51}$ ergs, the momentum during the radiative stage is $P_{rad} \approx 3 \times 10^5$ $M_\odot$ km s^{-1}(Chevalier 1974; Cioffi et al. 1988). During the subsequent evolution of the bubble, the shell momentum P_{sh} is conserved, and is equal to P_{rad}.

For a total number of massive stars formed given by equation (4.10), and assuming correlation in time, the total momentum applied to the shell is

$$P_{sh} = N_{SN} P_{rad} = \varepsilon_{SF} \frac{M_{cl}}{M_{SN}} P_{rad} \tag{4.13}$$

The shell velocity V_{sh} is

$$V_{sh} = P_{sh}/M_{sh} = \varepsilon_{SF} \frac{M_{cl}}{M_{SN}} \frac{P_{rad}}{M_{sh}}. \tag{4.14}$$

Assuming M_{SN} = 200 $M_\odot$ and $\varepsilon_{SF} = 0.1$, for $P_{rad} = 3 \times 10^5$ $M_\odot$ km s^{-1}, V_{sh} = 150 $\times (M_{cl}/M_{sh})$ km s^{-1}.

Given our feedback prescription, the two key parameters are the probability per unit time for cloud destruction (eq. [4.12]), and the momentum input in the feedback event (eq. [4.13]). For the simulations presented here, we explore a range in the rate R_{SN} and the momentum of one supernova P_{rad}. The specific supernova rate is set either to $R_{SN} = (10^9\ M_\odot \times 50\ \mathrm{yr})^{-1}$ (comparable to that in the Milky Way), or ten times that rate. Since M_{SN}/ε_{SF} in equation (4.12) appears as its inverse in equation (4.13), we fix $M_{SN} = 200\ M_\odot$ for all simulations, and explore variations in ε_{SF}. The momentum P_{rad} is set either to 3.4×10^4 or 3.4×10^5 $M_\odot$ km s^{-1}, in order to allow for out-of-plane momentum losses and a range in E_{SN}. To implement the chosen value of P_{rad}, we set the velocity $V_{inp} \equiv P_{rad}/(400\ M_\odot)$, corresponding to 85 or 850 km s^{-1}.

Before any feedback, the spiral models are executed for some time to allow gas to collapse (due to self gravity) and form the clouds in spiral arms. In simulations without spiral forcing, condensations begin to grow due to an initial 0.1% density perturbation. As a result of shear, the first structures that form are large scale flocculent spiral-like features, which we termed "sheared background features" in Chapter 3. Gas in these features then collapse to form distinct clouds. Thus, we wait until some threshold density is reached before feedback occurs. For most models, the threshold density is $\Sigma/\Sigma_0 = 10$ (320 $M_\odot$ pc^{-2} for Q_0=1 and 160 $M_\odot$ pc^{-2} for Q_0=2).

4.3 Simulation Results

We first present simulations with standard grid parameters, without spiral structure. We then show results of simulations including spiral structure, as well as simulations pertaining to different radial regions.

Table 4.1 shows the initial conditions of the models we present, as well as the relevant parameters controlling the feedback events. Column (1) lists each model. Column (2) shows the initial Toomre Q parameter which is initially constant for the whole disk. Column (3) indicates the number of arms, all with F=10%. Column (4) gives the supernova rate, which is required for setting the probability that a feedback event occurs in a cloud (see eq. [4.12]). Column (5) shows the assumed star formation efficiency, and column (6) gives the supernova shell velocity parameter. For these models $H/R = 0.01$.

4.3.1 Disks without Spiral Structure

Figure 4.1 shows a snapshot of model with Q_0=1, at time t/t_{orb} = 0.84, without an external spiral potential and before any feedback. As discussed in §4.2.4, trailing features grow due to the shear in the disk (see Chapter 3 for details). The most dense structures grow as sheared, trailing features. It is in these regions where the first supernovae will occur to disperse the dense gas.

Figure 4.2 shows a snapshot of model Q1A, at time t/t_{orb} = 1.125. For model Q1A, the supernovae parameters are all at the low end of the range. At the time of this snapshot, 105 feedback events have occurred, in clouds which have mean $M_{cl} = 1.2 \times 10^6$ $M_\odot$. The main difference between Figures 4.2 and 4.1 is the shape of the trailing features. The feedback events have caused the features to become fragmented. However, dispersal of gas due to feedback was not sufficient to prevent or reverse the inflow of gas into the high density agglomerations. Either the supernovae do not occur rapidly enough, or do not

Table 4.1. Parameters for Standard[a] Models

Model (1)	Q_0 (2)	m (3)	R_{SN}[b] (4)	ε_{SF} (5)	V_{inp} (km s^{-1}) (6)
Q1A	1	0	1	0.05	85
Q1B	1	0	1	0.1	85
Q1C	1	0	1	0.1	850
Q1D	1	0	10	0.1	850
Q1SA	1	4	1	0.05	85
Q1SB	1	4	1	0.1	85
Q1SC	1	4	1	0.1	850
Q1SD	1	4	10	0.1	850
Q1SE	1	4	10	0.1	85
Q2SA	2	4	1	0.05	85
Q2SB	2	4	1	0.1	85
Q2SC	2	4	1	0.1	850
Q2SD	2	4	10	0.1	850

[a] 1024×1024 zones; R $\in$ 4-11 kpc; $\phi \in 0$-$\frac{\pi}{2}$ radians

[b] Number of supernovae per 50 years per $10^9 M_\odot$

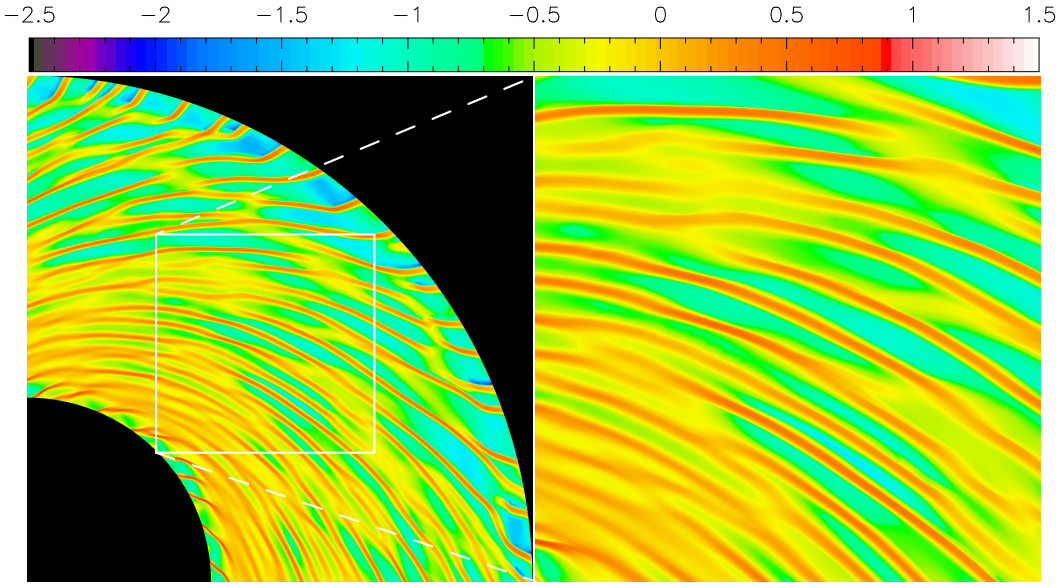

Figure 4.1: Density snapshots of $Q_0 = 1$ before any feedback, at time t/t_{orb} = 0.84. The color scale is in units of $\log(\Sigma/\Sigma_0)$.

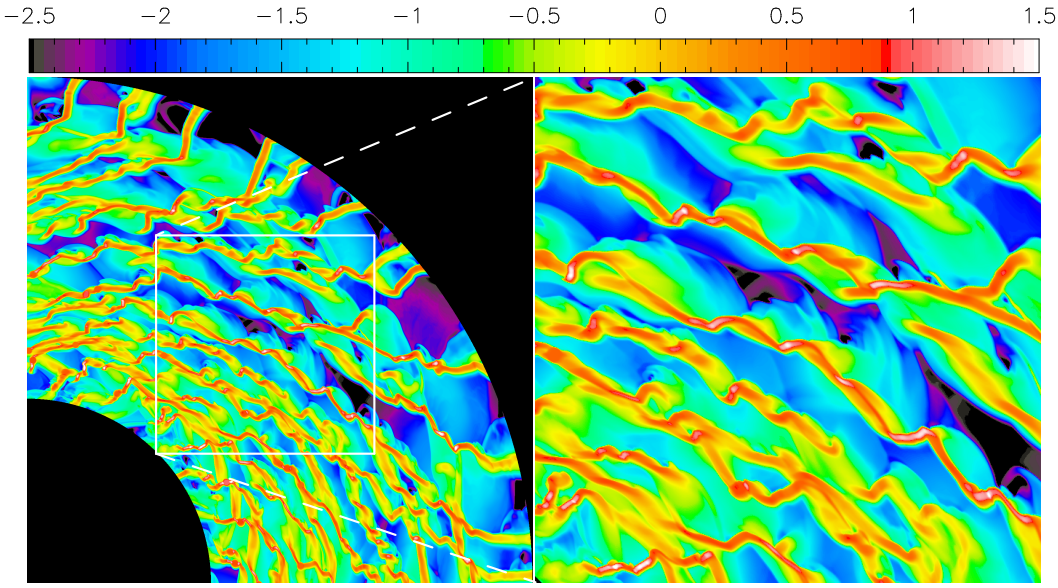

Figure 4.2: Density snapshots of model Q1A, at time t/t_{orb} = 1.125. The color scale is in units of $\log(\Sigma/\Sigma_0)$.

have enough momentum.

Even increasing both the supernovae rate by a factor of 10, and doubling the star formation efficiency is insufficient; the gravity from the trailing features keeps much of the gas in those structures. Increasing the velocity by up to a factor of 8 still does not significantly affect the outcome: much of the gas is contained in the sheared structures at any given time.

It is only when V_{inp} is increased to 850 km s^{-1}, along with $R_{SN} = 10$ and $\varepsilon_{SF} = 0.1$, as in Model Q1D, that we find a significant difference, as shown in Figures 4.3-4.4. The velocity is sufficiently large to drive gas away from the density maxima of the trailing structures. Further, the rate is high enough that a large number of events occur to significantly alter the morphology, in comparison with Figure 4.2. Feedback events in this model are so frequent and energetic that collisions between bubbles occur. In some instances, such collisions create density enhancements that later result in more collapse and subsequent feedback along the bubble interface. At time t/t_{orb} = 1.125 (Fig. 4.3), we can still make out the underlying loci of the initial structures formed by

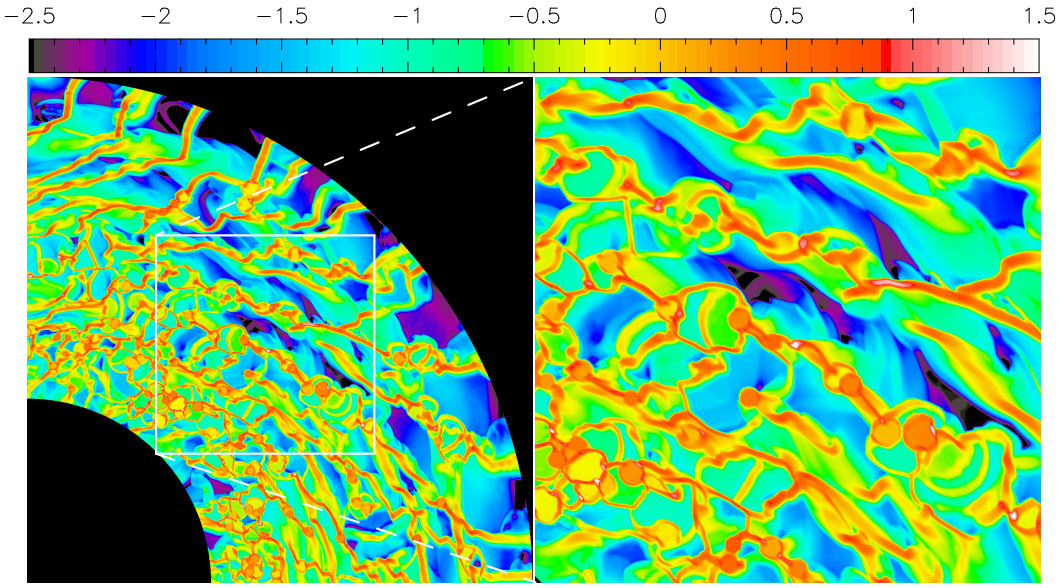

Figure 4.3: Density snapshots of model Q1D, at time t/t_{orb} = 1.125. The color scale is in units of $\log(\Sigma/\Sigma_0)$.

gravitational instability and shear, though 537 feedback events have occurred up to this time. Yet, after an additional 26 Myr and 75 feedback events (Fig. 4.4) the dominant large scale features do not have a single pitch angle. Further, the locations of many of the bubbles are clustered. Though gas is driven away from the initial structures formed before feedback, at later times clouds form in clusters near the initial density maxima, and where feedback bubbles overlap. Qualitatively, the features in the disk, consisting of filaments and bubbles, are similar to the global models including feedback of Wada & Norman (2001). We discuss the masses of the clouds in the next section (§4.3.2), along with cloud masses in simulations with an external spiral potential.

In disks with $Q_0 = 2$, sheared features will also grow, but need more time to develop than in the $Q_0 = 1$ disks. Due to its stability, after $t/t_{orb} = 2$ only a few clouds have formed. As a result, implementing feedback does not affect the majority of the disk. To study the effect of feedback in $Q_0 = 2$ disks, another mechanism is necessary to grow clouds everywhere in the disk. We thus simulate Q_0=2 disks with an external spiral potential, and then implement feedback to destroy the spiral arm clouds that grow.

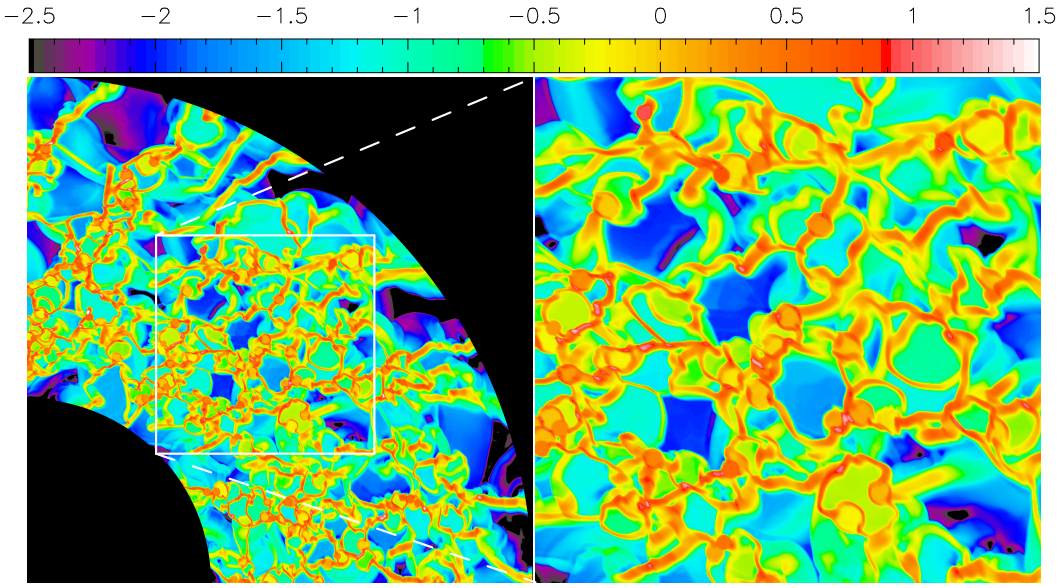

Figure 4.4: Density snapshots of model Q1D, at time t/t_{orb} = 1.375. The color scale is in units of $\log(\Sigma/\Sigma_0)$.

4.3.2 Disks with Spiral Structure

In disks with spiral structure, the stellar spiral potential acts as a source of perturbation, compressing the gas, eventually leading to the growth of self gravitating clouds. We explore the effect of feedback on the morphology of the gaseous spiral arms and interarm spurs, as well as any subsequent cloud formation.

Figures 4.5-4.6 shows snapshots of models with $m = 4$, for $Q_0 = 1$ and $Q_0 = 2$, without any feedback. In the spiral models, the growth of spiral arm clouds occur sooner than clouds formed by natural instabilities in a rotating self-gravitating disk. Figure 4.5-4.6 shows snapshots of models without any feedback, though in the $Q = 1$ snapshot (Fig. 4.5) the densities have surpassed the threshold density $\Sigma/\Sigma_0 = 10$ chosen for models with feedback.

For both models Q1SA and Q2SA, the supernova momenta are insufficient to offset the growth of clouds and spurs resulting from the spiral potential. After a feedback event, the dispersed cloud gas flows back toward the spiral arm. As a result, over time clouds

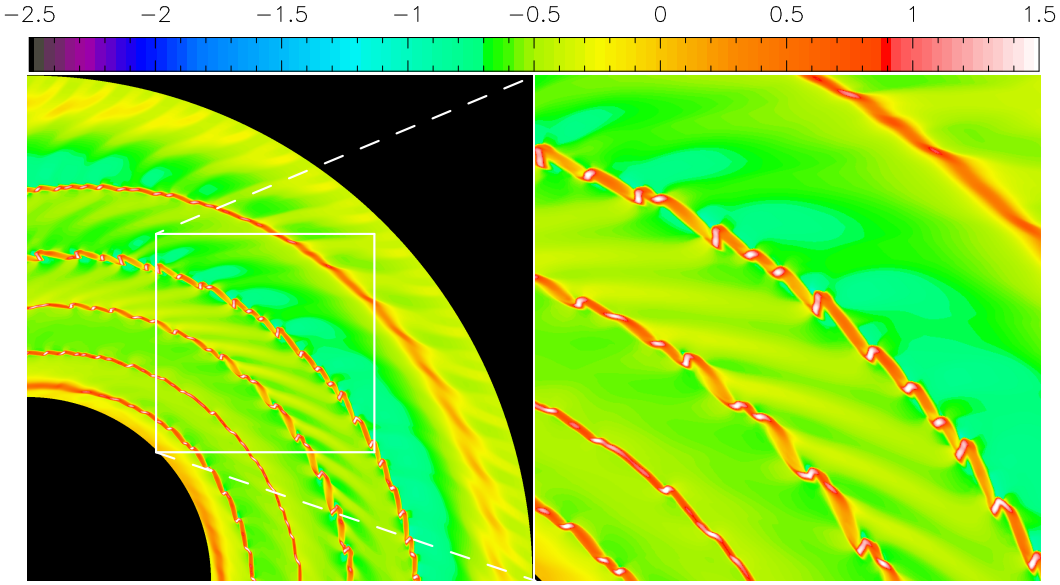

Figure 4.5: $Q_0 = 1$ spiral model, without feedback, at $t/t_{orb} = 0.675$. The color scale is in units of $\log(\Sigma/\Sigma_0)$.

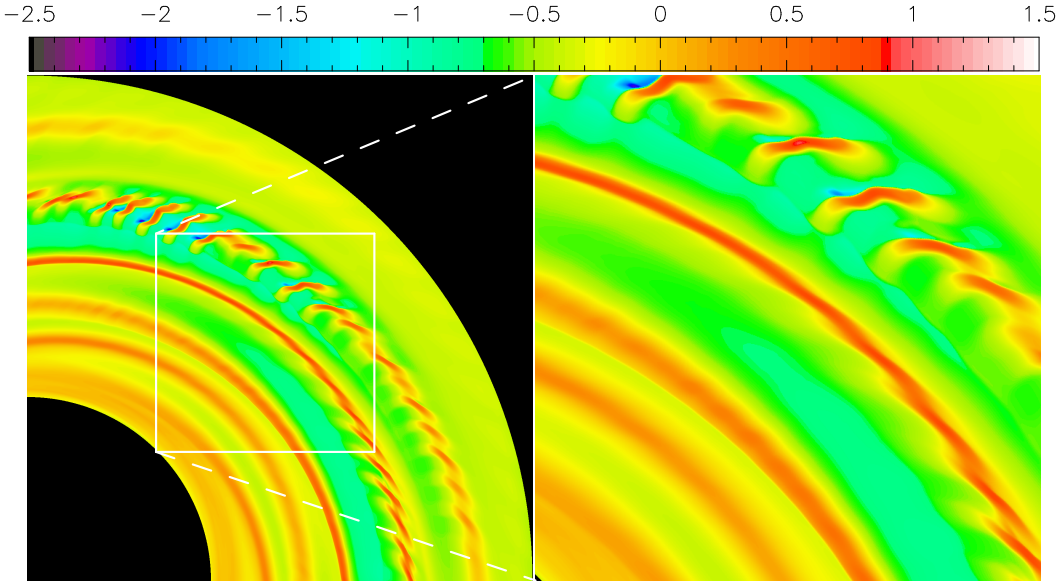

Figure 4.6: $Q_0 = 2$ spiral model, without feedback, at $t/t_{orb} = 1.04$. The color scale is in units of $\log(\Sigma/\Sigma_0)$.

that initially form continue to grow. Further, the spurs also continue to grow in density. Without feedback, self-gravitating spiral arm clouds cause the surrounding gas to flow in with large velocities. Eventually, the simulations have to be stopped because the Courant time is too small. The time when the simulation ceases, depending partly on our choice of the minimum acceptable Courant time, also depends on which clouds are (randomly) selected for feedback; clouds that have produced large inflow velocities would have to be dispersed for the simulation to continue to evolve.

We again find that large supernovae momenta are required to sufficiently disperse clouds so that immediate re-collapse does not occur. For such models, the supernovae rate has an effect on the number of subsequent clumps formed. Figure 4.7 shows a snapshot of models Q1SC and Q1SD, ~ 21 Myr after the first feedback events. At this time, 53 feedback events have occurred in model Q1SC, and 540 in model Q1SD. In model Q1SC, it is clear that most, if not all, feedback events originated in the spiral arms. However, in model Q1SD, many feedback events have occurred in interarm regions. The spiral arms are not as identifiable, though at this time the remnants of spurs are still identifiable. Further, model Q1SD contains many more clumps than model Q1SC. The enhanced supernovae rate has caused the collision of more shell remnants, which lead to formation of self gravitating clumps at the interfaces.

Figure 4.8 shows the histogram of the masses of the clouds M_{cl} that hosted feedback events in models Q1A, Q1D, Q1SA and Q1SD. In model Q1A, most feedback events have occurred in the large scale sheared features that grow due to gravitational instability. However, in model Q1D, some fraction of the feedback events have occurred in regions of colliding flows. The histogram suggests that clouds formed in such regions are likely to have lower masses than those formed in the large scale sheared features.[1] Similarly, in

[1]From equation (4.10), feedback events in model Q1A and Q1D on average consist of 300 and 350 supernovae, respectively.

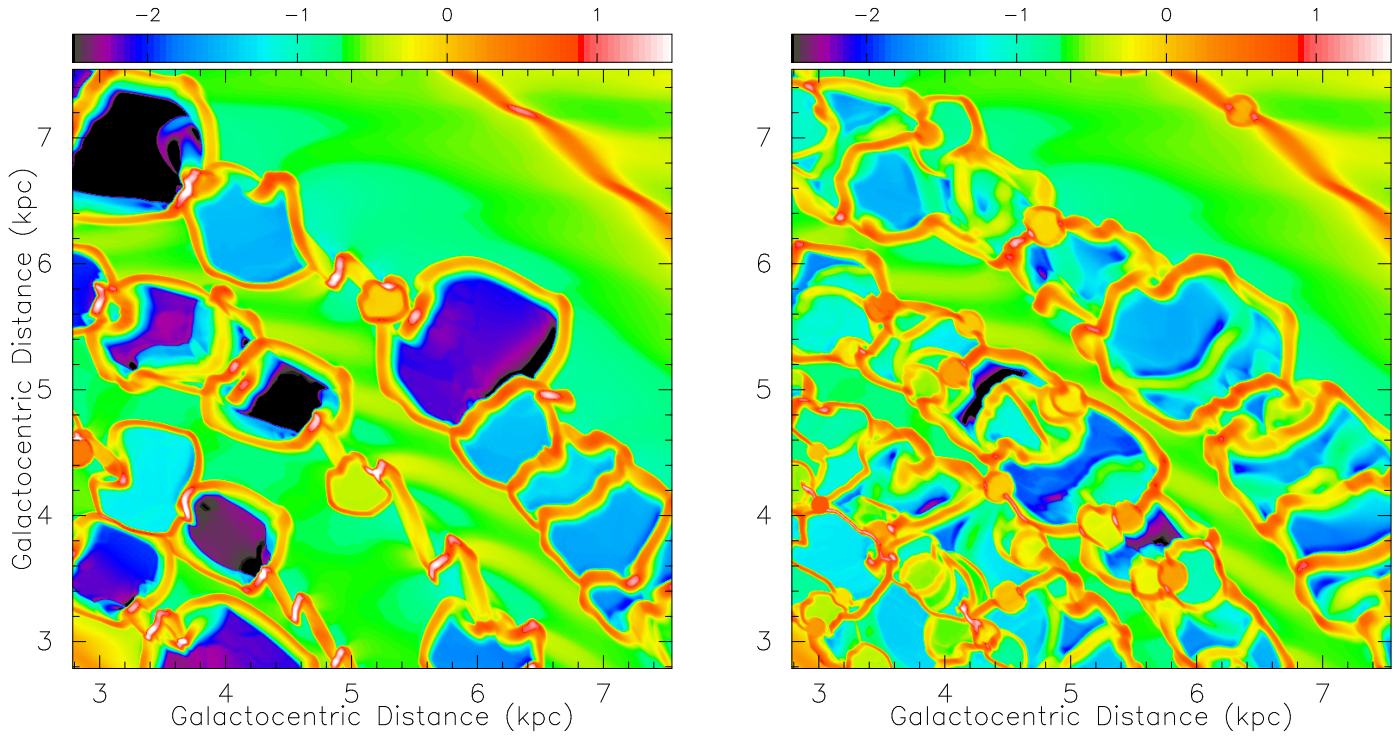

Figure 4.7: Models Q1SC (left) and Q1SD (right) at $t/t_{orb} = 0.73$ (left). The color scales are in units of $\log(\Sigma/\Sigma_0)$.

model Q1SA, most feedback events have occurred in the spiral arms, since most clouds form in the arms. On average, the clouds in model Q1SD have lower masses, because many clouds form away from the high density spiral arms, where colliding flows occur due to earlier feedback events. A detailed analysis is not appropriate here because many of the lower mass clouds are not well resolved. Higher resolution simulations are required to accurately measure cloud mass distributions. Nevertheless, it is clear that the characteristic masses of clouds formed in the sheared features or spiral arms are larger than those formed in colliding flows.

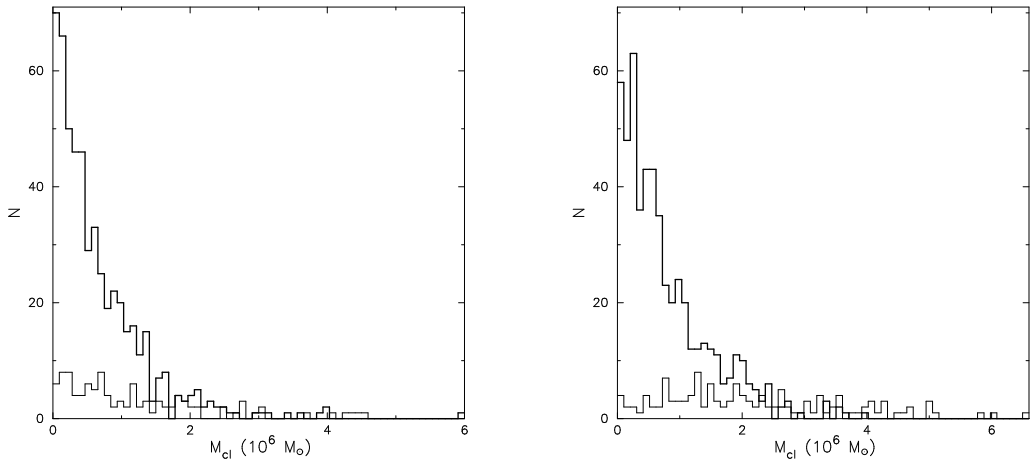

Figure 4.8: Left: Histogram of M_{cl} in models Q1D (thick) and Q1A (thin), up until time t/t_{orb} = 1.125 (see Figs. 4.2 - 4.3). The mean (median) M_{cl} for models Q1A and Q1D are 1.2×10^6 (0.8×10^6) and 0.7×10^6 (0.5×10^6) $M_\odot$, respectively. Right: Histogram of M_{cl} in models Q1SD (thick) and Q1SA (thin), up until time t/t_{orb} = 0.73 (model Q1SD is shown in Fig. 4.7). The mean (median) M_{cl} for models Q1SA and Q1SD are 2.2×10^6 (1.9×10^6) and 0.8×10^6 (0.6×10^6) $M_\odot$, respectively.

4.3.3 Star Formation Properties

Star Formation Rates and Turbulence

For comparison to observations, two quantities of interest are the star formation rate SFR and the turbulent velocity v_{turb}. In each simulation, we record each feedback event to determine the SFR. For some chosen time bin Δt, we compute

$$SFR = \varepsilon_{SF}\frac{\sum M_{cl}}{\Delta t}, \tag{4.15}$$

where $\sum M_{cl}$ is the total mass of all gas in clumps (i.e. above the chosen threshold surface density) that have undergone feedback events in the chosen time interval. We define

the turbulent velocity as the RMS sum of any non-circular velocities, weighted by the corresponding density:

$$v_{turb} = \left(\frac{\sum (\delta \mathbf{v}_{i,j})^2 \Sigma_{i,j}}{\sum \Sigma_{i,j}} \right)^{\frac{1}{2}}, \tag{4.16}$$

where only non-circular velocity components are considered: $\delta \mathbf{v} = \mathbf{v} - v_c \hat{\phi}$. Figure 4.9 shows the star formation rate and turbulent velocity as a function of time, for the Q_0=1 models without spiral structure. The time bin Δt for our SFR calculation is 3 Myr. In these models, the first feedback events occur at time $\sim$125 Myr. However, for the first $\sim$25 Myr after feedback begins, the SFR for all models is only a few $M_\odot$ yr^{-1}. Only $\sim$25 Myr after the first feedback events does the SFR substantially increase. Further, the model with large feedback momenta ($V_{inp} = 850$ km s^{-1}) and SN rate has the SFR increase to $>$10 $M_\odot$ yr^{-1}. This occurs because with such large velocities adjacent shells collide and more clouds are formed in the interfaces, which may subsequently undergo star formation.

The bottom panel of Figure 4.9 shows v_{turb}, for all feedback models without spiral structure and a simulation without any feedback. For the later case, we just allow self-gravity to grow clouds indefinitely. Most models continue the trend of v_{turb} established by the no-feedback case. In a few instances of enhanced feedback, there is a corresponding jump in v_{turb}. The enhanced SFR at later times for the model with large supernovae momenta also have increased levels of v_{turb}.

Figures 4.10 and 4.11 show the SFR and v_{turb} for the spiral models with $Q_0 = 1$ and $Q_0 = 2$. Comparing Figures 4.10 (with spiral structure) and 4.9 (w/o spiral structure), the star formation rate is consistent to within a factor of 2, although slightly larger in the spiral models. The general trends from the models without spiral structure are reproduced in Figures 4.10 and 4.11. Earlier times are shown in Figure 4.10, since the spiral arms cause gas to collapse into clouds sooner. It is clear that only in models with large supernovae shell velocities do the turbulent velocities increase appreciably; otherwise, the turbulent

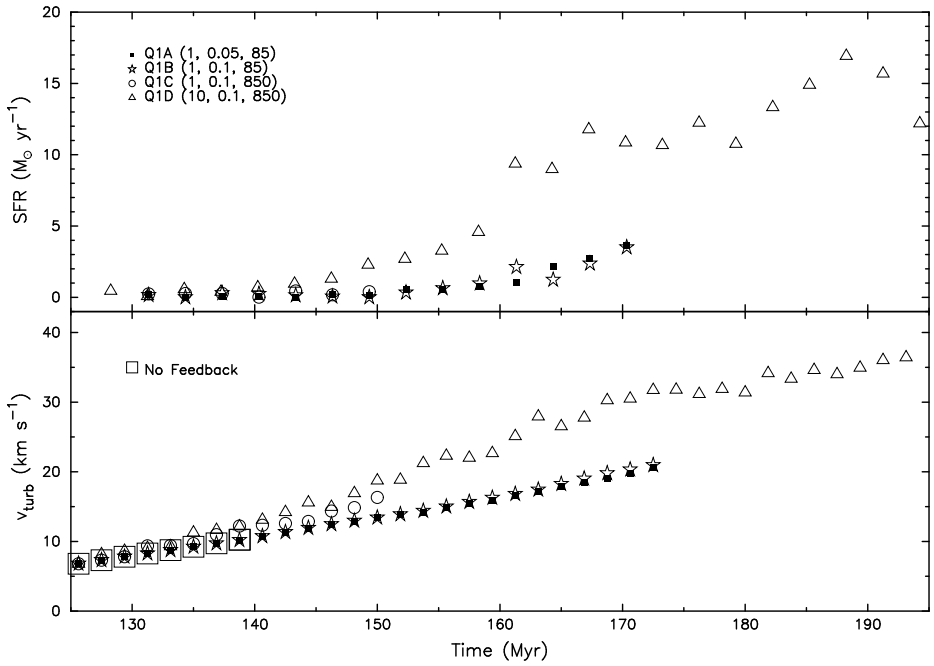

Figure 4.9: *SFR* (top) and v_{turb} (bottom) for models with Q_0=1, without spiral structure. The values in parentheses in the legend are the supernovae rate parameter R_{SN}, the star formation efficiency ε_{SF}, and shell velocity parameter V_{inp} of each model. The large open squares in the bottom panel is the turbulent velocity for a simulation without any feedback.

velocity (as we have defined it) is dominated by effects from gas self-gravity.

Model Q1SE, which has the same R_{SN} as model Q1SD, but a lower V_{inp} (85 km s^{-1}), results in a higher *SFR*, but lower v_{turb}. At later times the *SFR* is about a factor of 10 greater than the SFR of MODEL Q1SB, corresponding to the difference between the chosen value of R_{SN} for the respective models. The reason why the turbulent velocities of model Q1SE are low is because feedback events do not have sufficient velocities to affect regions that are far from the host clouds; feedback only slightly expands the clouds, which subsequently resume their collapse.

Since turbulence affects the velocity dispersion σ, a common assumption is that the sound speed c_s can be replaced by

$$c_{eff}^2 = c_s^2 + \sigma^2 \tag{4.17}$$

in the dispersion relations that characterize stability, such as the Jeans time, as well as

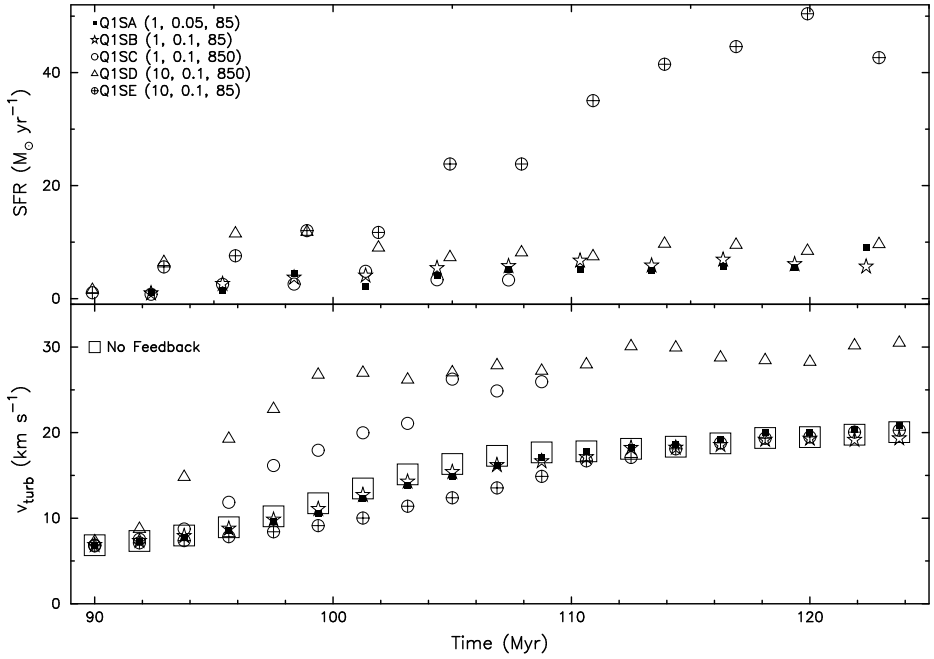

Figure 4.10: *SFR* (top) and v_{turb} (bottom) for models with Q_0=1, as in Figure 4.9, but with spiral structure.

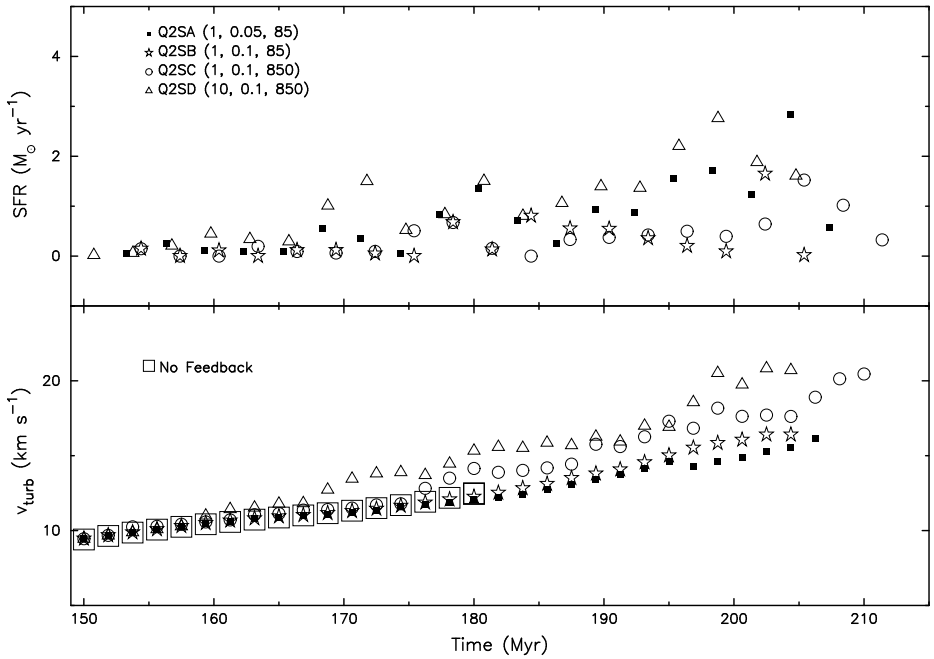

Figure 4.11: *SFR* (top) and v_{turb} (bottom), as in Figure 4.10, but for models with Q_0=2, with spiral structure.

other quantities such as the Jeans Mass and Q. We show the relationship between the velocity dispersion and the surface density in Figure 4.12. It is clear that the dispersion is related to the chosen value of V_{inp}. Naively, one may expect that $SFR \propto R_{SN}\Sigma/c_{eff}$. Model Q1SE has the same chosen parameters as model Q1SB, except R_{SN} is 10 times larger, and produces a SFR that is ≈10 times larger (Fig. 4.10), suggesting that the SFR is indeed directly proportional to R_{SN}. Comparing models with all the same parameters except for V_{inp}, Q1SD (V_{inp} = 850 km s^{-1}) with Q1SE (V_{inp} = 85 km s^{-1}), the SFR is indeed lower in model Q1SD. A possible reason for the lower SFR in model Q1SD, besides turbulent suppression, is because the large feedback velocity is efficient in destroying the dense clouds. In model Q1SE a feedback event only slightly expands the clouds, and the cloud subsequently resumes collapse. Thus star formation continues in clouds that have undergone feedback. On the other hand, clouds in model Q1SD are completely destroyed after a single feedback event, so star formation ceases. The suppressed star formation in models with large feedback velocities, may be due to large scale turbulence, or efficient destruction of the dense clouds.

Figure 4.13 shows the turbulent power spectrum (power $\propto v^2$) of model Q1D. The power is shown at constant k_R and k_ϕ. The slopes of the power spectra range from -2 to -3. For models that evolve for significant amounts of time, such as model Q1D, the power spectra are relatively independent of time. These results are consistent with turbulence dominated by numerous shocks, or Burgers turbulence.

Kennicutt-Schmidt Law

Figure 4.14 shows the local star formation rate per area as a function of mean surface density. To obtain these points, simulation data were binned in radius and time, of widths 1 kpc and 19 Myr, respectively. Only models with a sufficient number of points, which is dependent to some degree on the number of feedback events, are shown. Best fit lines to

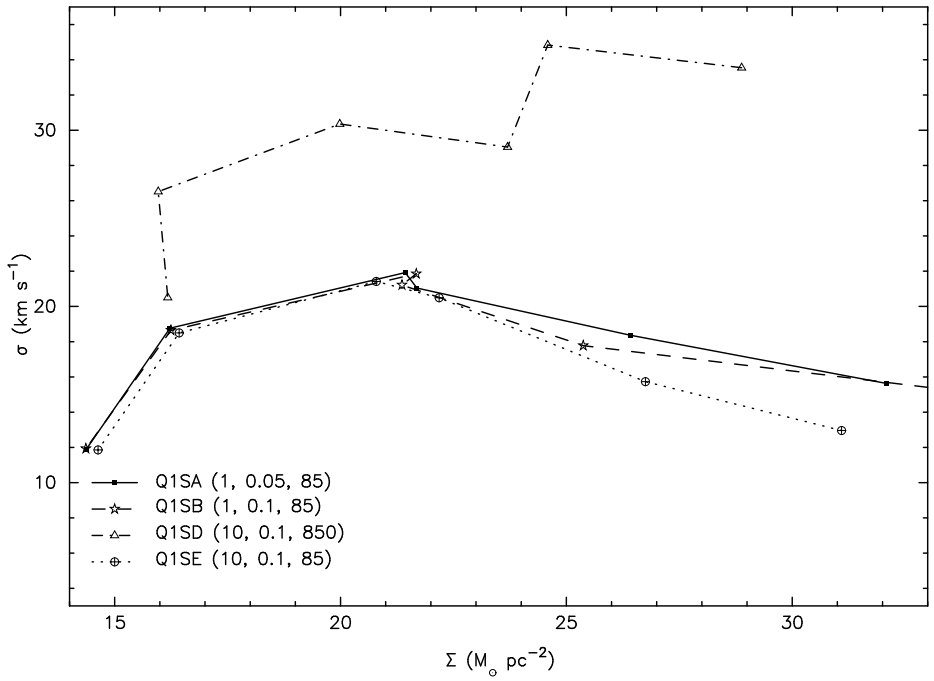

Figure 4.12: Velocity dispersion vs. mean surface density of Q1D models, averaged in annuli of widths 1 kpc, and in the time interval $t/t_{orb} \in 99.75 - 115.5$ Myr.

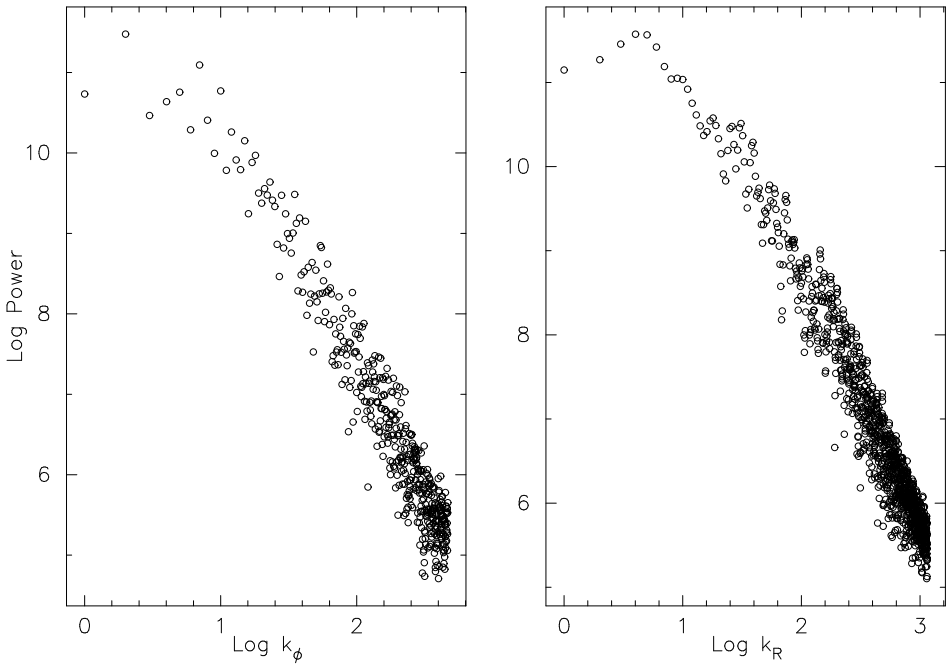

Figure 4.13: Turbulent power spectra of Model Q1D. Power is shown at constant k_R (left) and constant k_ϕ (right). Best fits for values between $\log(k) \in 1-2$ gives slopes of -3.1 (left) and -2.3 (right).

the data points are also shown. The rates show some scatter, both between models with different parameters, as well as between points from a given model. Overall, in most cases the general star formation rate - surface density relationship tends to increase consistent with a power law.

The $Q_0 = 1$ models, both with and without a spiral perturbation, and with different feedback parameters, all give slopes that agree to within a factor of about two. Most of the $Q_0 = 1$ models evolve for sufficiently long times that gas in the first clouds that are formed are allowed to be recycled into subsequently formed clouds. The $Q_0 = 2$ model, on the other hand, gives a variety of slopes, and the relationship between the star formation rate and surface density is not as well correlated as in the $Q_0 = 1$ models. The consistency of the slopes in the $Q_0 = 1$ models with varying parameters suggests that for marginally stable galaxies, turbulence does not qualitatively change the way star formation is regulated. For the $Q_0 = 2$ models, the number of feedback events are insufficient to affect much of the disk. As a result, some clouds continue to collapse, and the Courant condition is eventually violated. At this point the simulation must cease. The stochastic feedback events do not result in any developed turbulence. Therefore, the SFR as computed is sensitive to model parameters governing the feedback events, unlike the $Q_0 = 1$ spiral models.

We have also run simulations of the inner regions of disks, with radial extent $R \in 0.8 - 2.2$ kpc. The other parameters are the same as for the standard models. The only difference here, besides the radial range, is the initial surface density. Since Q_0 is constant, and $Q_0 \propto R^{-1}$, the initial surface density is 5 times larger. We have also measured the star formation rate for these models, to compare with the standard models.

Figure 4.15 shows the star formation rate as a function of surface density, for model Q1D, as well as the corresponding simulation of the inner region. The larger surface density does indeed lead to higher star formation rates, with a slope $\alpha = 2.2$ that is similar to the value $\alpha = 2.4$ of the standard model. We find similar trends for other inner disk

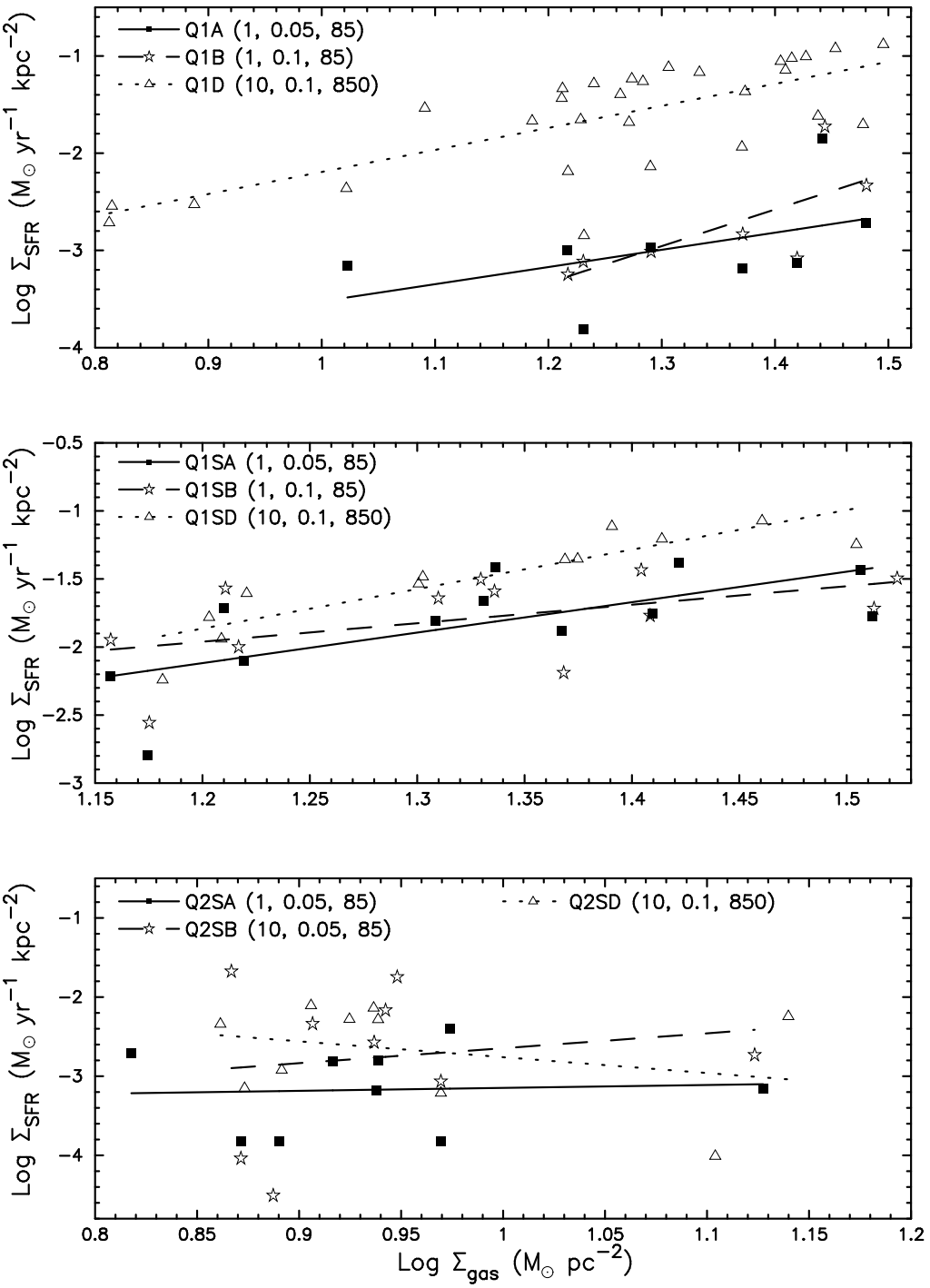

Figure 4.14: Schmidt law for models in Table 4.1. Each point is obtained by binning the simulation data in radii, with 1 kpc widths, and in time, with 19 Myr widths. Only annuli and times with at least 1 feedback event are included. The lines are the best fit to the points; with their slopes ranging from 1.8 - 3.8 (top), 1.4 - 3.0 (middle), and -2.0 - 1.9 (bottom).

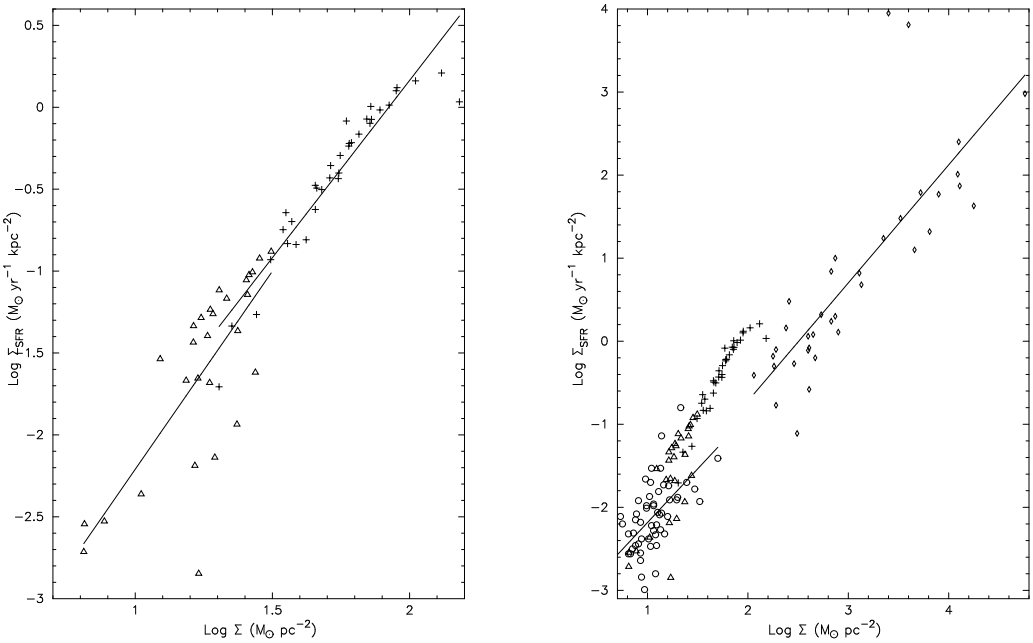

Figure 4.15: Left: Star formation rate vs. surface density for Models Q1D (triangles; $R \in$ 4 - 11 kpc), as well as the corresponding model of the inner region (crosses; $R \in$ 0.8 - 2.2 kpc). Best fit lines for each model is also shown, with slopes of 2.4 for the 4 - 11 kpc model and 2.2 for the 0.8 - 2.2 kpc model. Right: Triangles and crosses from figure on the left are shown, along with globally averaged observational data from Kennicutt (1998b): circles show normal spirals, with best fit slope of 1.3, and diamonds show IR sources, with best fit slope of 1.4.

models in comparison with the corresponding standard models. For comparison, Figure 4.15 also shows data from Kennicutt (1998b). Each point indicates the globally averaged star formation rate for individual galaxies. Though there is less scatter in the simulation points, the slope of the Σ_{SFR} - Σ relation from the simulations ($\sim$2.3) is larger than the slope from observational data ($\sim$1.4). At the low Σ end, the model results overlap with the observed points.

Predicting Gas Depletion Times

The gas depletion time t_{SF} is the time required for all gas to be converted to stars if the star formation proceeds as it has been during a given interval Δt:

$$t_{SF} = \Delta t \frac{M_{tot}}{\varepsilon_{SF} \sum M_{cl}}, \tag{4.18}$$

where M_{tot} is the total mass in a given annulus. The summation in equation (4.18) is taken over all clouds in which a feedback event has occurred, as in equation (4.15).

Observationally, if the supernovae rate per dense gas mass R_{SN} is known, the gas depletion time can be estimated based on the total amount of gas and the portion in dense clouds as:

$$t'_{SF} = \frac{M_{tot}}{\sum M_{den} M_{SN} R_{SN}}, \tag{4.19}$$

where $\sum M_{den}$ is the total mass of gas above some chosen threshold density. Since $R_{SN} M_{SN} = \varepsilon_{SF}/t_{cl}$ from equation (4.12), the results of equations (4.18) and (4.19) should agree on average. With R_{SN} = 1 or 10, $t'_{SF} = 2.5 \times 10^8 \times (M_{tot}/\sum M_{den})$ yr $\times$ 1 or 0.1.

Figure 4.16 shows the gas depletion time in different annuli for Model Q1D. The low values of t_{SF} are a result of the large input value of R_{SN} (which is not meant to be realistic). The actual depletion time, shown by the filled symbols, are computed using equation (4.18), after binning the simulation data in radii of 1 kpc widths and in time with t/t_{orb} = 0.125 widths. The open symbols show the predicted depletion time by applying equation (4.19) on the same binned data. The predicted times agrees well with the actual depletion times. We find similar agreement with all other models.[2] For this model, $t'_{SF} = 2.5 \times 10^7 \times (M_{tot}/\sum M_{den})$ yr. The increase of t'_{SF} with t_{orb} particularly at

[2]Most other models do not run for as long as the D models that have high feedback rates, because some dense clumps continue to collapse without feedback, eventually causing the Courant condition to be violated.

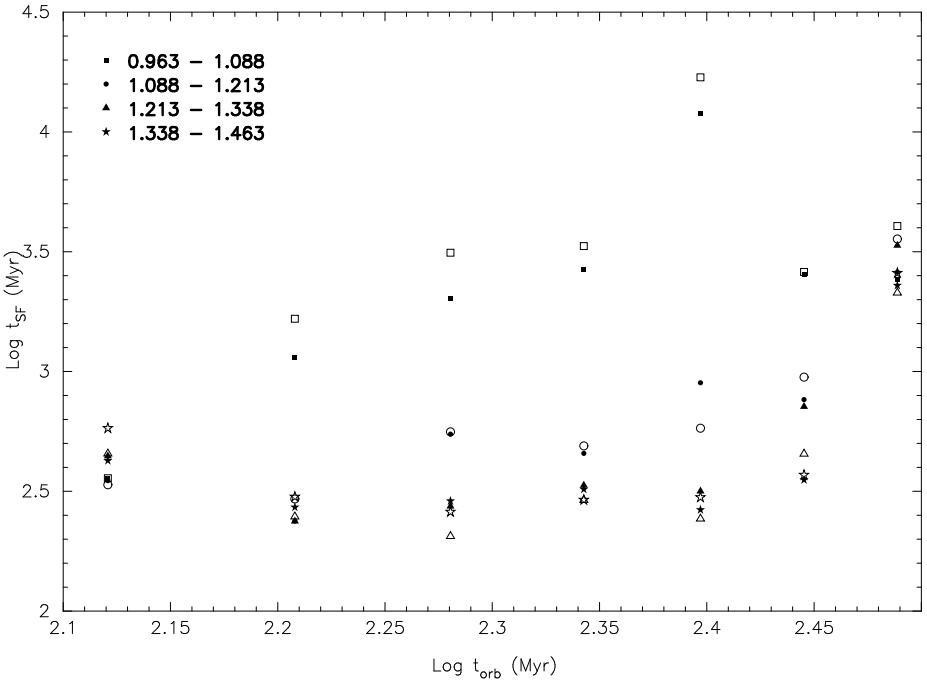

Figure 4.16: Gas depletion times from model Q1D, as a function of orbital time (or, equivalently, in different annuli). Legend shows, in t/t_{orb} the limits of each time bin. Filled symbols show actual depletion times (eqn. 4.18), and open symbols show predicted depletion times (eqn. 4.19).

early time, is indicative of an increase of $M_{tot}/\sum M_{den}$ with t_{orb} in annuli (i.e. a smaller fraction of the gas is dense at large radii, where Σ is lower.[3])

4.4 Discussion and Summary

4.4.1 Kennicutt-Schmidt Law in Simulations

We have found that the exponent of the $\Sigma_{SFR} \propto \Sigma^{\alpha}$ relation is somewhat sensitive to the supernovae parameters in $Q = 1$ models without spiral forcing, and in the spiral $Q = 2$ models. The exponent in the $Q = 1$ models with spiral forcing are relatively independent of the chosen supernovae parameters. In models that evolve for a significant amount

[3]The secular variation of Σ with t_{orb} at early times during the simulations (i.e. $\Sigma \propto R^{-1} \propto t_{orb}^{-1}$) contributes to the variation in the $t_{SF} - t_{orb}$ relation with time in Fig. 4.16; at later times, Σ is not proportional to R^{-1}.

of time, such as the models with high supernovae rates and shell velocities, there is a relatively tight correlation between Σ_{SFR} and Σ. In fact, the scatter in $\Sigma_{SFR} - \Sigma$ relation is smaller than from the observations of Kennicutt (1998b), as can be seen in Figure 4.15.

Simulations by Tasker & Bryan (2006) also show a power law $\Sigma_{SFR} - \Sigma$ relation. They find that the exponent is consistently 1.5, in agreement with observations, which they argue is a consequence of the dependence of clump formation on the dynamical time. However, they do not show the effect of varying the feedback parameters, which could affect the overall dynamics of the disk, and consequently the star formation properties.

Li et al. (2005a,b, 2006), by implementing sink particles into SPH simulations, study gravitational collapse in galaxy disks. Their simulations, spanning a range in surface densities, reproduced the slope and normalization of the Kennicutt - Schmidt law. They suggest that gravitational instability is the primary mechanism regulating star formation, due to independence of the slope of the $\Sigma_{SFR} - \Sigma$ relation from their input model parameters.

In the simulations of Li et al. (2005a,b, 2006), clouds can only form due to gravitational instability. As they indicate, cloud formation can only be modeled for one collapse time, since no feedback occurs. It may be at a stage early in the simulation, when clouds are forming, that the star formation rate is determined. In order to evolve the simulation for longer times, feedback is necessary. The rates at which gas is dispersed from clouds may affect the subsequent star formation rates, as we found in our models by varying R_{SN}.

A similar argument can be made for our $Q = 1$ spiral models. With spiral structure, the slope and normalization for all ($Q_0 = 1$) models are similar (middle panel of Figure 4.14). In these models, clouds initially form due to gravitational instability in the high density spiral arm gas. However, without an external spiral potential, the slopes and normalizations vary (top panel of Figure 4.14). In these models, clouds are forming along with the feedback induced destruction of other clouds all over the disk, so feedback has

an effect early on. Feedback even causes gas to collapse, in a region of colliding flow, for example. However, had we been able to evolve all our simulations for many more orbits, then it is possible that all models would give similar star formation properties. Our simulations suggest that measured star formation properties are subject to transient effects, thus for meaningful theoretical predictions it is necessary for systems to evolve well beyond the initial state.

Another possible reason for a $\Sigma_{SFR} \propto \Sigma^{1.5}$ relation in global simulations of disks is the effect of the disk thickness. The gas free-fall time is $\tau_g \sim (G\rho)^{-0.5}$. For thick disks, the volume density $\rho \sim \Sigma/H$. If the Kennicutt-Schmidt law is explained as $\Sigma_{SFR} \propto \Sigma_g/\tau_g$, then $\Sigma_{SFR} \propto \Sigma_g^{1.5}/\sqrt{H}$. In simulations that have a constant thickness (either by design or as a consequence of limited numerical resolution), then naturally $\Sigma_{SFR} \propto \Sigma_g^{1.5}$. However, for self-gravitating gaseous disks, the thickness would depend on the surface density, $H = c_s^2/(\pi G\Sigma)$ (if the vertical gravity is instead dominated by the stars, then $H = c_s/\sqrt{4\pi G\rho_*}$). In our models, we assume $H \propto R$ and also $\Sigma \propto R^{-1}$, so with $\Sigma_{SFR} \propto \Sigma_g/\tau_g$ would predict $\Sigma_{SFR} \propto \Sigma_g^2$. In models with the largest dynamical range in Σ and that evolve for a number of orbits, the slope is near this value, such as shown in Figure 4.15. However, the slopes may be dependent on other supernovae parameters; our other models show varying values (although they are statistically less well determined).

4.4.2 Model Limitations and Pending Questions

Spiral Structure

In spiral models, the external spiral potential is initially the primary driver for enhancing the density, leading eventually to the growth of clouds. In models that evolve for a significant amount of time, soon after feedback and the dispersal of cloud gas the global spiral pattern is disrupted, and eventually vanishes. With the simple feedback prescrip-

tion that we have adopted, we were unable to simulate a spiral galaxy in which the global spiral pattern is maintained simultaneously as cloud gas is returned to the ISM through feedback.

If the arms truly are long lasting, then either the spiral potential is much stronger than in our models ($F >> 10\%$), and/or that the feedback events are not as disruptive of structure on kpc scales. Very large F, however, does not appear consistent with observations of the old stellar disk (Rix & Rieke 1993). One possibility is that other feedback mechanisms such as stellar winds or photo-ionization in HII regions (e.g. Krumholz et al. 2006) act to disperse cloud gas, but do not completely destroy spiral arm coherence. Less correlated and spatially separated energy input would produce shells with dimensions less than the spiral arm thickness, and therefore may not destroy the global spiral structure.

We have shown that turbulence induced by correlated feedback events plays a significant role in the subsequent evolution of the gaseous disk. In our models, feedback occurs only after the formation of sufficiently dense clouds, which grow due to gravitational instability. The growth of clouds in an initially turbulent medium was not considered. This result raises the question of how spiral arms grow in a turbulent medium in the first place. In galaxy disks there are other sources of turbulence, and smaller scale turbulence may be less disruptive to the global spiral pattern.

Isothermality

In our models, we follow the isothermal expansion of the cloud, due to correlated supernovae events. Of course, just after a supernova event, energy is injected into the ISM. The high density shell cooling time ($\lesssim$ Myr) is much shorter than other timescales (such as the dynamical time, $\sim$ 100 Myr). The cooling time of the hot phase of the interstellar medium is longer, but contains a smaller fraction of the total mass of the ISM. We thus use the isothermal approximation for our simulations of the global flow focusing on the

warm component that contains most of the mass. We do not include the cold atomic component (T$\sim$100 K) explicitly. This component may be more gravitationally unstable than the warm component that we follow in our simulations, unless there is significant turbulence. Additionally, our models constrain feedback within the galaxy's midplane, and do not allow for dynamically evolving disk thickness. In the real ISM, energy injected from supernovae also affects the dynamics of the surrounding ISM, and contributes for maintaining the multi-phase structure of the ISM (McKee & Ostriker 1977). Such correlated supernovae may be important in driving the supernovae heated gas away from the midplane of the galaxy into the halo, through so-called chimneys and superbubbles (Norman & Ikeuchi 1989). After this gas is cooled in the halo, it falls back onto the disk in the form of cloudlets (e.g. Joung & Mac Low 2006). Even though recent simulations have shown that the fraction of mass that is vertically driven is small (de Avillez & Breitschwerdt 2004), the in-falling clouds may still affect the dynamics of the disk and may also act as another source of turbulence.

In order to accurately model disks that account for the effects of supernovae heating, chimneys, superbubbles, and the return of halo gas onto the disk, a 3D grid as well a numerical treatment of heating and cooling is necessary. 3D numerical simulations will also allow us to test the sensitivity of the Kennicutt-Schmidt slope to the disk thickness, as discussed in § 4.4.1. These processes are important avenues of future research that we plan on pursuing.

4.4.3 Summary

We have added feedback into our global simulations of gaseous disks (Chapter 3) in order to disperse gas that collapses due to self-gravity. We then analyzed the star formation and turbulent properties of disks with and without an externally imposed spiral perturbation. We summarize our main findings here:

1) In models with the largest dynamic range ($Q_0 = 1$ with spiral structure), the star formation rate density Σ_{SFR} is not strongly sensitive to the chosen feedback parameters. In other models, the simulations do not evolve for long after feedback, so a direct comparison is not applicable.

2) Feedback can cause colliding flows, within which density enhancements can collapse to eventually form stars. The characteristic masses of clouds formed in colliding flows are lower than those formed in spiral arms or the sheared background features. Higher resolution simulations will allow for a more detailed analysis of the mass distributions.

3) We find that the large scale turbulent velocity v_{turb} depends primarily on the input feedback momentum. Models with similar SFRs can have different measured values of v_{turb}. In models with low velocity dispersions, the SFR is proportional to the energy injection or supernovae rate. Large dispersions or efficient cloud destruction suppress subsequent star formation.

4) The SFRs in models with spiral structure are about 2-3 times larger than models without spiral structure (for $Q_0 = 1$).

5) For $1 < \log(\Sigma) < 2$, the range in Σ_{SFR} is similar to the range observed in normal disks. The slope of the Kennicutt-Schmidt $\Sigma_{SFR} \propto \Sigma^{\alpha}$ is steeper ($\alpha \sim 2$) in our simulations than the observed slope ($\alpha \approx 1.3 - 1.7$). For both low and high Σ, we find less scatter in $\Sigma_{SFR} - \Sigma$ than in observations. We suggest that the thickness of the gaseous disk may be important for setting the index in the Kennicutt-Schmidt relationship.

6) We were unable to model long lasting global spiral patterns; either the correlated feedback destroy global spiral structure as cloud gas is dispersed, or an insufficient amount of momentum is added to the gas clouds, so that arm clouds continue to collapse, eventually depleting the surround spiral arm gas. Perhaps other mechanisms, such as small scale turbulence and less correlated feedback, both spatially and temporally, are

required for global spiral patterns to persist.

Chapter 5

Summary and Future Work

5.1 Summary

The interdependence between large scale galaxy dynamics and much smaller scale star formation results in the ISM being rich in various physical processes. Grand-design stellar spiral structure causes perturbations in the differentially rotating gaseous disk. Gas is compressed in the spiral arms, and stars eventually form within these compressions. Gas that flows through and out the arm is also significantly perturbed, leading to the formation of spurs and feathers. Within gas clouds supernovae explosions from massive stars can return much of the remaining gas back into the surrounding ISM. The returned gas then continues its orbit around the galaxy's center, and may be involved in another episode of star formation. In this thesis, we present results of our investigation into spiral streaming in the gaseous component of the grand-design galaxy M51, of numerical simulations of the formation of spiral arm clouds and spurs, and star formation properties in disks with feedback.

Using interferometric CO and Fabry-Perot Hα observations, we studied the spiral streaming motions in M51. We fit the 2D observed velocity field to estimate the radial

and tangential velocity components at each arm phase. Using the velocity profile fits, we then analyzed whether the streaming motions are as predicted by a QSSS description. We found large radial streaming, resulting in a velocity field that is inconsistent with steady state continuity. Variations in the X-factor, position angle, or spiral pattern speed cannot account for the discrepancies. We thus concluded that the spiral arms in M51 are dynamic features, and perhaps that out-of-plane motions are significant.

In Chapter 3, we presented results of our first set of numerical simulations of gaseous disks. Gas self-gravity and galaxy rotation naturally cause large-scale sheared features to form. In simulations with an external spiral potential, representing the background stellar perturbation, gravitational instability causes gas to collapse in the arms, forming $\sim 10^7$ $M_\odot$ clouds. Additionally, spurs (or feathers) are formed out of the gas that flows through and out the arms, due to the combined effect of gravitational instability and shear. These spurs are different from the background sheared features because there is a one-to-one correlation between the spurs and the spiral arm clouds, and their orientation depends on the relative speeds between the spiral pattern and the gas: inside corotation, spurs project outward from the convex side of the arm, but outside corotation, spurs form on the concave side, projecting inward. Magnetic fields act to slow the collapse of the spiral arms, thereby suppressing pure hydrodynamic instabilities found by Wada & Koda (2004).

We extended our models to include feedback effects, which are presented in Chapter 4. In sufficiently dense clouds, we injected kinetic energy, modeling correlated supernovae explosions, to expand and disperse the cloud gas back into the surrounding ISM. We found that the relationship between the star formation rate density and the gas surface density can be expressed as a power law, consistent with observations (Kennicutt 1989). However, in models that evolve for a significant amount of time, the exponent is ~ 2. We suggest that if $\Sigma_{SFR} \propto \Sigma^{1.5}/\sqrt{H}$ (if it is governed by gas self-gravity), for disk thickness H, then $\Sigma_{SFR} \propto \Sigma^2$ would be expected in our simulations since $H \propto R$ (and $\Sigma \propto R^{-1}$).

This dependence may also explain results of previous simulations with constant H, which produce $\Sigma_{SFR} \propto \Sigma^{1.5}$. We also found that in simulations with high feedback rates, large feedback velocities can suppress subsequent star formation because clouds are efficiently destroyed. Simulations with and without an external spiral potential do not produce vastly different star formation rates.

5.2 Future Work

An outstanding issue relating to spiral structure is the offsets between various components. Observations of spiral galaxies show offsets between the molecular peaks, which is coincident with the dust lanes, and star forming regions traced by Hα (e.g. Tilanus et al. 1988; Vogel et al. 1988). However, due to the poor resolution of CO observations, these offsets require further investigation. Such offsets have been heavily discussed in the ongoing debate of star formation timescale; both in favor for and against rapid star formation (e.g Ballesteros-Paredes & Hartmann 2007; Tassis & Mouschovias 2004). The CARMA interferometer will produce the highest resolution CO map of M51 in the near future. We plan on investigating the CO peaks, relative to other high resolution images from *Spitzer* SINGS (Calzetti et al. 2005; Kennicutt et al. 2003) and the *Hubble Space Telescope* (Scoville et al. 2001). Infrared observations from *Spitzer* will be used to define the star formation peaks. We will average the intensities at each arm phase, as we described in Chapter 2, to measure the offsets between various components, and compare with the different predictions from star formation theories.

We also plan on extending our numerical simulations of disk galaxies. With 3D simulations, we can study the development of turbulence due to the spiral arms, as Kim et al. (2006) demonstrated with 2D ($R-z$) simulations. In addition, we could include a live stellar disk. Our current simulations only include a fixed external rotating potential;

with a live stellar disk, we can track the response of the stellar component to the gaseous disk; those simulations will expand on the 2D study of Kim & Ostriker (2007). Further, we could include heating and cooling to track the phase evolution of the gas. With a multi-phase medium as well as 3D, we can more realistically model feedback, taking into account the supernovae driving of hot gas away from the midplane (e.g Norman & Ikeuchi 1989), as well as the return of halo gas onto the disk in the form of cloudlets. Calculations including both a multi-phase medium and 3 dimensions will more accurately track turbulence, which has been a key topic in current studies of star formation.

5.3 Suggestions from Thesis Committee

The following are two interesting points that we discussed with the committee after the presentation.

1) Do observations show the kind of bifurcations we found in our simulations, due to ultra-harmonic resonances? If so, can corotation be identified using the locations of the bifurcations?

2) We found that magnetic fields strengthen the spiral arms, slowing the collapse and fragmentation of gas in the arms. Is there a systematic trend of stronger magnetic fields in grand-design galaxies?

Appendix A

Numerical Methods for Computing the Self-Gravitational Potential

A.1 Cartesian Coordinates

Numerically, Poisson's Equation

$$\nabla^2\Phi = 4\pi G\rho, \tag{A.1}$$

can be solved efficiently using Fourier methods. In 3D Cartesian coordinates,

$$\hat{\Phi}(k_x,k_y,k_z) = -\frac{4\pi G\hat{\rho}(k_x,k_y,k_z)}{k^2}, \tag{A.2}$$

where $\hat{\Phi}$ and $\hat{\rho}$ are the Fourier transform of the potential Φ and density ρ, and $k^2 = k_x^2+k_y^2+k_z^2$. If density is periodic on a domain (L_x,L_y,L_z) with (N_x,N_y,N_z) zones in each dimension, respectively, the values of $k_x = \pm n_x 2\pi/L_x$ with $n_x = 1\ldots N_x/2$.

For an infinitesimally thin, two dimensional disk, one may use separation of variables to show that the potential within the disk in Cartesian coordinates satisfies

$$\hat{\Phi}(k_x,k_y) = -\frac{2\pi G\hat{\Sigma}(k_x,k_y)}{|\mathbf{k}|}, \tag{A.3}$$

where $\hat{\Sigma}$ is the Fourier transform of the surface density Σ (e.g. Binney & Tremaine 1987). The effect of the nonzero disk thickness may be accounted for in an approximate way (Kim et al. 2002), such that equation (A.3) becomes

$$\hat{\Phi}(k_x, k_y) = -\frac{2\pi G\hat{\Sigma}}{|\mathbf{k}|(1+|\mathbf{k}|H)}, \tag{A.4}$$

where H is the thickness of the disk, and $\Sigma = 2H\rho$.

Obtaining the potential using Fourier methods expressed in equations (A.2) or (A.3) assumes that the density is periodic. Thus, the resulting potential includes a contribution from replicas of the density distribution (outside the computational domain). If in fact one desires to compute the potential of a spatially isolated system with zero density outside of the computational domain, then this method is modified by computing Fourier transforms on a larger, zero-padded array. The central portion of the larger array is filled with the density values from the original domain, and the surrounding zones are set to zero. To obtain a solution of the Poisson's equation, the zero-padded array must be at least twice the size of the original array in each dimension (e.g. Hockney & Eastwood 1981). A larger padded region moves unphysical cusps away from the boundaries of the computational domain; of course, increasing the size of the padded region requires more memory as well as CPU time.

A.2 Polar Coordinates I

In 2D cylindrical polar coordinates, a number of techniques have been explored to calculate the potential. Miller (1976) describes a method that sums the potential due to concentric rings in polar coordinates. The potential at (R,ϕ) is written as

$$\Phi(R,\phi) = -G\int_0^\infty R^{'}dR^{'}\int_0^{2\pi} d\phi^{'}D(R,R^{'};\phi-\phi^{'})\Sigma(R^{'},\phi^{'}) \tag{A.5}$$

where

$$D(R,R^{'};\phi-\phi^{'}) = (R^2+R^{'2}+\varepsilon^2-2RR^{'}\cos(\phi-\phi^{'}))^{-\frac{1}{2}}, \tag{A.6}$$

where, ε is a softening parameter. We can discretize equation (A.5), writing the result as

$$\Phi(R_i,\phi_l) = -G\sum_n\sum_j D(R_i,R_j;\phi_l-\phi_n)\Sigma(R_j,\phi_n)\delta A_{jn} \tag{A.7}$$

where $\delta A_{jn} = R_j\delta R_j\delta\phi_n$. The direct summation in equation (A.7) is computationally expensive; however, Fourier transforms can accelerate the computation. The integral over $\phi^{'}$ in equation (A.5) is a convolution of D with the mass distribution in the ring at $R_j^{'}$ with the equivalent for the sum in equation (A.7). By the Fourier convolution theorem, we can write

$$\hat{\Phi}_n(R_i) = -G\sum_{R_j}\hat{D}_n(R_i,R_j)\hat{M}_n(R_j), \tag{A.8}$$

where $\hat{M}_n(R_j)$ is the 1D Fourier transform in the azimuthal direction of the mass $M_{j,n} = \Sigma_{j,n}\delta A_{j,n}$. The discrete Fourier transform (in the $\hat{\phi}$ direction) of the Green's function $D(R,R^{'};\phi-\phi^{'})$, $\hat{D}_n(R_i,R_j)$, only needs to be computed once, at the beginning of the simulation. For an (R,ϕ) computational grid, including periodic replicas of the density is required to cover the full 2π domain of the azimuthal coordinate. The computational domain must therefore be $2\pi/m$ for some m; we use $m=2$ for a two-armed spiral. Aside from the effect of softening, this method of computing the potential is exact.

Even though the Miller (1976) method is more efficient than direct summation of equation (A.7), more memory and CPU time are still required than for a pure Fourier approach. Thus, for numerical expediency, we instead use a computationally more efficient method to obtain an approximate solution for Φ. Although this method is not an exact calculation of Φ, we show that the differences between the exact (Miller) method and our more efficient method is small. After describing our method, we show how the results, as well as CPU usage, from the different methods compare.

To compute an approximate potential Φ in polar coordinates based solely on Fourier transforms, we use the method described in §A.1. Below we refer to this method as the

coordinate transformation method. If we apply a coordinate transformation

$$\begin{aligned} x &\equiv R_0 \ln\left(\frac{R}{R_0}\right) \\ y &\equiv R_0\phi, \end{aligned} \tag{A.9}$$

Poisson's equation becomes

$$\frac{\partial^2\Phi}{\partial x^2} + \frac{\partial^2\Phi}{\partial y^2} + \left(\frac{R}{R_0}\right)^2 \frac{\partial^2\Phi}{\partial z^2} = \left(\frac{R}{R_0}\right)^2 4\pi G\rho. \tag{A.10}$$

For in-plane gradients large compared to vertical gradients, the solution is

$$\hat{\Phi}(k_x,k_y) = -\frac{2\pi G\hat{\tilde{\Sigma}}}{|k|^2 H}, \tag{A.11}$$

where $\tilde{\Sigma} = (R/R_0)^2\Sigma$. This has the same form as equation (A.4) in the limit $|k|H >> 1$.

More generally, solutions to the Laplace equation in cylindrical coordinates have the form $\sum_{k,l} A_{kl} C_l(kR) e^{il\phi} e^{-|kz|}$ where the C_l's are two independent Bessel functions - e.g. J_l and Y_l - and where $|z| \to \infty$ and azimuthal boundary conditions have been applied. The coefficients of each term in the sum is determined by the requirement that $\partial\Phi/\partial z|_{z=0^+} = 2\pi G\Sigma(R,\phi)$. Each A_{kl} can then be written as a Fourier-Hankel transform of the surface density $A_{kl} \propto \int_0^{2\pi} e^{-il\phi} d\phi \int_{-\infty}^{\infty} dR J_l(kR) R^2 \Sigma(R,\phi)$ (e.g. Binney & Tremaine 1987).

Since the force is dominated by terms with large gradients, the large k values are most important. For large arguments, the Bessel functions approach sinusoidal functions, so that the A_{kl}'s can be written as two-dimensional Fourier transforms of $\tilde{\Sigma}$. In this limit, we must have $\hat{\Phi}(k_x,k_y) = -2\pi G\hat{\tilde{\Sigma}}/|\mathbf{k}|$. Altogether, we may therefore write our approximate solution as

$$\hat{\Phi}(k_x,k_y) = -\frac{2\pi G\hat{\tilde{\Sigma}}}{|\mathbf{k}|(1+|\mathbf{k}|H)}, \tag{A.12}$$

where, $k_y = l/R$ and k_x is the wavenumber corresponding to the transformed radial coordinate. In order to have the x_i values equally spaced, the radial grid coordinates are equally separated in $\log R$.

With this method, the surface density is implicitly assumed periodic in both azimuth and radius. The spurious contribution from periodic replicas in the radial direction can be minimized by zero padding the edges of the density array in the radial direction, as described at the end of §A.1.

A.3 Comparison of Methods

To compare the effects of the periodic replicas in the test cases for the coordinate transformation method, we use arrays that are $2\times$, $4\times$, $8\times$, $16\times$, and $32\times$ the size of the original density array. The computational domain for the comparison tests has 256 radial elements and 1024 azimuthal elements. As an example, for the case for which we use a $4\times$ larger array, the size of the $\tilde{\Sigma}$ array before taking a Fourier transform to obtain $\hat{\tilde{\Sigma}}$ is 1024×1024. The actual values of the densities are stored in array elements in which the first (radial) index is between 385 and 640. All other elements of the array are set to zero.

To compare the two methods of computing the potential from test simulations, we arrange test cases for which the total mass in the computational domain is 0 or very small. The Fourier method will include contributions from matter outside the computational domain, due to the assumed periodicity of the density. Thus, minimizing the total mass reduces this superfluous contribution. In analyzing the differences between the methods, we keep in mind that the softening will affect the numerical values of the potential (and force) in regions with large density gradients. With the coordinate transformation method, we also compare the results from cases where the size of the zero padded zones vary.

We inspect the potential of three test disks containing (1) a positive and negative ring, (2) a positive and negative radial spoke, and (3) and a positive and negative logarithmic spiral arm. To avoid edge effects, we compare the region between the positive and negative mass distributions regions. For test cases (1) and (2), we find the relative difference

between the coordinate transformation and the Miller method ($|\Phi_{CT} - \Phi_{MM}|/\Phi_{MM}$) to be within $\sim$3%. For test case (3), we measure a relative difference of $\sim$5%. Again, these relative differences are measured between the positive and negative density regions, away from the edges of the disk. For the self-gravitating simulations we perform, we are interested in the growth of substructures under similar circumstances, i.e. away from the edges of the disk, near regions where the perturbed density is both positive and negative. Nevertheless, even near the edges, all tests give values of the potential that agree within $\sim$25%. Finally, the difference between the tests using the coordinate transformation (with varying sizes of the zero-padded zone) is negligible.

The main advantage of using the coordinate transformation method is the decrease in CPU time for each simulation. For this method computing the potential requires a multiplication of the density to obtain $\tilde{\Sigma}$, a Fourier transform to obtain $\hat{\tilde{\Sigma}}$, a multiplication in Fourier space for the gravitational kernel in equation (A.12), and an inverse Fourier transform to obtain Φ. This sequence requires fewer operations than the Miller computational method.

To measure the efficiency of each method, we use a test simulation slightly different from the ones described above. In these tests, with a grid of 256 radial and 512 azimuthal zones, a spiral potential is turned on over the first half orbit, then the self-gravitational potential is slowly turned on over another half an orbit. Thus, both potentials are turned on fully after one orbit. The test simulations are subsequently allowed to run for an additional orbit, after which the CPU times are compared.

All these tests, as well as many of the simulations presented in this paper, were run on a machine with a 2.99 GHz Pentium 4 processor, with 2 GB of RAM. Table A.1 shows the CPU time (relative to that using the exact solution) required for each test to run. It is evident, as expected, that the simulations using the coordinate transformation method (where we enlarge the density array by $2\times$, $4\times$, or $8\times$) requires much less CPU time

Table A.1. CPU Time for Different Potential Computation Methods

CT (2×) [a]	CT (4×) [a]	CT (8×) [a]	CT (16×) [a]	CT (32×) [a]	MM [b]
0.59	0.62	0.70	0.89	1.25	1.0

[a]CT: Coordinate Transformation, with zero-padded enlargement of density array as indicated in parentheses

[b]MM: Miller's Method

than those using the exact potential computational method. Since the numerical differences between the methods are modest, and to take advantage of the superior efficiency of the coordinate transformation method, we use the coordinate transformation method, enlarging the density array by $4\times$, for our high resolution simulations presented in this paper. We have also tested models using the Miller method, and obtain essentially the same results.

A.4 Polar Coordinates II

In §A.2, we described two methods to solve Poisson's equation numerically on a polar grid; both methods employ Fast Fourier Transforms (FFT). One method sums the potential from concentric rings, as described by Miller (1976). The other method employs a coordinate transformation from polar coordinates to a Cartesian-like coordinate system. The former method is exact, but computationally expensive, and the latter is an approximation, but computationally efficient.

Here, we describe another FFT based method that is exact, and more efficient than the Miller (1976) method. The basic scheme is described in Kalnajs (1971) and Binney & Tremaine (1987); we describe the method including the effect of the thickness H of the disk, which also acts as softening. The potential Φ at each position (R,ϕ) on the disk, at

z=0, is

$$\Phi(R,\phi,z=0) = -G\int dR^{'}\int d\phi^{'}\int dz^{'}\frac{R^{'}f(z^{'},R^{'})\Sigma(R^{'},\phi^{'})}{[R^{'2}+R^2-2RR^{'}\cos(\phi-\phi^{'})+z^{'2}]^{\frac{1}{2}}}. \quad \text{(A.13)}$$

Here, G is the usual gravitational constant and the coefficient function f, describing the vertical profile of the surface density Σ, must be normalized, $\int_{-\infty}^{\infty}dz^{'}f(z^{'},R^{'})=1$. Substituting $u=\ln R$, and $\zeta^{'}=z^{'}/\sqrt{2}R^{'}$ in equation (A.13), the potential reduces to

$$\Phi(R,\phi,z=0) = -Ge^{u}\int du^{'}\int d\phi^{'}\int d\zeta^{'}\frac{e^{u^{'}-u}e^{u^{'}}f(\zeta^{'},u^{'})\Sigma(u^{'},\phi^{'})}{[e^{u-u^{'}}(\cosh(u-u^{'})-\cos(\phi-\phi^{'}))+\zeta^{'2}]^{\frac{1}{2}}}. \quad \text{(A.14)}$$

If $e^{u^{'}}f(\zeta^{'},u^{'})$ is a function of $\zeta^{'}$ only, we can define

$$I(u^{'}-u,\phi^{'}-\phi) \equiv e^{u^{'}-u}\int d\zeta^{'}\frac{e^{u^{'}}f(\zeta^{'},u^{'})}{[e^{u-u^{'}}(\cosh(u-u^{'})-\cos(\phi-\phi^{'}))+\zeta^{'2}]^{\frac{1}{2}}}. \quad \text{(A.15)}$$

For a Gaussian vertical density distribution,

$$f(z^{'},R^{'}) = \frac{e^{-z^{'2}/2H^2(R^{'})}}{\sqrt{2\pi H^2(R^{'})}}. \quad \text{(A.16)}$$

For a radial thickness profile $H(R^{'})\propto R^{'}$, we define $\mathcal{H}=H(R^{'})/R^{'}$, so that[1]

$$e^{u^{'}}f(\zeta^{'},R^{'}) = \frac{e^{-(\zeta^{'}/\mathcal{H})^2}}{\sqrt{2\pi}\mathcal{H}}. \quad \text{(A.17)}$$

We now have an expression for I:

$$I(u^{'}-u,\phi^{'}-\phi) \equiv \frac{e^{u^{'}-u}}{\sqrt{2\pi}\mathcal{H}}\int_{-\infty}^{\infty}d\zeta^{'}\frac{e^{-(\zeta^{'}/\mathcal{H})^2}}{[e^{u-u^{'}}(\cosh(u-u^{'})-\cos(\phi-\phi^{'}))+\zeta^{'2}]^{\frac{1}{2}}}. \quad \text{(A.18)}$$

[1]If gas is the dominating component for vertical gravity, $H=c_s^2/\pi G\Sigma$, so that $H/R=c_sQ/\sqrt{2}v_c$. If both the Toomre Q parameter and c_s/v_c is independent of R, as in our models, then H/R = constant. Similarly, if the stellar disk dominates gravity then $H/R=c_sQ_*/2v_c$ so constant c_s/v_c and Q_* implies constant H/R. For self-gravitating gaseous disks, if $Q=1$ and v_c/c_s=30, then $H/R=0.02$. Including stellar gravity typically reduces H by a factor of ~ 2 (e.g Kim et al. 2002).

Substituting equation (A.15) into equation (A.14),

$$\Phi(R,\phi,z=0) = -Ge^{u}\int du^{'}\int d\phi^{'}\Sigma(u^{'},\phi^{'})I(u^{'}-u,\phi^{'}-\phi). \qquad \text{(A.19)}$$

The integral in equation (A.19) is simply a 2D convolution. Thus, through the convolution theorem, the gravitational potential can be computed by taking the Fourier transform of Σ to obtain $\hat{\Sigma}$, and then taking the inverse Fourier transform of the product of $\hat{\Sigma}$ and $\hat{I}$, where $\hat{I}$ is the Fourier transform of I. In hydrodynamic simulations, $\hat{I}$ can be computed once at the beginning of the simulation run, so that only two FFTs need to be performed at each time step, FFT(Σ) and FFT$^{-1}(\hat{\Sigma}\hat{I})$.

Bibliography

Aalto, S., Hüttemeister, S., Scoville, N. Z., & Thaddeus, P. 1999, ApJ, 522, 165

Allen, R. J., Knapen, J. H., Bohlin, R., & Stecher, T. P. 1997, ApJ, 487, 171

Artymowicz, P. & Lubow, S. H. 1992, ApJ, 389, 129

Balbus, S. A. 1988, ApJ, 324, 60

Balbus, S. A. & Hawley, J. F. 1991, ApJ, 376, 214

Ballesteros-Paredes, J. & Hartmann, L. 2007, Revista Mexicana de Astronomia y Astrofisica, 43, 123

Ballesteros-Paredes, J., Klessen, R. S., Mac Low, M.-M., & Vazquez-Semadeni, E. 2007, Protostars and Planets V, 63

Begeman, K. G. 1989, A&A, 223, 47

Bell, E. F. & de Jong, R. S. 2001, ApJ, 550, 212

Bertin, G. & Lin, C. C. 1996, Spiral structure in galaxies: A Density Wave Theory (Cambridge: MIT Press)

Bertin, G., Lin, C. C., Lowe, S. A., & Thurstans, R. P. 1989a, ApJ, 338, 78

—. 1989b, ApJ, 338, 104

Binney, J. & Tremaine, S. 1987, Galactic dynamics (Princeton: Princeton University Press)

Blitz, L., Fukui, Y., Kawamura, A., Leroy, A., Mizuno, N., & Rosolowsky, E. 2007, Protostars and Planets V, 81

Bouche, N., Cresci, G., Davies, R., Eisenhauer, F., Forster Schreiber, N. M., Genzel, R., Gillessen, S., Lehnert, M., Lutz, D., Nesvadba, N., Shapiro, K. L., Sternberg, A., Tacconi, L. J., Verma, A., Cimatti, A., Daddi, E., Renzini, A., Erb, D. K., Shapley, A., & Steidel, C. C. 2007, ArXiv e-prints, 706, arXiv:0706.2656

Calzetti, D., Kennicutt, Jr., R. C., Bianchi, L., Thilker, D. A., Dale, D. A., Engelbracht, C. W., Leitherer, C., Meyer, M. J., Sosey, M. L., Mutchler, M., Regan, M. W., Thornley, M. D., Armus, L., Bendo, G. J., Boissier, S., Boselli, A., Draine, B. T., Gordon, K. D., Helou, G., Hollenbach, D. J., Kewley, L., Madore, B. F., Martin, D. C., Murphy, E. J., Rieke, G. H., Rieke, M. J., Roussel, H., Sheth, K., Smith, J. D., Walter, F., White, B. A., Yi, S., Scoville, N. Z., Polletta, M., & Lindler, D. 2005, ApJ, 633, 871

Chakrabarti, S., Laughlin, G., & Shu, F. H. 2003, ApJ, 596, 220

Charlot, S. & Bruzual, A. G. 1991, ApJ, 367, 126

Chevalier, R. A. 1974, ApJ, 188, 501

Cioffi, D. F., McKee, C. F., & Bertschinger, E. 1988, ApJ, 334, 252

Cohen, R. S., Dame, T. M., & Thaddeus, P. 1986, ApJS, 60, 695

Cox, D. G. 2005, ARA&A, 43, 337

de Avillez, M. A. & Breitschwerdt, D. 2004, A&A, 425, 899

de Vaucouleurs, G., de Vaucouleurs, A., Corwin, Jr., H. G., Buta, R. J., Paturel, G., & Fouque, P. 1991, Third Reference Catalogue of Bright Galaxies (Volume 1-3, XII, 2069 pp. 7 figs.. Springer-Verlag Berlin Heidelberg New York)

Dobbs, C. L. & Bonnell, I. A. 2006, MNRAS, 367, 873

Elmegreen, B. G. 1994, ApJ, 433, 39

—. 2002, ApJ, 577, 206

Elmegreen, B. G. & Elmegreen, D. M. 1983, MNRAS, 203, 31

Elmegreen, B. G. & Scalo, J. 2004, ARA&A, 42, 211

Elmegreen, B. G., Seiden, P. E., & Elmegreen, D. M. 1989, ApJ, 343, 602

Elmegreen, D. M. 1980, ApJ, 242, 528

Elmegreen, D. M. & Elmegreen, B. G. 1982, MNRAS, 201, 1021

Feldmeier, J. J., Ciardullo, R., & Jacoby, G. H. 1997, ApJ, 479, 231

Ferguson, A. M. N., Wyse, R. F. G., Gallagher, J. S., & Hunter, D. A. 1998, ApJ, 506, L19

Field, G. B., Goldsmith, D. W., & Habing, H. J. 1969, ApJ, 155, L149+

Frigo, M. & Johnson, S. G. 2005, Proc. IEEE, 93, 216

Gittins, D. M. & Clarke, C. J. 2004, MNRAS, 349, 909

Goldreich, P. & Lynden-Bell, D. 1965, MNRAS, 130, 125

Gómez, G. C. & Cox, D. P. 2002, ApJ, 580, 235

Gruendl, R. A. 1996, Ph.D. Thesis

Hagiwara, Y., Henkel, C., Menten, K. M., & Nakai, N. 2001, ApJ, 560, L37

Heiles, C. & Troland, T. H. 2003, ApJ, 586, 1067

Helfer, T. T., Thornley, M. D., Regan, M. W., Wong, T., Sheth, K., Vogel, S. N., Blitz, L., & Bock, D. C.-J. 2003, ApJS, 145, 259

Henry, A. L., Quillen, A. C., & Gutermuth, R. 2003, AJ, 126, 2831

Heyer, M. H., Corbelli, E., Schneider, S. E., & Young, J. S. 2004, ApJ, 602, 723

Ho, P. T. P., Martin, R. N., Henkel, C., & Turner, J. L. 1987, ApJ, 320, 663

Hockney, R. W. & Eastwood, J. W. 1981, Computer Simulation Using Particles (Computer Simulation Using Particles, New York: McGraw-Hill, 1981)

Hubble, E. P. 1936, Yale University Press

Jensen, J. B., Tonry, J. L., & Luppino, G. A. 1996, in Bulletin of the American Astronomical Society, 1419–+

Joung, M. K. R. & Mac Low, M.-M. 2006, ApJ, 653, 1266

Kalnajs, A. J. 1971, ApJ, 166, 275

Kennicutt, R. C. 1989, ApJ, 344, 685

Kennicutt, Jr., R. C. 1981, AJ, 86, 1847

—. 1998a, ARA&A, 36, 189

—. 1998b, ApJ, 498, 541

Kennicutt, Jr., R. C., Armus, L., Bendo, G., Calzetti, D., Dale, D. A., Draine, B. T., Engelbracht, C. W., Gordon, K. D., Grauer, A. D., Helou, G., Hollenbach, D. J., Jarrett, T. H., Kewley, L. J., Leitherer, C., Li, A., Malhotra, S., Regan, M. W., Rieke, G. H., Rieke, M. J., Roussel, H., Smith, J.-D. T., Thornley, M. D., & Walter, F. 2003, PASP, 115, 928

Kennicutt, Jr., R. C., Calzetti, D., Walter, F., Helou, G., Hollenbach, D. J., Armus, L., Bendo, G., Dale, D. A., Draine, B. T., Engelbracht, C. W., Gordon, K. D., Prescott, M. K. M., Regan, M. W., Thornley, M. D., Bot, C., Brinks, E., de Blok, E., de Mello, D., Meyer, M., Moustakas, J., Murphy, E. J., Sheth, K., & Smith, J. D. T. 2007, ArXiv e-prints, 708, arXiv:0708.0922

Kim, C.-G., Kim, W.-T., & Ostriker, E. C. 2006, ApJ, 649, L13

Kim, W.-T. 2002, PhD thesis, AA(UNIVERSITY OF MARYLAND COLLEGE PARK)

Kim, W.-T. & Ostriker, E. C. 2001, ApJ, 559, 70

—. 2002, ApJ, 570, 132

—. 2006, ApJ, 646, 213

—. 2007, ApJ, 660, 1232

Kim, W.-T., Ostriker, E. C., & Stone, J. M. 2002, ApJ, 581, 1080

—. 2003, ApJ, 599, 1157

Knapen, J. H. & Beckman, J. E. 1996, MNRAS, 283, 251

Krumholz, M. R., Matzner, C. D., & McKee, C. F. 2006, ApJ, 653, 361

Kuno, N. & Nakai, N. 1997, PASJ, 49, 279

La Vigne, M. A., Vogel, S. N., & Ostriker, E. C. 2006, ApJ, 650, 818

Li, Y., Mac Low, M.-M., & Klessen, R. S. 2005a, ApJ, 620, L19

—. 2005b, ApJ, 626, 823

—. 2006, ApJ, 639, 879

Lin, C. C. & Shu, F. H. 1964, ApJ, 140, 646

Lindblad, B. 1963, Stockholms Observatoriums Annaler, 5

Lowe, S. A., Roberts, W. W., Yang, J., Bertin, G., & Lin, C. C. 1994, ApJ, 427, 184

Lubow, S. H., Cowie, L. L., & Balbus, S. A. 1986, ApJ, 309, 496

Lynds, B. T. in , IAU Symposium, Vol. 38, The Spiral Structure of our Galaxy, ed. W. BeckerG. I. Kontopoulos, 26–+

Mac Low, M.-M. & Klessen, R. S. 2004, Reviews of Modern Physics, 76, 125

Martin, C. L. & Kennicutt, Jr., R. C. 2001, ApJ, 555, 301

McGaugh, S. S. 2005, ApJ, 632, 859

McGaugh, S. S., Schombert, J. M., Bothun, G. D., & de Blok, W. J. G. 2000, ApJ, 533, L99

McKee, C. F. & Ostriker, E. C. 2007, ARA&A, 45, 565

McKee, C. F. & Ostriker, J. P. 1977, ApJ, 218, 148

McKee, C. F. & Williams, J. P. 1997, ApJ, 476, 144

Merrifield, M. R., Rand, R. J., & Meidt, S. E. 2006, MNRAS, 366, L17

Miller, R. H. 1976, Journal of Computational Physics, 21, 400

Mohan, R., Dwarakanath, K. S., & Srinivasan, G. 2004, Journal of Astrophysics and Astronomy, 25, 185

Nakai, N. & Kasuga, T. 1988, PASJ, 40, 139

Nakai, N. & Kuno, N. 1995, PASJ, 47, 761

Norman, C. A. & Ikeuchi, S. 1989, ApJ, 345, 372

Piontek, R. A. 2005, PhD thesis, University of Maryland, College Park

Quirk, W. J. 1972, ApJ, 176, L9+

Rand, R. J. 1993, ApJ, 410, 68

—. 1995, AJ, 109, 2444

Regan, M. W., Thornley, M. D., Helfer, T. T., Sheth, K., Wong, T., Vogel, S. N., Blitz, L., & Bock, D. C.-J. 2001, ApJ, 561, 218

Rix, H.-W. & Rieke, M. J. 1993, ApJ, 418, 123

Roberts, W. W. 1969, ApJ, 158, 123

Roberts, W. W. & Stewart, G. R. 1987, ApJ, 314, 10

Rots, A. H., Bosma, A., van der Hulst, J. M., Athanassoula, E., & Crane, P. C. 1990, AJ, 100, 387

Salo, H. & Laurikainen, E. 2000, MNRAS, 319, 377

Schaye, J. 2004, ApJ, 609, 667

Schmidt, M. 1959, ApJ, 129, 243

Schuster, K. F., Kramer, C., Hitschfeld, M., Garcia-Burillo, S., & Mookerjea, B. 2007, A&A, 461, 143

Scoville, N. Z., Polletta, M., Ewald, S., Stolovy, S. R., Thompson, R., & Rieke, M. 2001, AJ, 122, 3017

Scoville, N. Z. & Rector, T. 2001, HST Press Release

Shetty, R. & Ostriker, E. C. 2006, ApJ, 647, 997

Shetty, R., Vogel, S. N., Ostriker, E. C., & Teuben, P. J. 2007, ApJ, 665, 1138

Shu, F. H., Milione, V., & Roberts, Jr., W. W. 1973, ApJ, 183, 819

Spitzer, L. 1978, Physical processes in the interstellar medium (New York Wiley-Interscience)

Stone, J. M. & Norman, M. L. 1992a, ApJS, 80, 753

—. 1992b, ApJS, 80, 791

Strong, A. W., Bloemen, J. B. G. M., Dame, T. M., Grenier, I. A., Hermsen, W., Lebrun, F., Nyman, L.-A., Pollock, A. M. T., & Thaddeus, P. 1988, A&A, 207, 1

Tasker, E. J. & Bryan, G. L. 2006, ApJ, 641, 878

Tassis, K. & Mouschovias, T. C. 2004, ApJ, 616, 283

Teuben, P. ASP Conf. Ser. 77: Astronomical Data Analysis Software and Systems IV, ed. , R. A. ShawH. E. Payne & J. J. E. Hayes, 398–+

Tilanus, R. P. J. & Allen, R. J. 1989, ApJ, 339, L57

Tilanus, R. P. J., Allen, R. J., van der Hulst, J. M., Crane, P. C., & Kennicutt, R. C. 1988, ApJ, 330, 667

Toomre, A. 1964, ApJ, 139, 1217

Toomre, A. in , Structure and Evolution of Normal Galaxies, ed. S. M. FallD. Lynden-Bell, 111–136

Toomre, A. & Toomre, J. 1972, ApJ, 178, 623

Truelove, J. K., Klein, R. I., McKee, C. F., Holliman, II, J. H., Howell, L. H., & Greenough, J. A. 1997, ApJ, 489, L179+

Tully, R. B. 1974, ApJS, 27, 449

Tully, R. B. & Fisher, J. R. 1977, A&A, 54, 661

van der Kruit, P. C. & Shostak, G. S. 1982, A&A, 105, 351

Verheijen, M. A. W. 2001, ApJ, 563, 694

Visser, H. C. D. 1980a, A&A, 88, 159

—. 1980b, A&A, 88, 149

Vogel, S. N., Kulkarni, S. R., & Scoville, N. Z. 1988, Nature, 334, 402

Vogel, S. N., Rand, R. J., Gruendl, R. A., & Teuben, P. J. 1993, PASP, 105, 666

Wada, K. & Koda, J. 2004, MNRAS, 349, 270

Wada, K., Meurer, G., & Norman, C. A. 2002, ApJ, 577, 197

Wada, K. & Norman, C. A. 2001, ApJ, 547, 172

—. 2007, ApJ, 660, 276

Williams, J. P., de Geus, E. J., & Blitz, L. 1994, ApJ, 428, 693

Williams, J. P. & McKee, C. F. 1997, ApJ, 476, 166

Wong, T. & Blitz, L. 2002, ApJ, 569, 157

Woodward, P. R. 1975, ApJ, 195, 61

Wyse, R. F. G. 1986, ApJ, 311, L41

Wyse, R. F. G. & Silk, J. 1989, ApJ, 339, 700

Zimmer, P., Rand, R. J., & McGraw, J. T. 2004, ApJ, 607, 285